Available online at www.sciencedirect.com

ScienceDirect

Icarus 192 (2007) 248–286

ICARUS

www.elsevier.com/locate/icarus

The origin of non-porphyritic pyroxene chondrules in UOCs: Liquid solar nebula condensates?

Almut Engler [a], Maria Eugenia Varela [b,*], Gero Kurat [c], Denton Ebel [d], Paul Sylvester [e]

[a] Department of Mineralogy and Petrology, University of Graz, Universitätsplatz 2, A8010, Graz, Austria
[b] Complejo Astronómico El Leoncito (CASLEO), Av. España 1512 sur, J5402DSP, San Juan, Argentina
[c] Institut für Geologische Wissenschaften, Universität Wien, Althanstrasse 14, 1090 Vienna, Austria
[d] Department of Earth and Planetary Sciences, American Museum of Natural History, New York, NY 10024-5192, USA
[e] Department of Earth Sciences, Memorial University of Newfoundland, St. John's, NF A1B 3X5, Canada

Received 9 September 2006; revised 14 June 2007

Abstract

A total of 56 non-porphyritic pyroxene and pyroxene/olivine micro-objects from different unequilibrated ordinary chondrites were selected for detailed studies to test the existing formation models. Our studies imply that the non-porphyritic objects represent quickly quenched liquids with each object reflecting a very complex and unique evolutionary history. Bulk major element analyses, obtained with EMPA and ASEM, as well as bulk lithophile trace element analyses, determined by LA-ICP-MS, resulted in unfractionated (solar-like) ratios of CaO/Al_2O_3, Yb/Ce as well as Sc/Yb in many of the studied objects and mostly unfractionated refractory lithophile trace element (RLTE) abundance patterns. These features support an origin by direct condensation from a gas of solar nebula composition. Full equilibrium condensation calculations show that it is theoretically possible that pyroxene-dominated non-porphyritic chondrules with flat REE patterns could have been formed as droplet liquid condensates directly from a nebular gas strongly depleted in olivine. Thus, it is possible to have enstatite as the stable liquidus phase in a $800 \times$ CI dust-enriched nebular gas at a p^{tot} of 10^{-3} atm, if about 72% of the original Mg is removed (as forsterite?) from the system. Condensation of liquids from vapor (primary liquid condensation) could be considered as a possible formation process of the pyroxene-dominated non-porphyritic objects. This process can produce a large spectrum of chemical compositions, which always have unfractionated RLTE abundances. Late stage and subsolidus metasomatic events appear to have furthered the compositional diversity of chondrules and related objects by addition of moderately volatile and volatile elements to these objects by exchange reactions with the chondritic reservoir (e.g., V, Cr, Mn, FeO as well as K and Na). The strong fractionation displayed by the volatile lithophile elements could be indicative of a variable efficiency of metasomatic processes occurring during and/or after chondrule formation. Histories of individual objects differ in detail from each other and clearly indicate individual formation and subsequent processing.

Keywords: Cosmochemistry; Solar nebula; Meteorites

---

1. Introduction

Chondrites are the most primitive meteorites which preserve useful information about the time the Solar System formed, about 4.56 Ga ago. One of their major constituents are chondrules, µm to mm-sized spherical objects, which are composed mainly of ferromagnesian silicates with glassy or cryptocrystalline mesostasis and accessory sulfides and FeNi metal.

In the early 20th century, Merrill published a summary of the theories of chondrule origin (Merrill, 1929a) that had been advanced by earlier scientists like Reichenbach, Sorby and Tschermak, together with his own views (Merrill, 1929b). Since that time, chondrules and chondrule formation are studied intensely. However, there is no real consensus regarding the origin of chondrules and many issues concerning their formation still remain unresolved (e.g., Wood, 1996).

Models for chondrule origins can be separated into two major groups: chondrules may have formed in the early solar nebula (e.g., primary origin; Grossman, 1988), or they may have

---

[*] Corresponding author.
E-mail address: evarela@casleo.gov.ar (M.E. Varela).

0019-1035/$ – see front matter © 2007 Elsevier Inc. All rights reserved.
doi:10.1016/j.icarus.2007.06.016

formed on asteroidal or planetary bodies during or shortly after accretion (e.g., secondary origin). Our attention is focused on solar nebula models. The two main models propose that chondrules were formed either: (1) by melting of pre-existing solids during transient, localized heating events or, (2) by direct condensation in the solar nebula.

In the early 1960s, Wood (1962, 1963) advanced the hypothesis that chondrules could have formed through condensation in the solar nebula and was later supported by, among others, Blander and Katz (1967), Blander and Abdel-Gawad (1969), Wood and McSween (1977) and Blander (1983). Some years later, e.g., Cameron (1966), Whipple (1966), Larimer (1967), Larimer and Anders (1967) and Gooding et al. (1980) suggested that chondrules could have formed by melting of pre-existing aggregates of dust in the solar nebula, a theory which is favored by most of the scientists working on chondrules today. Nevertheless, there is still no consensus on the nature of the heat sources necessary for such a melting process, nor how dust aggregates into chondrule precursors of sufficient size and chemical diversity. Several heating mechanisms have been suggested, such as lightning (electrical discharge heating) in a turbulent or stratified nebula (e.g., Cameron, 1966; Whipple, 1966; Rasmussen and Wasson, 1982; Wasson, 1992; Phillip et al., 1998; Desch and Cuzzi, 2000) or frictional heating of dust clumps falling into the nebula mid-plane (Wood, 1983, 1984) as well as nebular flares (e.g., Sonett, 1979; Levy and Araki, 1989). More recently, FU Orionis outbursts or gamma-ray bursts, bipolar out-flows and especially nebular shock waves (e.g., Liffman and Brown, 1996; Weidenschilling et al., 1998; McBreen and Hanlon, 1999; Desch and Connolly, 2002; Ciesla and Hood, 2002, 2003) are the most popular heating mechanism for chondrule formation (for more details also see Boss, 1996). In the X-wind model of Shu et al. (1996, 2001) chondrules are melted near the proto-sun by radiation related to flares. Additional models suggest that chondrules were formed in interstellar space (e.g., Skinner, 1990; Cameron, 1995).

On the other hand, models for chondrule formation by direct condensation in the solar nebula are rejected by many scientists today (e.g., Grossman and Wasson, 1983). The major problems with the condensation origin of chondrules are: the presence of "relict grains" (actually, grains with chemical and isotopic properties that differ from those of the common ones—a model-dependent interpretation turns them into "relics" which have either survived melting or evaporation in a high temperature environment), the chemical and isotopic variety of chondrules (condensation should produce chemically and isotopically homogeneous matter; e.g., Gooding et al., 1983; Sears et al., 1992), the high cooling rates interpreted for chondrules, based on analog experiments (e.g., Hewins, 1988; Lofgren, 1989), the fact that mean chondrules are not significantly depleted in volatiles compared to whole rocks (Grossman and Wasson, 1983) as well as the fact that producing liquid condensates in the physical setting of the solar nebula (Wood and Morfill, 1988) is considered to be difficult. Liquids are stable equilibrium phases in a gas under special pressure and composition conditions only. They are not stable in a gas of solar composition at the low-pressures that characterize solar nebula models like that of Cameron (1962), Grossman (1972) or Arrhenius and De (1973). For liquids to become stable in a solar gas, this gas must be enriched in condensable elements (e.g., one way to achieve this scenario is by dust-enrichment, model dependent but principally fractionated Si/H ratio) to a sufficiently high degree (e.g., Wood and Hashimoto, 1993). Recent works of Yoneda and Grossman (1995), Ebel and Grossman (2000), Alexander (2004) and Ebel (2005) clearly show that in regions of high dust enrichment, or high total gas pressure, olivine-rich silicate liquids can exist as stable equilibrium phases. The same was theoretically shown by Ebel et al. (2003) also for pyroxene-rich liquid compositions, which become stable in Mg-depleted systems, although in a highly restricted pressure–temperature-composition field. Thus, liquid condensation of a variety of chemical compositions is theoretically possible and should, therefore, be considered as a possible chondrule formation process.

Recently, we have discussed how the primary liquid condensation (PLC) model can help—with a thin liquid interface between vapor and crystal—to grow crystals directly from the vapor (Varela et al., 2005) and how this model can also be applied to the formation of porphyritic chondrules and aggregates (Kurat et al., 2004) as well as to the formation of barred olivine chondrules (Varela et al., 2006). Here, we will investigate how this model can also serve to explain the formation of non-porphyritic pyroxene-rich chondrules.

Preliminary results on trace element patterns for some Tieschitz, Mezö-Madaras, Krymka and Bishunpur objects are published in Engler et al. (2003) and Engler (2004).

2. Samples and analytical methods

A total of 56 micro-objects from 5 different unequilibrated ordinary chondrites were selected for detailed studies. Eight objects each were selected from Bishunpur (LL3.1; polished section—PS—"from G3684") and Krymka (LL3.1; PS "from L3510"), fourteen objects each from Sahara 97210 (L/LL3.6; PS no name) and Mezö-Madaras (L3.7; PS—no name), and twelve objects from Tieschitz (H3.6; PS "from C784"). All samples belong to the Natural History Museum (NHM) in Vienna. Abbreviations of sample names used throughout the report are as follows: BP = Bishunpur, KR = Krymka, MM = Mezö-Madaras, SO = Sahara 97210 and TS = Tieschitz. Objects that were selected by optical microscopy, all have cryptocrystalline, radially crystallized, or barred olivine textures.

2.1. Analytical techniques

For object characterization and major and minor element analyses we used the JEOL JSM 6400 analytical scanning electron microscope (SEM), equipped with a Norton energy-dispersive system utilizing a Kevex Quantum X-ray analyzer with a Si(Li) crystal cooled by a Peltier system operating at 15 kV and 1–2 nA beam current at the NHM in Vienna.

Estimated analytical precision for major elements is better than 5% relative and better than 20% relative for minor elements (for values below 2 wt% analytical precision declines strongly). Analyses were done standardless. Bulk chondrule/object compositions were obtained by rastering areas including major parts of the objects or sometimes even the whole object. This method yields accurate bulk analyses for fine-grained and cryptocrystalline objects.

When possible, objects were also analyzed with an electron microprobe (EMP) for their major and minor element bulk chemical composition. In addition, the compositions of individual phases within each object—where possible—were also determined. We used the CAMECA SX100 of the Department of Geological Sciences at the University of Vienna with an accelerating voltage of 15 kV and a beam current of 20 nA. Estimated precision for major and minor elements is better than 3%, for Na about 10%. Natural and synthetic standards were used for calibration and a PAP correction was applied to the data.

For geometric reasons only a small scan region can be analyzed by EMPA. Scan widths of approximately 7.5 µm × 10 µm were set closely to each other, without overlapping. Several analyses covering areas with a maximum of 80 × 80 µm were averaged to give an estimated bulk composition. But in several objects (if major phases are coarse-grained and/or inhomogeneously distributed) an area of 80 × 80 µm was still not representative. Especially Fe and S were probably not measured representatively, because metal and sulfide usually are not distributed homogeneously inside the objects. Another problem is posed by voids (some objects, e.g., in Tieschitz, contain many voids in between the crystals). In some cases, instead of rastering, line-scans were used. Analyses were averaged to compute a bulk composition. Bulk analysis by EMPA were appropriate for cryptocrystalline, fine-grained and homogenous objects only, due to these sampling problems. Additionally, major and minor element contents of silicate phases were measured by EMPA.

The bulk trace element contents, as well as trace element contents of individual silicate phases within each object, were measured with a VG Plasma Quad II+ "S" ICPMS and a 266 nm Q-switched Nd-YAG laser at the Memorial University of Newfoundland (see Jackson et al., 1992; Jenner et al., 1993; Jackson, 2001). The laser was pulsed at a frequency of 10 Hz, with an energy of 0.3–0.4 mJ per pulse. The first 40 s of each measurement were acquired with the laser off to determine the background count rates for each analysis. The sample was then ablated for a maximum of 80 s, depending on the stability of the acquired signals and the thickness of the sample. Where the laser was likely to burn through the sample material very quickly (in glass, olivine or generally in thin sections), the laser beam was defocused to 200 µm above the sample surface, using an optical microscope. We used sampling pit diameters in the range of 10–40 µm (usually 40 µm, depending on the area of interest and/or the object size). NIST 612 glass, a synthetic silicate glass spiked with 61 elements at a nominal concentration of about 50 ppm, was used as the standard for calibration. We used the calibration values of Pearce et al. (1997) in NIST 612 to standardize for all measured elements. Reference materials USGS BCR2G as well as in some runs a radiating pyroxene chondrule ALLENDE SHE, which was previously analyzed by instrumental neutron activation analysis (INAA; see Kurat, 1985), were run as secondary checks on data quality. The standard NIST glass was measured twice at the start of each analytical run and was re-measured twice after a maximum of 16 analyses of unknowns (including the reference materials) to correct for instrumental drift. To correct for temporal and matrix-dependent variations in ablation yield during each run of analyses, Si was used as an internal standard, based on SEM analyses of that element in each object. Either 100 × 100 µm raster, line scans, or single point analyses (mean values) were used to gain bulk analyses of the objects, depending on the grain size and homogeneity of chondrules and fragments. The accuracy and precision for the instrumentation used in this study has been reported by Horn et al. (1997) and Taylor et al. (1997).

All measurements were performed in time resolved analysis mode utilizing peak jumping mode with 1 point per mass peak. Dwell time was 8.3 ms, with a quadrupole settling time of 1 ms per mass. Raw counts were processed off line to integrate signals from each sequential set of 3 sweeps. Data reduction and concentration calculations were then performed using the in-house developed spreadsheet-based program LAMTRACE.

For long term precision of each element we calculated the RSD on the average of all the replicate analyses of the BCR standard, which was run at least twice in all of the individual sets of 20 analyses (one analytical run). Long term precision is better than 10% for most of the analyzed elements, except of Gd, Dy, Ho, Er, Tm, Yb, Lu, Hf, W, Th and Ti, for which it ranges between 10–15% and Cr for which it is 22%. The exact source of the lower precision for the Cr data is not known but may be due to variable ^{40}Ar^{12}C signals in gas backgrounds and resulting instability in ^{52}Cr signals.

An estimate of the accuracy of the analytical method used in this study has been made by comparison of laser ICPMS analyses for BCR-2G made in our laboratory with those made for BCR-2G in other laser ICPMS laboratories (Norman et al., 1998; Barth et al., 2001) and those made for BCR-2G by solution-based ICPMS analysis in our laboratory (unpublished data). For all elements of interest, the correspondence between our laser ICPMS results and the other results is within 11% except for Ti, which is 5–20% low in our laser data. The difference in Ti is thought to be due to poor counting statistics on the low Ti signals from the Ti-poor NIST 612 calibration standard.

One possible pitfall of in situ methods for obtaining bulk analyses of micro-objects in thin/thick sections using ASEM, EMPA, or LA-ICP-MS is that we do not know the chemical homogeneity of the object with depth, and must assume that the section we see is representative for the bulk chemistry of the whole, as we are analyzing three-dimensional objects in the two-dimensional image of a thin section. Thus the disadvantage of these methods is the possibility of non-representative sectioning of inhomogeneous or coarse-grained objects. As a result, bulk data may be non-representative. Although we always tried to approach the true bulk value by taking large numbers of analyses, depending on the homogeneity and grain size of each individual object, the bulk analyses gained by EMPA, ASEM as well as LA-ICP-MS should be considered as the best approximation we could get to the actual bulk elemental contents. These facts should always be kept in mind.

3. Results

3.1. Petrography

This study focuses on non-porphyritic chondrules, chondrule fragments and related objects in unequilibrated ordinary chondrites (UOC). The diameters of the analyzed objects range from about 40 μm to 2.5 mm. Shapes of objects vary from well-rounded (spherical to ellipsoidal) to irregular. Based on these variations, the objects were classified into the following four groups: (a) chondrules (C); (b) chondrule fragments (CF); (c) irregular objects (IO), which do not show any evidence for having once been part of a spherical object, but which have textures similar to those of chondrules; (d) unclassified objects (U), which are objects that do not show any evidence of having been broken off a former large object and which are texturally and/or compositionally distinct from non-porphyritic chondrules, e.g., with crystals up to 80 μm or objects containing large amounts of metal and sulfide. The principal petrographic characteristics of all studied objects are listed in Table 1 and Appendices A–D.

The dominant silicate phases of the objects investigated are olivine, low-Ca pyroxene, high-Ca pyroxene and glass or devitrified glass. Metal and sulfides, which usually occur in minor to trace amounts inside the objects, are Fe–Ni metal (kamacite, taenite, and subordinate tetrataenite) and troilite (FeS). Accessory phases are chromite and apatite.

Grain sizes of mineral phases range from <1 μm to a maximum of about 20 μm, except for barred olivine chondrules (which contain coarser-grained olivine bars) as well as some unclassified objects. In some cases single large grains of minerals are present (e.g., KR2, TS27, SO14, KN7, SA2, SA8).

In *crypto-crystalline objects* phases are too fine-grained to be resolved with an optical microscope at low magnification. Crypto-crystalline objects are rare in our collection; objects TS37 and KR3 belong to this group. Other objects, like SO12, BP5, TS24, and TS28 are very fine-grained (around 1–2 μm grain size) and the textures can be regarded as transitions between crypto-crystalline and fine platy, fine granular, dendritic or fibrous textures. Crypto-crystalline or very fine-grained objects may also show a radiating structure with occasional multiple extinction domains. Examples for crypto-crystalline and very fine-grained objects are shown in Figs. 1a and 1b.

In certain objects olivine or pyroxene grew with *fibrous morphology*. A typical habit of the fibers is numerous radiating, optically continuous crystals, with one or more eccentric locations of the radiation center (Fig. 1c). There are transitions between fibrous and granular textures (depending on the section plane), as well as fibrous and platy textures (depending on the size of the fibers/plates). In some objects both fibrous and granular crystal shapes are present. Examples of objects with fibrous textures are BP3, BP6, BP7, MM10, TS10, TS14, and SO1.

Objects with *granular textures* usually are composed mainly of closely packed anhedral crystals of olivine and/or pyroxene with interstitial mesostasis (Fig. 2a). The grain size can vary between very fine-grained (see above) to coarse-grained. Some granular objects are texturally similar to porphyritic chondrules (e.g., BP2) and in certain objects transitions between granular textures and platy textures (e.g., TS20, TS27), or between granular textures and fibrous textures (e.g., MM11, TS10, TS14) can be observed.

In many objects either pyroxenes or olivines grew with *platy habit* (Fig. 2b). One important group of objects with platy textures is barred olivine objects, consisting of parallel plates of olivine (which usually are optically continuous under the optical microscope) with interstitial glass, who are commonly enveloped by an olivine mantle. Examples of barred olivine objects with coarse platy textures are KR14 and SO4. Fine platy textures occur for example in SO1 and SO12. Examples of objects with pyroxene plates and with or without interstitial glass are KR5, KR6, KR7, BP4, TS20, TS27, and TS32 (Fig. 2b).

A special kind of *platy fibrous combined with granular* textures occurs in TS32, SO6, and MM11: these objects consist mainly of partly barred olivine, with large low-Ca pyroxene grains in between the plates (subordinate phases include glass, metal and sulfide; e.g., Fig. 2c). Object SO9 consists mainly of platy pyroxene crystals with coarse olivine grains in-between.

Object KR12 is a barred olivine object which contains olivine crystals with *platy* as well as *skeletal shape* (Fig. 3a). Object TS24 has pyroxene crystals which form very fine dendrites (Fig. 3b).

3.2. Surface features

In several objects, the outermost part of the object—a mantle—is mineralogically or texturally different from the major part of the object. These mantles seem to be overgrowths. Frequently, one of the mineral phases is missing in the outermost parts (in pyroxene–olivine objects sometimes olivine is missing, or no glass or no metal and sulfide occur in the mantle e.g., BP7, MM10, and MM17). Object MM21 has an outermost mantle without olivine but with an additional very regular chromite zone.

Occasionally, the mantles or certain parts inside the objects are porous; usually glass or high-Ca px is missing (e.g., BP6, BP8, KR1, KR3, KR7, TS10, TS14, TS28).

In several objects an enrichment in FeO near the margin, as compared to the center part of the object, can be observed, usually in the form of additional olivine (usually a transformation of pyroxene to olivine; e.g., many objects in Sahara 97210 and MM4, MM12, MM15, TS37).

Different types of rims occur attached to many chondrules and objects, mostly fine-grained rims with a mineralogy similar to that of the chondrite matrix (Fig. 4a; e.g., attached to almost all Tieschitz-objects, BP4, BP6, and SO2). Usually, those rims also surround chondrule fragments. In some cases coarse-grained rims or thick olivine rims are present, usually consisting of olivines and/or other silicate phases (Fig. 4b, e.g., MM13). Occasionally, coarse-grained metal/sulfide is attached to the surfaces of objects (e.g., KR2, BP2, TS10, MM6, SO3).

Additional surface features in some objects are round depressions, which occur in KR1, KR7, TS14, MM2, and MM11 (Fig. 4c). Compound chondrules are not present among our collection of objects. The probability of finding compound chon-

Table 1
Bulk trace element analyses: summary of characteristic features of all objects

Chondrite	Refractory TE	Eu-Sr-Ba	Mn-V-Cr	U	Rb-Cs-W
Bishunpur LL3.1 (8 objects)	*From Zr to Mn:* Roughly flat in all studied objects	BP2, BP7, BP6: Sr-, Eu-, Ba- BP1, BP8: Sr-, Eu-, Ba-	BP2, BP6, BP7: V- BP1, BP8: Mn+		
Krymka LL3.1 (8 objects)	*From Zr to Lu:* Roughly flat in KR1, KR2 KR3, KR5 and KR14	KR5: slight Eu+, Sr- KR2: slight Eu-, Sr-	KR1, KR2, KR3, KR5: V-	KR5: slight U+	KR2, KR3, KR5: Cs-, W-
	KR6, KR7, KR7r: Zr-	Kr7: Eu-			KR7, KR7r: Cs-, W-
	KR6: Ce-, Nd-	KR6, KR7, KR7r: Sr-, Ba-	KR6, KR7, KR7r: Mn-, V-		KR6: W-
	KR12: 6–9 × Cl, RL		KR12: Mn-		
	KR14: 2–4 × Cl, TE				
Mezö-Madaras L3.7 (14 objects)	*From Zr to Lu:* Roughly flat in all studied objects	MM6: Sr-, Ba- MM5: Sr-, Ba+	MM6, MM7: 1.5–2 × Cl MM5: Mn-		MM6, MM7: Rb-, Cs-, W-
	MM2, MM11, MM15, MM12: 1–2 × Cl, RL	MM2, MM11, MM12, MM15, MM19: Eu-		MM15: U-	
	MM19: 5–8 × Cl, RL	MM19: Sr-, Ba-		MM2: U+	
	MM10, MM17, MM21: strongly fract. RL				
	MM10, MM17, MM21: strongly fract. REE	MM10, MM17, MM21: Sr-, Ba-	MM10, MM17, MM21: 1–2 × Cl	MM10, MM17: U+	MM10, MM17, MM21: Rb-, Cs-
		MM4: 10 × Cl, Sr and Ba		MM21: U+	
		MM4r: Eu-, Sr+, Ba+	MM4 = MM4r		
	MM22, MM13: 1 × Cl, slightly fract. RL	MM13, MM22: Eu+, Sr-, Ba-	MM22: 1.5 × Cl	MM13: U+	
Tieschitz H3.6 (12 objects)	TS27, TS32, TS27px: irregularly fract. RTE	TS32: Eu-, Sr-	TS27, TS32, TS27px: V, Cr: 3 × Cl		
	TS27, TS32, TS27px: Zr-, Hf-, Al-, Sc-, Ca-, Y-	TS27: Sr-, Ba-	TS27: Mn-		TS27: Rb-, Cs-, W-
	TS10, TS19: RLE slightly fract.	TS10,19: Sr-, Ba+	TS10, TS19: 1 × Cl		TS10, TS19: Cs, W: 1 × Cl TS10: Rb+
	TS26, TS24: Zr-, Hf-, Al-	TS26, TS24: Eu+, Sr-, Ba-	TS26, TS24: Mn+, Cr+; V: 1 × Cl		TS26, TS24: Rb-, Cs-
	TS20, TS28, TS47c: flat RTE	TS20, TS28, TS47c: Sr-, Ba: 1–2 × Cl	TS20, TS28, TS47c: 1–2 × Cl		TS20, TS28, TS47c: Rb-, Cs-, W-
	TS24, TS14: 1–2 × Cl, RTE	TS44, TS14: Eu-, Sr-, Ba-	TS44, TS14: Mn+, Cr+	TS44, TS14: U+	TS44, TS14: Rb-, Cs-
Sahara 97210 LL3.6 (14 objects)	*From Zr to Lu:* roughly flat in all studied objects			All objects: U+	SO7, SO9, SO7ua: Cs, W: 1.5–2 × Cl
	SO7, SO9, SO7ua: 1.5–2 × Cl, RL	SO7, SO9, SO7ua: Eu-, Sr-, Ba-	SO7, SO9, SO7ua, SO12: 1.5–2 × Cl		SO12: Rb: 285 ppm
	SO4, SO6: Flat TE at 1–2 × Cl	SO4, SO6: Eu-, Sr-	SO4, SO6: 1.5 × Cl		SO4, 6: Cs+, Rb+
	SO14, SO8: Flat RL: 2–3 × Cl	SO14, SO8: slight Eu-, SO14: Sr+ SO14, SO8: Ba: 1–1.6 × Cl	SO14, SO8: 1–1.6 × Cl		SO14: Sr+
	SO3, SO5, SO2ua: Irregular TE	SO3, SO5, SO2ua: Sr-, Ba-	SO3, SO5, SO2ua: Mn, Cr: 2×, V: 1 × Cl		SO3, SO5: Cs-, Rb-; SO2ua: Cs+, Rb+
	SO1, SO13: RL: irregularly fract.	SO1: Eu+, Ba+; SO13: Sr+, Ba+			SO13: Cs-, Rb-; SO1: Cs+, Rb+
	SO10, SO11: slightly irreg. 0.7–1.5 × Cl	SO11: Eu-; SO10: Sr-, Ba-	SO10, SO11: 1–1.5 × Cl		

Abbreviations: TE: trace element; RL: refractory lithophile; RTE: refractory trace element; fract.: fractionated; ua: unaltered portion; irreg.: irregular; E-, E+: negative and positive abundance anomaly for element E.

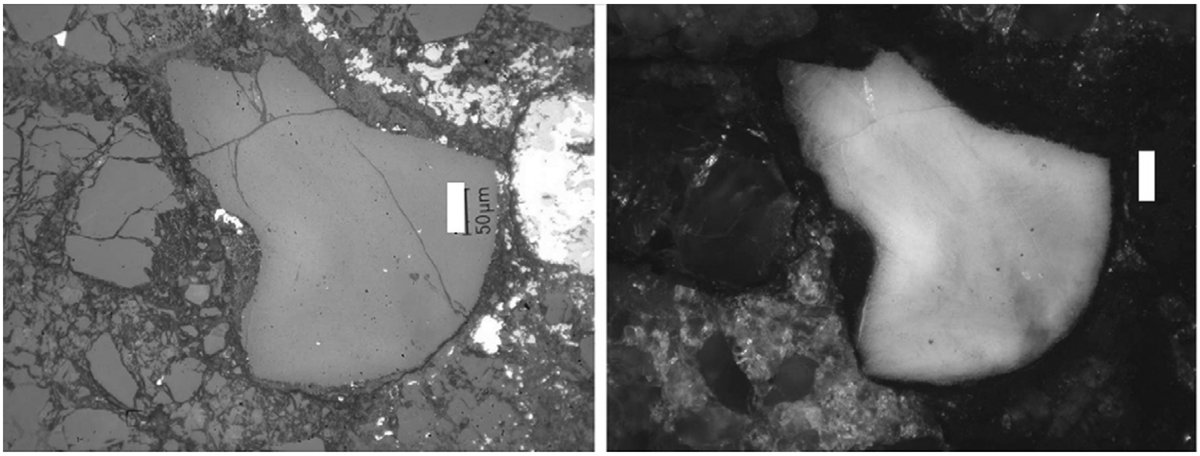

(a) Tieschitz TS 37

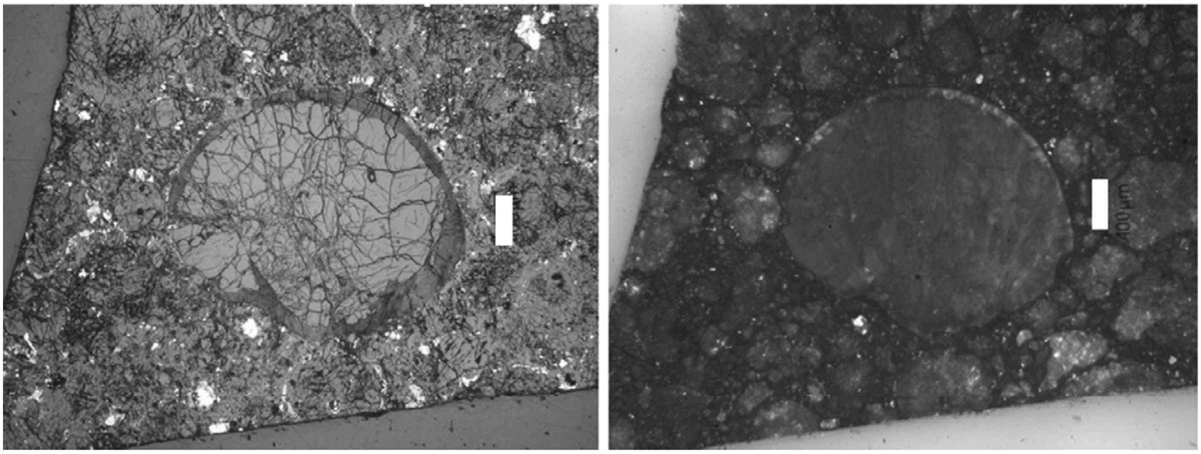

(b) Krymka KR3

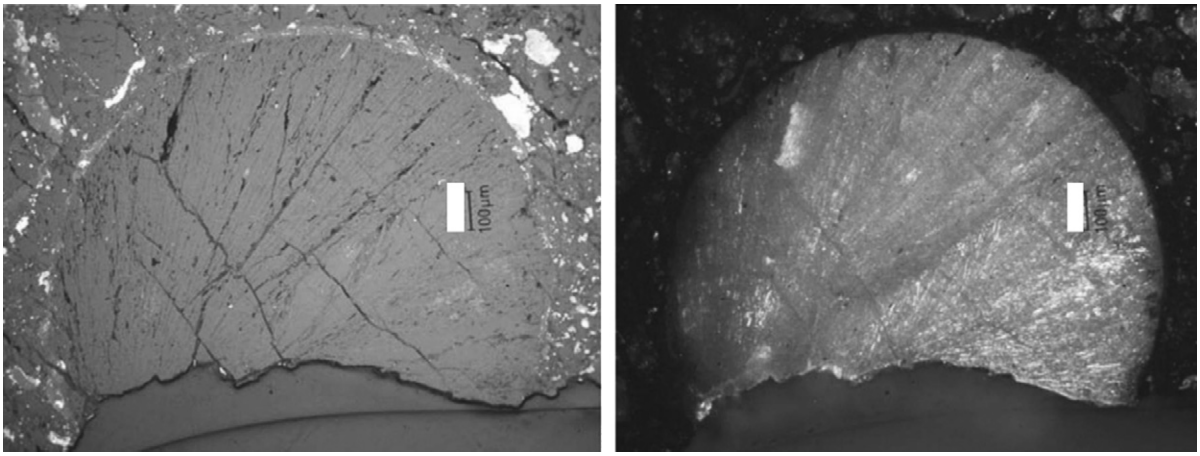

(c) Bishunpur BP6

Fig. 1. Objects with (a) crypto-crystalline—Tieschitz TS 37, scale: 50 µm; (b) fine-grained granular—Krymka KR3, scale: 400 µm; and (c) fibrous (eccentric-radiating)—BP6 (Bishunpur), scale: 100 µm textures. Optical images in plain reflected light (left) and under crossed polarizers (right).

drules in these randomly oriented thin sections is low (Ciesla et al., 2004).

The petrographic characteristic of all 56 objects of Tieschitz, Mezö-Madaras, Krymka, Bishunpur and Sahara 97210 are listed in Appendices A–E, where all-important petrographic observations are given. Numbers given for round depressions in chondrules refer to the diameters of the depressions, and numbers given for mineral size in barred olivine objects refer to the width of the olivine plates. The term “glass” is used for glass and slightly devitrified glass, whereas “mesostasis” (mes) is used for devitrified glass. For the textures of objects the terminology of Gooding and Keil (1981) was used: C for crypto-crystalline objects, G for granular objects, R for radiating objects, B for barred objects and P for porphyritic objects,

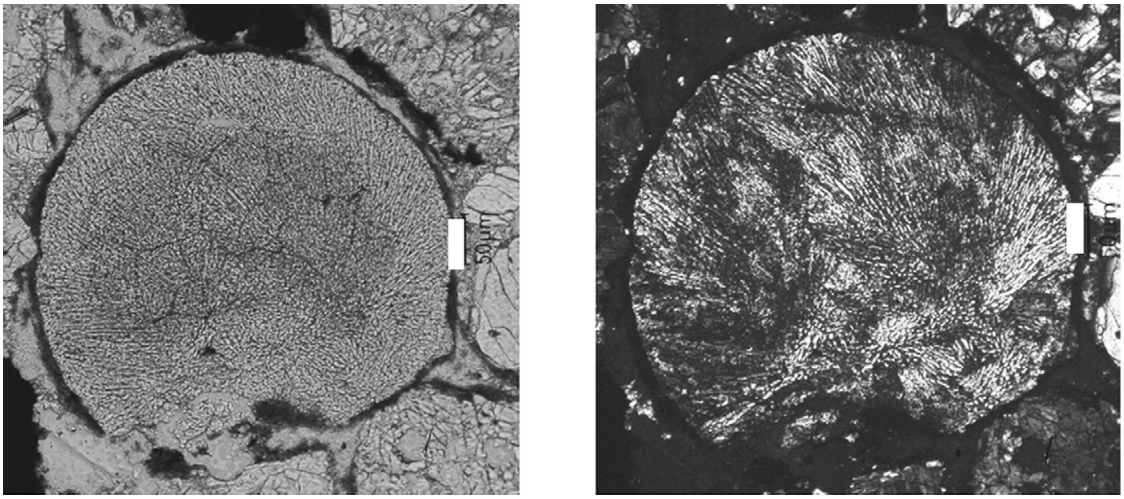

(a) Tieschitz

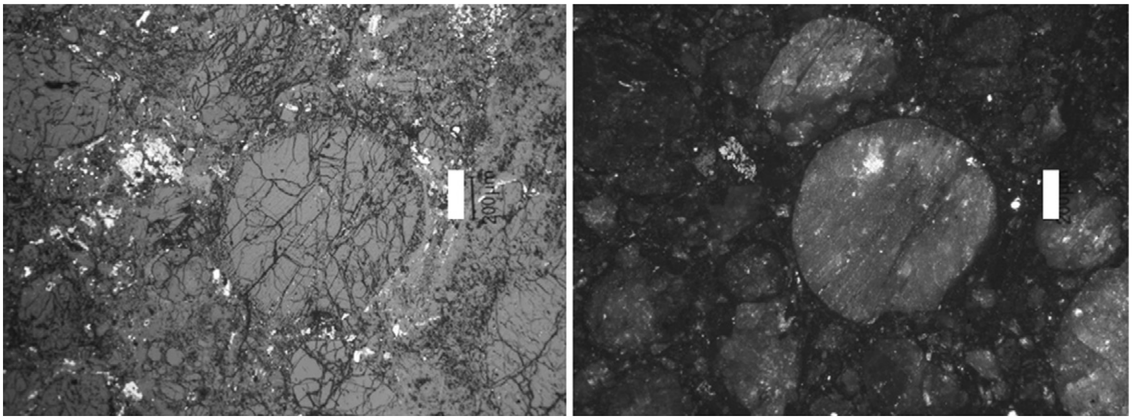

(b) Krymka KR7

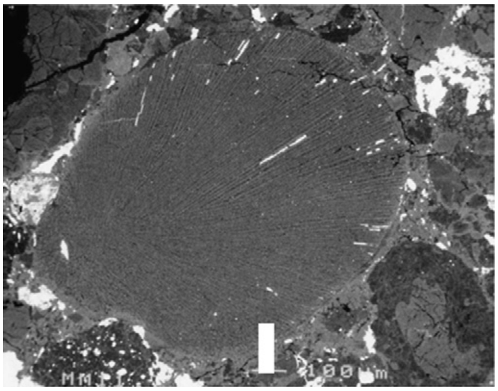

(c) Mezö-Madaras MM11

Fig. 2. Objects with (a) granular (Tieschitz), scale: 50 μm and (b) platy pyroxene (Krymka KR7), scale: 200 μm textures. Left: Optical images in plain reflected light (left) and under crossed polarizers (right). (c) Platy combined with granular (Mezö-Madaras MM11) textures, scale: 100 μm. Back scattered electron scanning (BSE) picture.

followed by either P for pyroxene and/or O for olivine (as major phases); M, S means metal and sulfide, respectively.

4. Major and minor element analyses of object phases

Major and minor element (ASEM and EMP) analyses of phases (olivine, low-Ca pyroxene, high-Ca pyroxene and glass/mesostasis) were performed on all the 56 objects. As the study was focused on non-porphyritic chondrules, it was difficult or even impossible to obtain quantitative phase analyses in crypto-crystalline, fine-grained, fine-prismatic or fibrous objects. Analyses as well as calculations of structural formulas are listed in Appendix B.

Chemical composition of *olivine* varies widely from object to object as well as within objects. The forsterite content ranges from Fo_{53} to Fo_{100}. Minor element contents range from 0 to

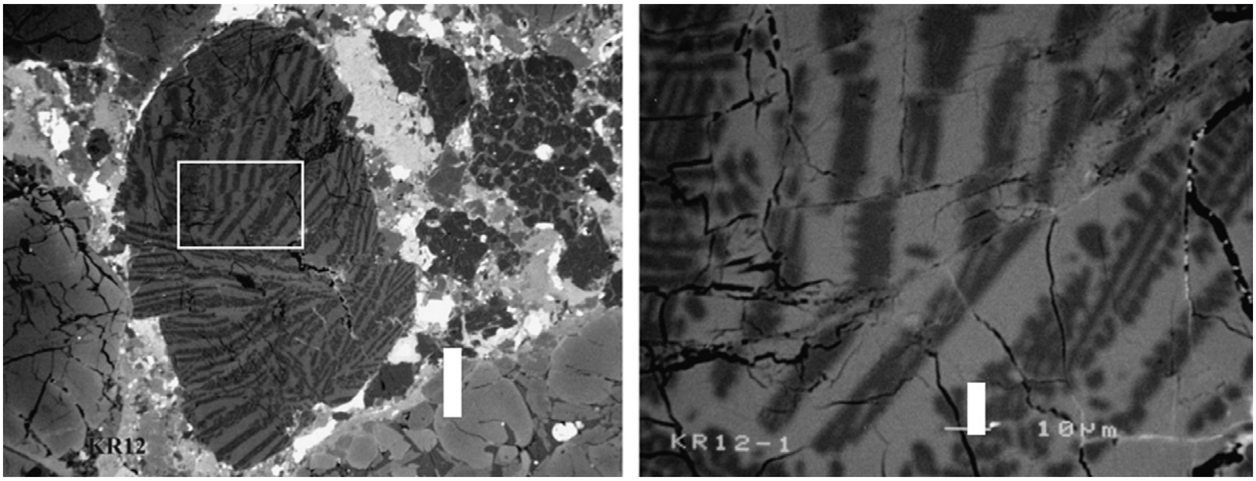

(a) Krymka KR12

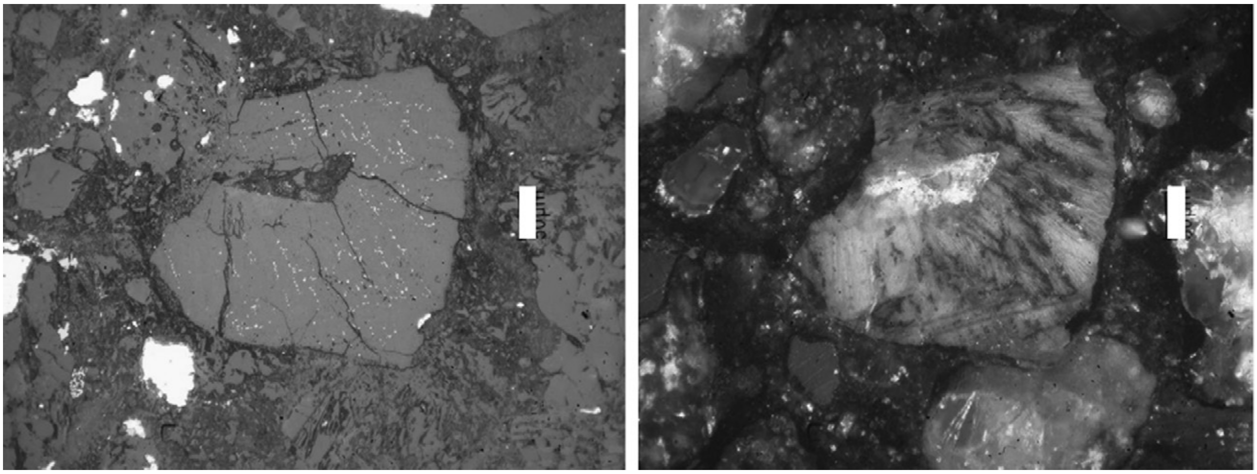

(b) Tieschitz TS24

Fig. 3. Objects with dendritic textures: (a) dendritic to platy (Krymka KR12), scale: 100 µm (scale inset: 10 µm); (b) dendritic to fibrous (Tieschitz TS24), scale: 50 µm. Optical images in plain reflected light (left) and under crossed polarizers (right).

0.7 wt% for TiO_2, 0 to 0.9 wt% for Al_2O_3 (except for some olivines in mantle-areas, which contain up to 2.3 wt% Al_2O_3) and 0 to 1 wt% for MnO.

*Low-Ca pyroxen*e occurs in objects of all chondrites investigated. We have observed a strong inter-chondrule variation in low-Ca pyroxene compositions with the enstatite content ranging from En_{57} to En_{97}. The Ti content ranges from 0 to 0.5 wt%, Al_2O_3 contents as well as Cr_2O_3 contents from 0 to 2 wt% and MnO contents from 0 to 1.5 wt% (Appendix B).

High-Ca pyroxene occurs mostly as rims surrounding low-Ca pyroxene cores, or as small grains, usually hosted by the glassy matrix. High-Ca pyroxenes are pigeonite to augite, and contain up to 21 wt% CaO (wollastonite component up to Wo_{47}). Titanium contents range from 0 to 1.8 wt%, Al_2O_3 contents reach a maximum of 12 wt% (except for pyroxenes in Bishunpur, which generally have lower Al_2O_3 contents, with a maximum of 2 wt%) Cr_2O_3 and MnO contents range up to 2.6 wt% (Appendix B).

Glass and recrystallized mesostasis are chemically heterogeneous from chondrule to chondrule, and sometimes even within the same chondrule. The SiO_2 contents vary from 50 to 76 wt%, the Al_2O_3 contents range from 0 to 30 wt%, Na_2O contents from 1 to 11 wt% and CaO contents from 0 to 17 wt%. With respect to the abundances of CaO, Na_2O, K_2O as well as Al_2O_3, SiO_2, FeO, and MgO in different glassy phases, almost all glass compositions deviate from the primitive Cl composition (Appendix B).

5. Bulk major and minor element analyses

Bulk major and minor element compositions of individual objects were obtained by ASEM and EMPA on polished thick and thin sections. Analyses of individual objects are listed in Appendix C. Calculations of normative compositions of individual objects were performed with the program MINPET 2.02 (Richard, 1995).

Major element chemistry of objects in all studied chondrites is dominated by Si, Mg, Fe, Al, and Ca. Objects from all chondrite classes show a considerable variation in composition. The SiO_2 contents range from 46 to 61 wt%, Al_2O_3 contents from 0 to 5 wt%, except for two barred olivine objects in Mezö-Madaras (MM19) and Krymka (KR12) which have Al_2O_3 contents up to 12 wt%. FeO and MgO contents vary from 3 to

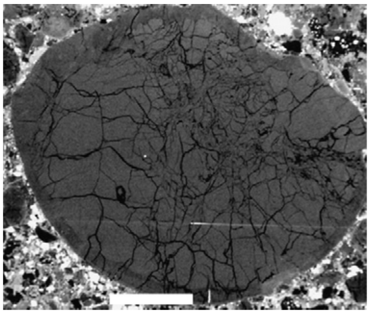

(a) Krymka KR3

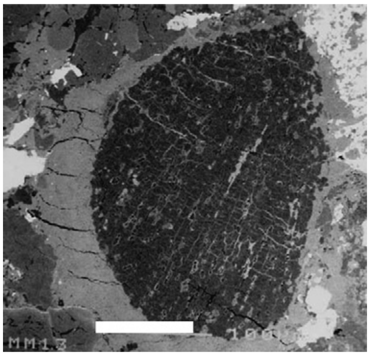

(b) Mezö-Madaras MM13

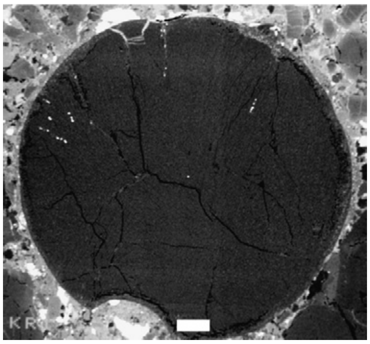

(c) Krymka KR1

Fig. 4. Different types of rims on UOCs objects: (a) object with porous mantle (Krymka KR3), scale: 500 µm; (b) thick olivine rim (Mezö-Madaras MM13), scale: 100 µm; and (c) an example of an object with a round depression (Krymka KR1), scale: 70 µm. BSE images.

31 wt% and 18 to 40 wt%, respectively. CaO is present at low concentrations and ranges from 1 to 3 wt%.

The Na_2O contents reach a maximum of 5 wt%, with 27 objects out of 56 containing >1 wt% Na_2O (SO1, SO2, SO12, BP2, BP3, BP4, BP5, BP6, TS14, TS19, TS20, TS27, TS32, KR1, KR12, KR14, MM2, MM4, MM5, MM6, MM7, MM11, MM12, MM13, MM19, MM21, and MM22). There is no correlation between K_2O and Na_2O abundances and most of the objects have non-chondritic Na_2O/K_2O ratios. The majority of objects has a K_2O/Na_2O ratio higher than the chondritic ratio.

The compositional differences between objects in the different chondrite classes are presented in the ternary plot of SiO_2–($CaO + Al_2O_3$)–($MgO + FeO$) (Fig. 5a). The studied objects have relatively constant $CaO + Al_2O_3$ contents, except for the two barred olivine objects KR12 and MM19, as well as MM4, which have higher contents of $CaO + Al_2O_3$ as compared to all other objects. With respect to MgO and FeO, the ternary diagram of SiO_2–MgO–FeO contents shows a strong variation from FeO-poor objects towards the composition of Orgueil (Fig. 5b).

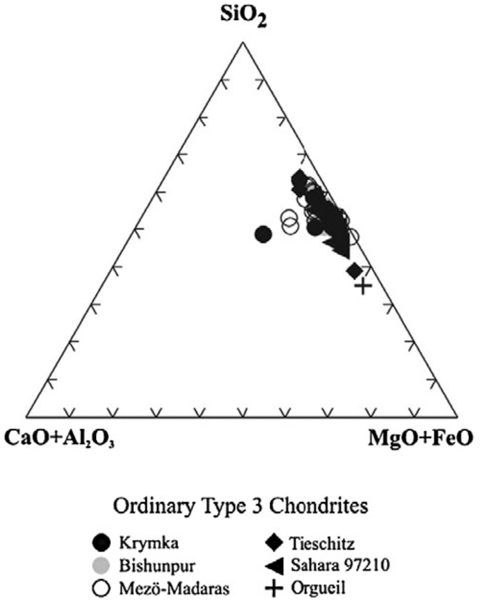

(a)

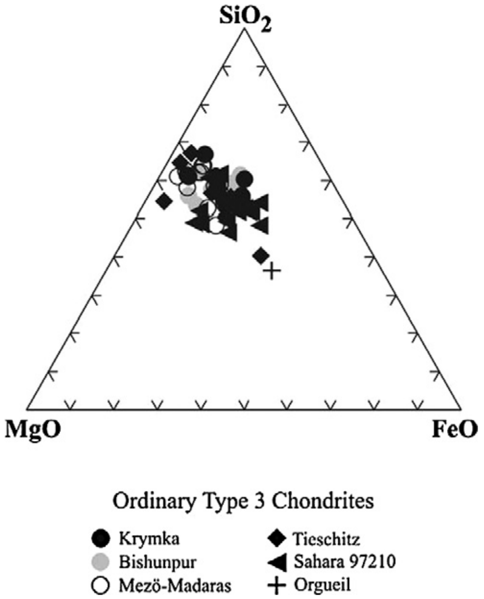

(b)

Fig. 5. Bulk compositions of UOCs objects projected onto the ($CaO + Al_2O_3$)–($MgO + FeO$)–SiO_2 (a) and the MgO–FeO–SiO_2 planes (b). Additionally, the bulk contents of Orgueil are plotted as a primitive, unfractionated reference material (Anders and Grevesse, 1989).

The bulk elemental abundances of CaO, SiO_2, MgO, and FeO are plotted against Al_2O_3, a reference refractory oxide, in Fig. 6. No chondritic trends can be seen among the objects of the different chondrites, except for CaO (Fig. 6a). Only a few objects maintain chondritic ratios relative to Al_2O_3. In terms of CaO vs Al_2O_3, the different objects of UOCs cluster around the CI-ratio line. Objects BP1, BP3, BP4, BP6, BP7, KR3, KR5, MM10, MM15, MM17, MM21, SO14, SO2, SO3, SO5, SO7, SO9, TS10, TS27, and TS32 have preserved a chondritic or

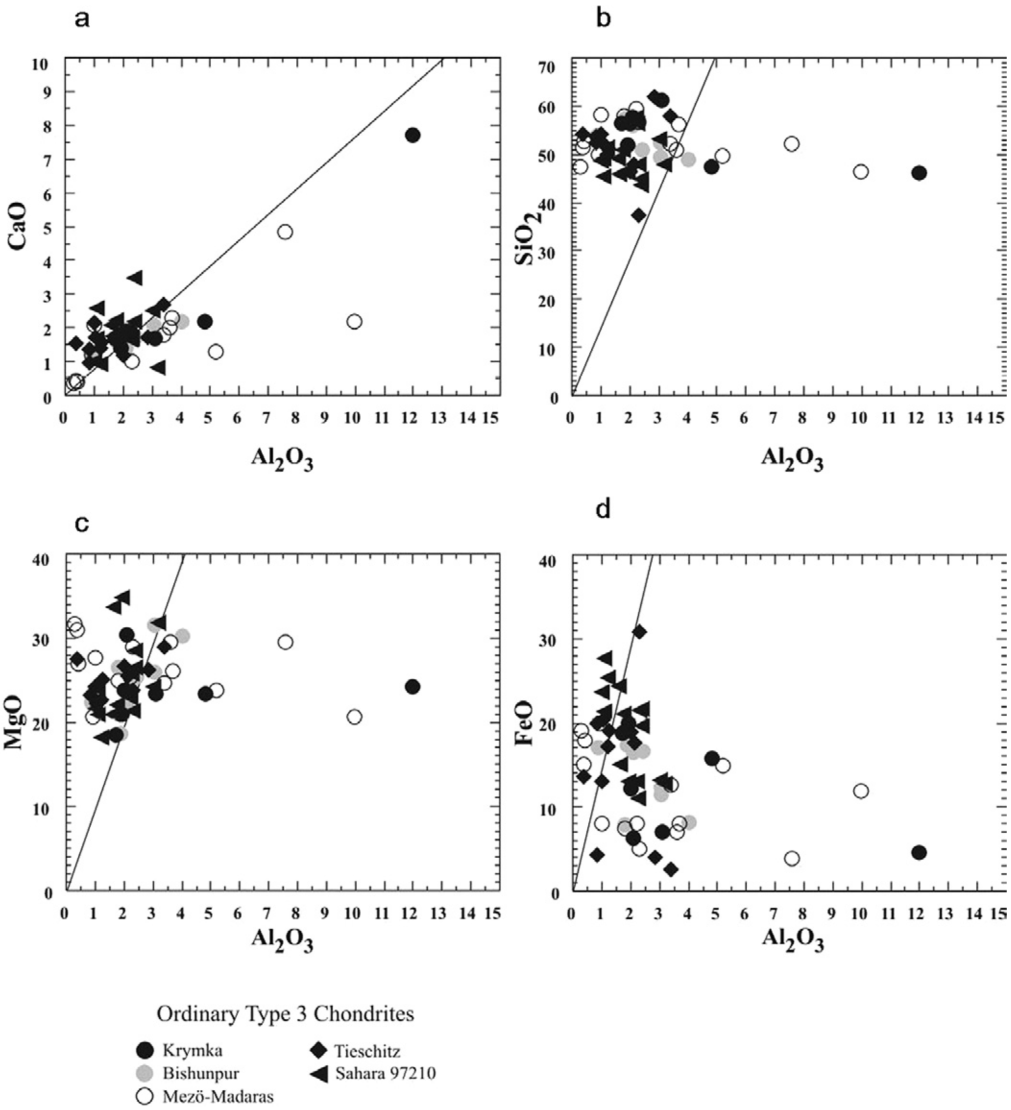

Fig. 6. Bulk CaO (a), SiO_2 (b), MgO (c), and FeO (d) contents plotted versus the Al_2O_3 content of objects in UOCs and compared to the respective Cl abundance ratio (Anders and Grevesse, 1989).

near-chondritic CaO/ Al_2O_3 ratio. The MgO/Al_2O_3 ratio of the majority of objects in UOCs is super-chondritic (Fig. 6c). The FeO/Al_2O_3 ratio (Fig. 6d) varies considerably among all the objects. Most of them have sub-chondritic ratios and only a few objects, like TS10, TS14, TS20 and TS28, have a chondritic ratio.

A summary of compositional features—inclusive trace element abundances—is given in Table 1.

6. Discussion

As already outlined in the Introduction, two principal models for the origin of chondrules in the solar nebula exist. In the first model chondrules are formed by melting of pre-existing solids (melting of solid precursors: MSP) during transient, locale heating events. Chondrule melts are considered either as closed systems which implies that their properties were established mostly by their precursors (e.g., Grossman and Wasson, 1982, 1983; Ikeda, 1983; Rubin and Wasson, 1987, 1988; Hewins, 1991; Kurahashi et al., 2004) or they went through open-system melting, with evaporation and interactions with the ambient gas as well as recondensation (e.g., Cameron, 1966; Whipple, 1966; Larimer, 1967; Larimer and Anders, 1967; Walter and Dodd, 1972; Gooding et al., 1980; Kurat, 1985; Grossman, 1988; Lu et al., 1990). In the second model, chondrules formed through direct condensation of solar nebula gas into liquids and crystals (e.g., Wood, 1962; Blander and Katz, 1967; Wood and McSween, 1977; Blander, 1983; Kurat, 1984, 1988; Kurat et al., 1996, 2004; Krot et al., 2001, 2002; Blander et al., 2005). However, the two open-system processes (melting with evaporation and recondensation, and the process of direct condensation) have also been considered as sub-processes of a single process (Huang et al., 1995).

Until recently, the major difficulty in accepting condensation models was that liquids were not considered stable equilibrium phases in a low-pressure solar nebula (e.g., Cameron, 1962; Grossman, 1972; Arrhenius and De, 1973). Beside silicate liquids, also FeO-bearing silicates (another major component of ferromagnesian chondrules) are not stable in a vapor of solar composition under nebular conditions. Extremely high total pressures ($p_{\mathrm{tot}} > 10^{-1}$ bar) or high enrichments in chondritic dust, relative to a vapor of solar composition, are needed to stabilize silicate liquids (Ebel, 2005) and oxidized Fe (Herndon and Suess, 1977). However, the nebula is now recognized to have been an inhomogeneous medium with local regions of enhanced condensable element to H ratios (e.g., dust enrichment, Herndon and Suess, 1977; Wood, 1985; Wood and Hashimoto, 1993; Krot et al., 2001; Petaev et al., 2001; Lauretta et al., 2002; Boss, 2006) and calculations of Yoneda and Grossman (1995), Ebel and Grossman (2000) and Alexander (2004) have shown that silicate liquids can condense from a solar nebula gas provided the dust/gas ratio is sufficiently high.

Based on studies of glass inclusions in olivines, Kurat et al. (1997, 2000), Varela and Kurat (2000, 2004) and Varela et al. (2001, 2002a, 2002b, 2003, 2005) confirmed the existence of liquids in the solar nebula and showed that their main role was to facilitate condensation of major silicate minerals from the solar nebula. The trace element pattern of these liquids (glass inclusion precursors) is refractory and has solar relative abundances with evidence for vapor fractionation of volatile elements. Based on these studies, a new model for chondrule formation has been proposed. The primary liquid condensation (PLC) model can explain how porphyritic olivine chondrules and aggregates (Kurat et al., 2004; Varela et al., 2005), as well as barred olivine chondrules (Varela et al., 2006) can be produced through direct condensation in one single nebular cooling step, without complex mixing of solids or remelting processes.

Besides the simplicity of the PLC model another difference with respect to the MSP model concerns the regions where chondrules could have been formed. In the MSP model, the porphyritic and non-porphyritic chondrules (Gooding and Keil, 1981) that may have formed from different precursor materials (Gooding et al., 1980), as well as some barred olivine chondrules and crypto-crystalline chondrules considered to be condensates (Krot et al., 2001, 2002), could have solidified in different regions of the nebula and then been brought together and incorporated into the final chondritic rocks. In the PLC model both chondrule types can be produced in the same region of the nebula, but during different evolutionary stages of the nebula and with different amounts of liquid involved. For porphyritic chondrules and aggregates only a small amount of liquid is needed to facilitate the growth of crystals and droplets of a crystal–liquid mixture are formed and solidify. If the quantity of early condensing liquid is enough to form a sizeable droplet, barred olivine chondrules can also be created in one step.

Here, based in the petrographic and chemical data of non-porphyritic objects from UOCs and supported by theoretical considerations, we discuss how in a late stage of evolution of the solar nebula with composition of the nebula gas having been changed due to crystallization of large amounts of olivine, liquid-only condensates can create the non-porphyritic ("all-liquid droplets") chondrules which have a mostly pyroxene-rich composition. In addition, we shall discuss the mechanism that lead to the practically unlimited chemical variability of chondrules and also chondritic constituents and describe the condensation calculations that indicate the conditions in which a pyroxene-rich liquid can indeed condense in the solar nebula.

6.1. Petrographic features

The shape and texture of chondritic constituents offer information about the primary nebula processes that formed them. The crypto-crystalline, granular, fibrous, platy and subordinated dendritic textures, the spherical to ellipsoidal shapes as well as the smooth surfaces of non-porphyritic chondrules indicate that those chondrules are quenched liquids. Strong evidence for the presence of liquids is also the glassy or crypto-crystalline mesostasis in many chondrules.

In pyroxene chondrules, granular and fibrous textures are in many cases probably the same textures, what we see is just a matter of view or cut, since the chondrules are three-dimensional objects.

On the surfaces of some objects *round indentations* are abundantly present (e.g., KR1, Fig. 4c). They can be interpreted (e.g., Gooding and Keil, 1981) as having formed by plastic deformation during chondrule collisions, which left circular depressions. This interpretation implies first, that chondrules which show a round depression probably formed in regions with high chondrule density, and second, that chondrules did not move with high relative velocity in space, so they did not disrupt each other when colliding, but rather stuck together, forming either compound chondrules (Wasson et al., 1995; Ciesla et al., 2004), which are rare in our collection, or left round depressions as they separated again.

Also, round indentations could be explained by immiscibility of silicate liquids and metal/sulfide liquids during high temperatures (melting or condensation, e.g., Grossman and Wasson, 1985). As a result of immiscible liquid formation a round metal spheroid is generated which we occasionally still can find in place. In the majority of cases it is lost, leaving behind the round indentation on the surface of the object.

A type of rim, which occurs on many objects, is either *fine-grained or coarse-grained overgrowths*. The latter are interpreted (e.g., Rubin, 1984) as having evolved through partial melting of pre-existing fine-grained dusty rims. Upon closer examination of many rims it is difficult to distinguish between the border of the actual object and the rim, because crystals are connected and sometimes even show evidence for epitaxial growth. Therefore, we suggest that those rims are not products of melting of pre-existing rims, but they grew on the surface of the chondrules in a combined process of aggregation and growth by condensation (with a certain amount of liquid). If a fine-grained rim surrounding a chondrule would have been sintered and melted, we should also see some evidence for this process in the texture of the chondrule or at least in the textures and distribution of metal–sulfide, since the metal–sulfide eutectic temperature is much lower than the melting point of silicates. Also, the overgrowths usually do not show the smooth surfaces typical for liquids, but have irregular surfaces, indicating diffusion governed growth. The overgrowths show that the temperature conditions in the nebula region in which the chondrule stayed for some time, were high enough for overgrowth formation. This can be taken as another hint for locally changing nebula conditions. Chondrule fragments which are completely surrounded by rims must have been fragmented in the nebula before rim formation and also before rock accretion. If fragments are only partly surrounded by rims, they obviously were broken apart after rim accretion but still before rock formation.

Some objects are surrounded by fine-grained accretionary rims, which can be considered as accretion of dusty matrix material onto the objects that must have occurred before incorporation into the chondrite, yet post-date chondrule formation. Those "envelopes" document that those objects have been at least for a certain time in a nebula region with high dust contents.

Another common chondrule feature are *mantles (rims) with different mineralogy or textures* compared with the main body (core) of the object. This can be due to overgrowths forming at a late evolutionary phase, when the chemical and physical conditions of the system had changed (olivine, glass or metal and sulfide can be missing; in MM21 an outermost portion with chromite occurs). But in most of the objects, mantles could also represent the results of metasomatic subsolidus reactions, as the object's outer portions could have reacted with the gas during open-system cooling. Chondrules have also been modified by secondary processes such as interactions between the chondrule and the nebular gas (e.g., replacement of olivine by pyroxene and vice versa) aqueous alteration or thermal metamorphism on their parent bodies (Kurat, 1969; Krot et al., 1995; Huss et al., 2006). In many cases we can see a Fe-enrichment near the surface which in some objects results from a reaction to form olivine from orthopyroxene (e.g., MM4, MM12, MM15, TS37 and many objects in Sahara 97210).

Some objects have *porous rims* (e.g., BP6, BP8, KR1, KR3, KR7, TS10, TS14, and TS28) which seem to represent regions that used to contain another phase, in many cases this seems to have been glass (see also Kurat, 1969). Glass appears to have somehow been "leached" out of the surface areas of the objects. In BP8 also porous regions exist inside the object with the original interstitial phase missing. The rim and two specific regions inside the object contain interstitial glass indicating that the precursor phase might have been glass. However, it is not clear why glass should break down inside the object and still remain in the rim as well as in those two regions. Probably it is a matter of primary porosity, permeability and composition of the leaching agent. Object TS10 lost part of its clinopyroxene (or maybe another additional phase) the same way as the other objects lost part of their glass. In two parts of this object clinopyroxene still exists and fills the space between olivines. In one region, metal and sulfide apparently secondarily filled the voids and substituted for clinopyroxene. Objects TS24 and TS26 have some large void spaces which appear to have contained a phase (with euhedral grain boundaries) that became unstable at a certain stage and broke down into mobile phases which disappeared without leaving any trace.

In summary, the petrographic observations reflect a very complex history of each individual object. The textures of non-porphyritic chondrules and objects indicate that the objects have to be quenched liquids. On the basis of the textures and petrographic observations we cannot distinguish between the main models of chondrule formation. However, one exception to this conclusion seems to be the overgrowths (also known as coarse-grained rims). If the overgrowths were generated through melting (e.g., Rubin, 1984) then, one of the questions that arise is, why was the chondrule interior not affected by the heating event? A possible answer is that overgrowths are the result of a condensation process. Then they could evolve like the chondrule itself by aggregation and growth during condensation, just with a smaller amount of growth-supporting liquid (Varela et al., 2006). Because the growth rates of crystals will depend on the relative amount of liquid (which will be different in different places of the chondrule's surface) and on the crystallographic orientation of the growing crystals, the result will be an irregular, lobate surface, a feature very commonly observed.

Features like the existence or non-existence of accretionary rims (dust-enriched environments), the porosity of some objects (loss of certain phases), changing mineralogy of mantle and cores (changing chemical and physical environment or a nebular metasomatic process) show that every chondrule has seen its own individual history in a changing and inhomogeneous environment which could have been the solar nebula. Because we can see certain properties of objects repeated in one chondrite, which do not occur in other chondrites, each chondrite seems to collect its objects from one particular region in the nebula.

6.2. *Major and minor element abundances*

The Al_2O_3 contents show no chondritic correlation with those of SiO_2, MgO or FeO, thus, objects tend to plot away from the solar ratios (Fig. 6). Only the CaO vs Al_2O_3 contents of the objects fall near the solar ratio line. A roughly chondritic correlation between CaO and Al_2O_3 contents has already been described by Fredriksson et al. (1997) for chondrules of different unequilibrated ordinary chondrites. As the oxides Al_2O_3 and CaO are both highly refractory, they should not be cosmochemically fractionated from each other. Thus, this correlation supports a condensation origin rather than a solid precursor melting origin in which chondrules should have sampled differing amounts of Ca-bearing and Al-bearing precursor phases, each of which would not have a chondritic Ca/Al ratio. The direct condensation model, in the other hand, predicts a chondritic Ca/Al ratio for the early chondrule, which carries these elements in glass inclusions and mesostasis in the chondritic, non-differentiated, proportions. Some barred olivine objects and objects with high glass contents have CaO/Al_2O_3 ratios much lower than the solar ratio (e.g., KR12, KR14, MM19, MM22, MM4 have high Al_2O_3 contents) suggesting subsolidus exchange reactions that mainly affected the CaO content—similar to what has been observed in glasses of glass inclusions in olivines and mesostasis of chondrules from CR and CV chondrites (Varela et al., 2001, 2005) and neck-inclusions and mesostasis of BO chondrules (Varela et al., 2006).

The majority of the objects has a SiO_2/Al_2O_3 ratio higher than the Cl ratio, the same holds for the MgO/Al_2O_3 ratio, both reflecting a control by ferromagnesian minerals. The high SiO_2

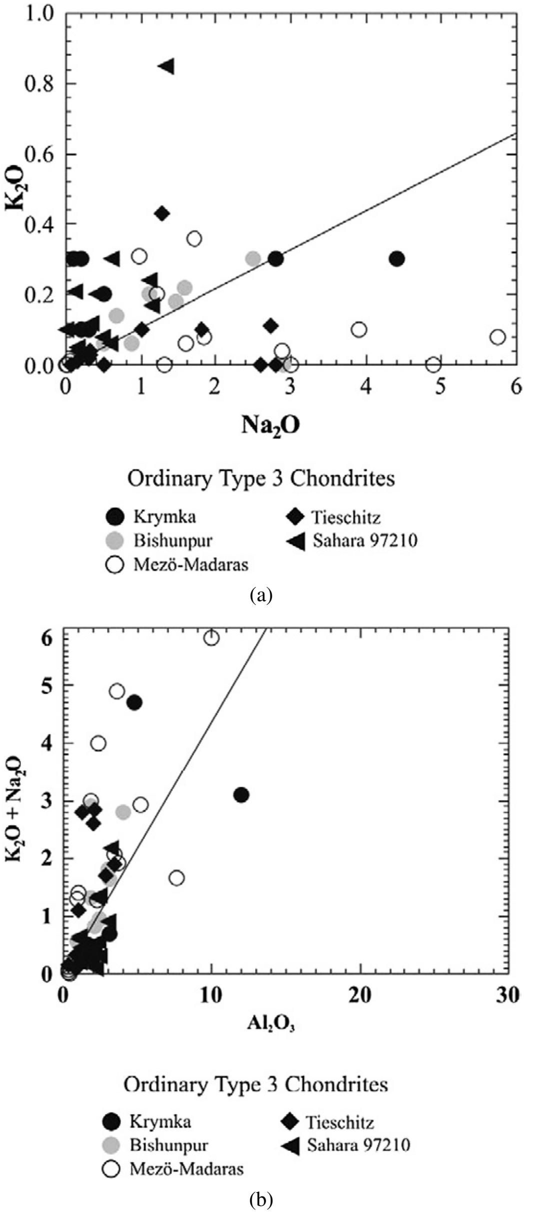

(a)

(b)

Fig. 7. (a) Bulk K_2O vs Na_2O and (b) bulk ($K_2O + Na_2O$) vs Al_2O_3 contents in UOCs objects compared to the CI abundance ratio.

content of all chondrules analyzed reflects their mineralogy (as we selected especially pyroxene-rich objects) and is therefore a primary feature of these certain types of chondrules. In contrast, the FeO/Al_2O_3 ratio is lower than the solar ratio in the majority of objects. Because FeO is not a stable species at conditions prevailing in the solar nebula, the large scatter in this ratio can reflects the chaos of secondary processing during which FeO is metasomatically added to different degrees at the expense of Mg. The fact that chondrules are generally richer in SiO_2 and poorer in Fe(O) than the bulk chondrites is well known and was already described by, e.g., Howard (1802), and more recently by Fredriksson et al. (1997).

The volatile K_2O and Na_2O contents of chondrules show no correlation with each other (Fig. 7a). In the majority of the studied objects the K_2O/Na_2O ratio is higher than the CI ratio, a phenomenon also observed in other chondrule types (e.g., Kurat, 1967). However, some objects lie on the CI ratio line, but since the scatter of the objects is high this is interpreted as stochastic. Thus, the volatile elements K and Na seem to behave independently from each other during chondrule formation, as is also suggested by the absence of correlation between volatile and refractory components in all studied objects ($K_2O + Na_2O$ vs Al_2O_3, Fig. 7b). For the melting of solid precursor (MSP) model of chondrule formation this fact implies that K, Na, and Al cannot have been added to the mix in one phase, such as feldspar, but rather need at least two phases. As Na and K cannot be easily separated in Al-bearing silicate systems (e.g., feldspars or feldspathoids will not discriminate Na from K) an exotic precursor mineralogy such as the one proposed for Chainpur chondrules by Kurat et al. (1984) is implied. On the other hand, metasomatic additions of alkalis from the vapor to the cooling chondrule should create all possible Na/K ratios just because Na and K have slightly different condensation temperatures (e.g., Wasson, 1985; Lodders, 2003). The final Na/K ratio of a given chondrule will depend on when and for how long it resided in certain regions of the nebula.

6.3. *Trace element abundances*

Individual objects in UOCs have variable abundances of refractory, moderately volatile and volatile lithophile trace elements (Table 1). Elemental abundances vary between 0.1 and 10 × CI, with the majority of the objects having elemental abundances between 1 and 2 × CI (Figs. 8–11). Exceptions are some highly fractionated objects in Tieschitz and Mezö-Madaras, which have lower abundances (mostly between 1 and $<0.1 \times$ CI, Fig. 9e), and some refractory barred olivine objects, which have trace element abundances up to 15 × CI (Fig. 8f). Normalized REE abundance patterns of all objects are either roughly flat (with or without a variably strong Eu anomaly, Figs. 8b and 9d), or irregularly fractionated (term used to denote that fractionation takes at least two steps and thus, cannot be called a regular fractionation). Moderately volatile and volatile lithophile elements are usually strongly fractionated and therefore show complex abundance patterns (either depleted or enriched with respect to the refractory elements, Fig. 9a). Abundance anomalies in refractory to moderately volatile elements are common and affect mainly the elements Eu, Sr, Ba, and U (Figs. 9b, 10c–10e, 11d–11e).

The only siderophile element of which the abundance could be measured is W (Table 1). Tungsten behaves as an incompatible volatile lithophile element under oxidizing conditions, similar to Cs and Rb but apparently with less mobility then the latter. Its abundance in the objects analyzed varies widely between non-detectable to about 4 × CI, but is usually low. Of the data obtained (from 34 objects) about 40% each are below CI or at about CI abundances, respectively, and only 10% (3 objects) are above CI abundance (up to 4 × CI).

6.3.1. *Characteristic trace element patterns*

(a) Objects with almost all elements at about chondritic abundances (1–2 × CI) (BP3, BP4, and BP5): This pattern

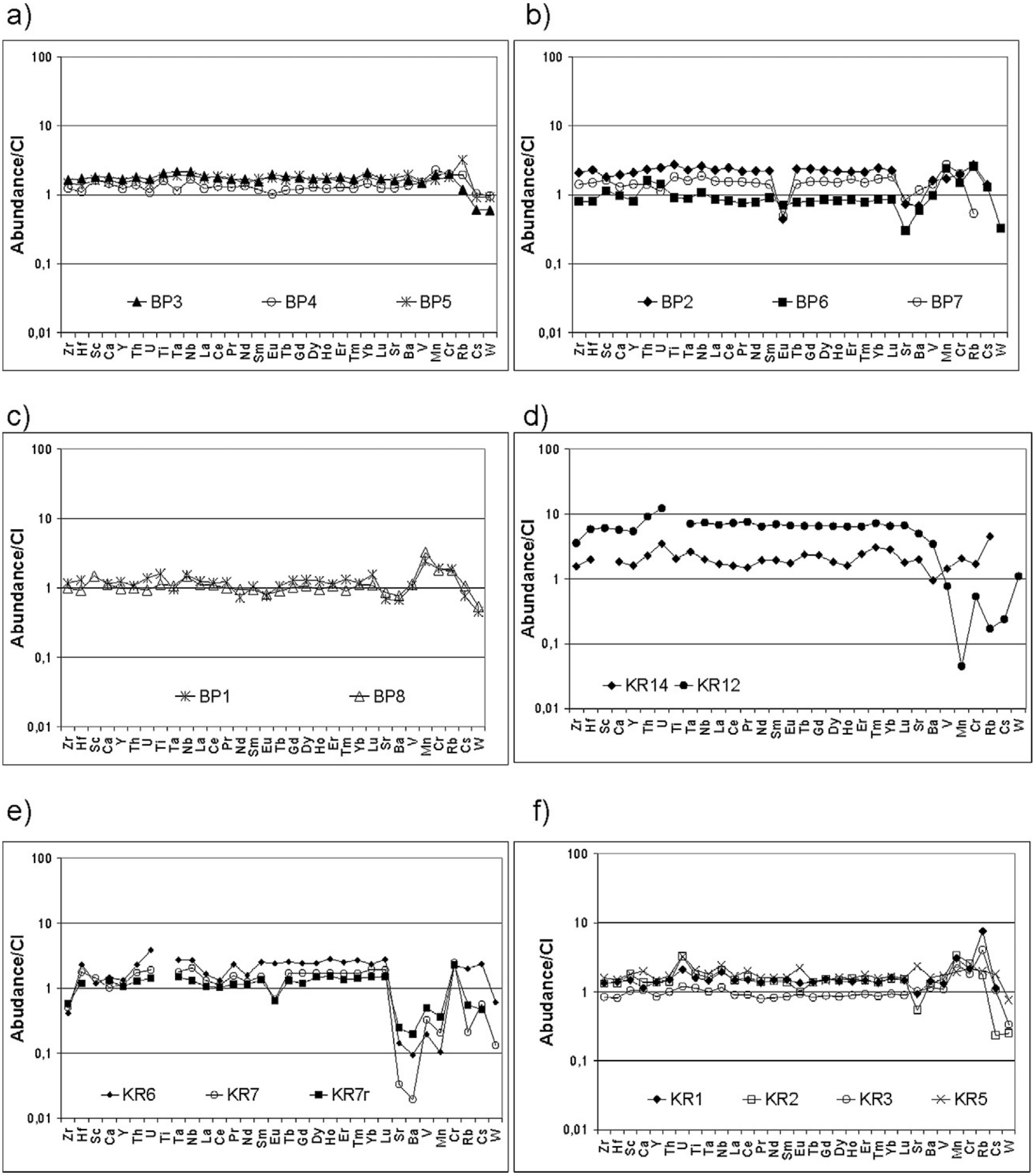

BP: Bishunpur, KR: Krymka, r: rim

Fig. 8. Bulk content of lithophile trace elements normalized to CI abundances [here and in the following graphs normalizing data were taken from Lodders and Fegley (1998)] in objects of the UOCs Bishunpur (a–c) and Krymka (d–f; all LA-ICP-MS data).

indicates that these objects retained the solar proportions of elements and that the moderately volatile and volatile elements equilibrated with the chondritic nebular source vapor. In these patterns we do not see any evidence for melting of solid precursors. If this was the mechanism that produced the pyroxene-dominated objects we would expect to see some evidence for trace element fractionation, especially enrichment in Sc and V or a depletion of the LREE, consistent with the modal mineralogy of the object. Object MM7 has a generally flat trace element abundance pattern (Fig. 9a), which can be interpreted as an unfractionated primitive pattern. Depletion of the most volatile elements Rb, Cs, and W suggests vapor fractionation. Objects SO4 and SO6 (Fig. 11b) have in addition a negative Al and a positive U anomaly, whereas Rb and Cs are enriched (this could also be due to terrestrial contamination).

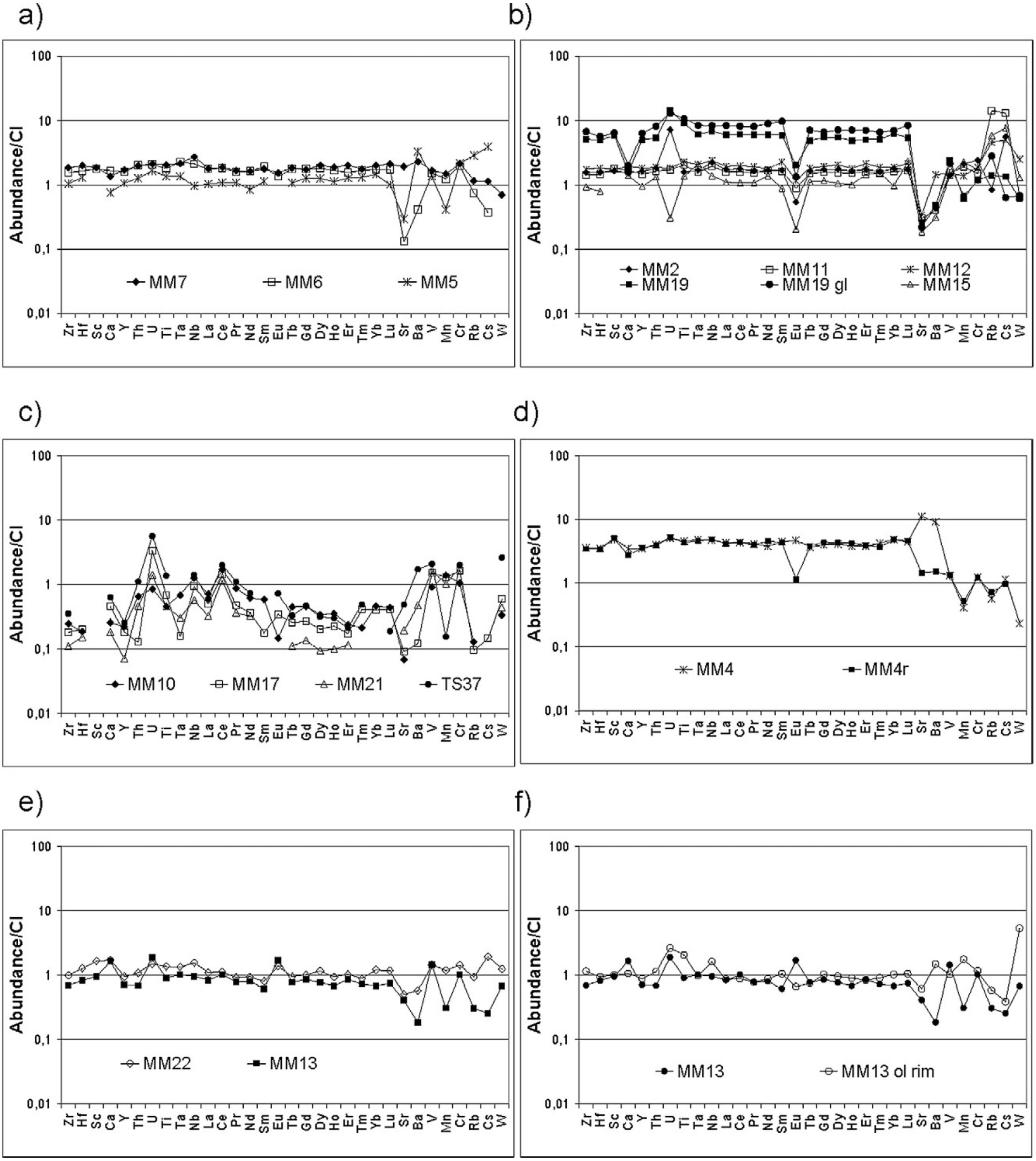

MM: Mezö-Madaras, TS: Tieschitz, r: rim

Fig. 9. Bulk and phase analyses of lithophile trace elements normalized to Cl abundances in objects of the UOCs Mezö-Madaras (LA-ICP-MS data).

(b) Objects with roughly flat refractory lithophile trace element abundance patterns (with some minor irregularities) and negative Eu, Sr, and Ba anomalies (BP1, BP2, BP6, BP7, BP8, KR6, KR7, KR12, KR14, MM2, MM11, MM15, MM12, MM5, MM6, MM19, MM22, MM13, TS27, TS32, TS10, TS19, TS26, TS24, TS14, TS44, TS20, TS28, TS47c, SO7, SO9, SO12). This kind of trace element pattern is the most common in our selection of objects. Because the elements Sr and Ba are more volatile than the REE, we interpret these anomalies as a consequence of vapor–solid/liquid fractionation. The same could hold for Eu. In objects MM2, MM11, MM15, and MM12, in addition to the negative Eu anomaly, a negative Yb anomaly occurs. This could be—combined with the negative Eu anomaly—an additional, strong evidence for fractionation due to the volatility of the elements.

In two objects (KR6 and KR7), the depletions in Sr and Ba are strong and are accompanied by Mn and V depletions and in

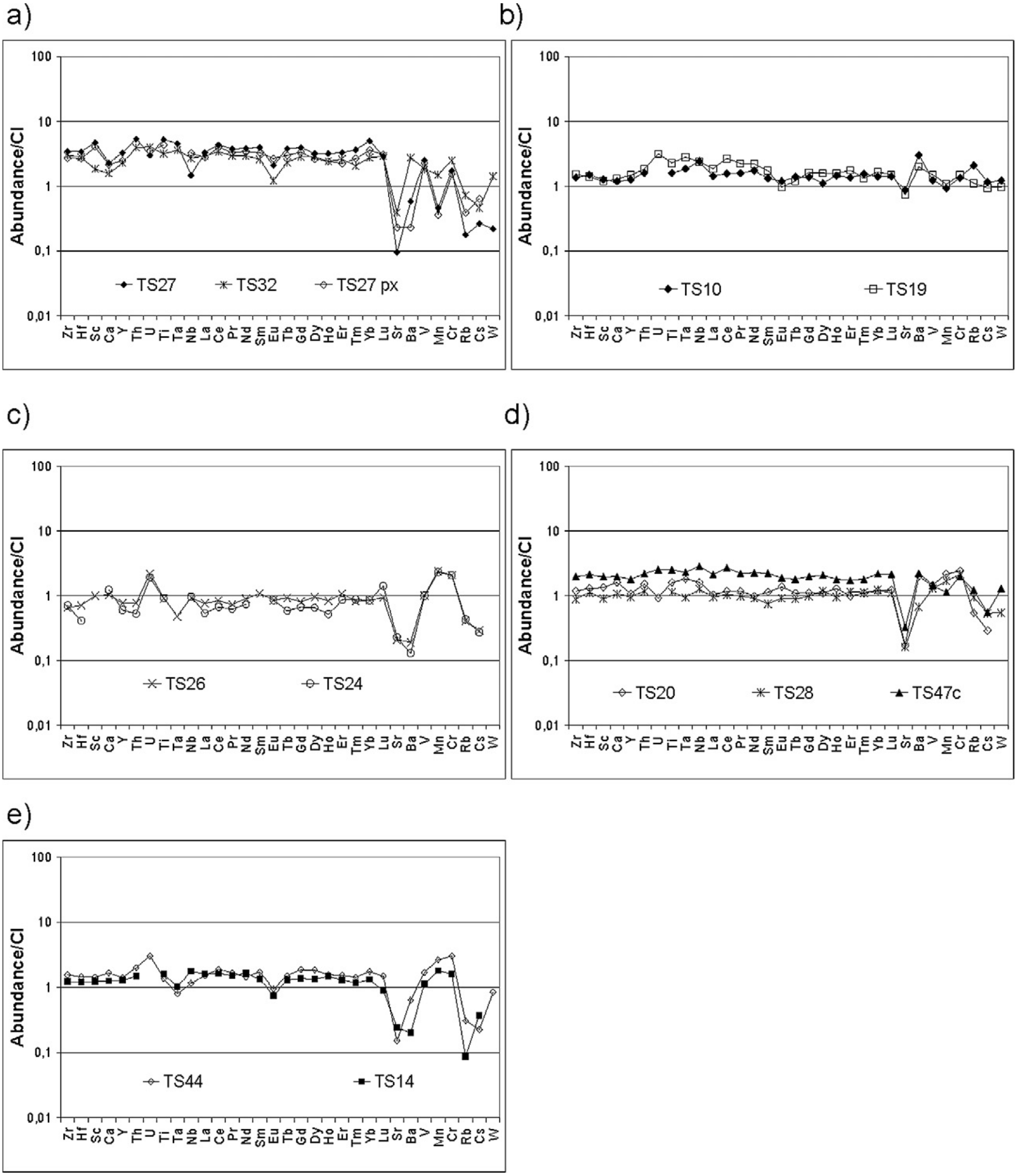

TS: Tieschitz, C: core

Fig. 10. Bulk and phase analyses of lithophile trace elements normalized to CI abundances in objects of the UOCs Tieschitz (LA-ICP-MS data).

KR7 also a negative Eu anomaly. This kind of pattern can be interpreted again as vapor–solid/liquid fractionation, since this fractionation seems to be due to the volatility of the elements depleted (Lodders, 2003). KR12 (Fig. 3a) and KR14 are barred olivine objects. They are enriched in refractory lithophile elements, which are carried by the glassy mesostasis. Object KR12 shows a typical volatility dependent pattern with a relatively flat pattern for RLE and a depletion for VLE (Fig. 8f).

Object MM19 is a barred olivine object, which also contains minor amounts of pyroxene. In addition to the negative Eu, Sr, and Ba anomalies, it shows a negative Ca and a positive U anomaly. As the glass has a high Na_2O content (around 10 wt%) this could be evidence for a Na–Ca exchange reaction during late stage metasomatic processes in the nebula (e.g., Varela et al., 2005). For the combined Eu, Sr, Ba, and Ca anomalies a plagioclase fractionation can be ruled out, because the

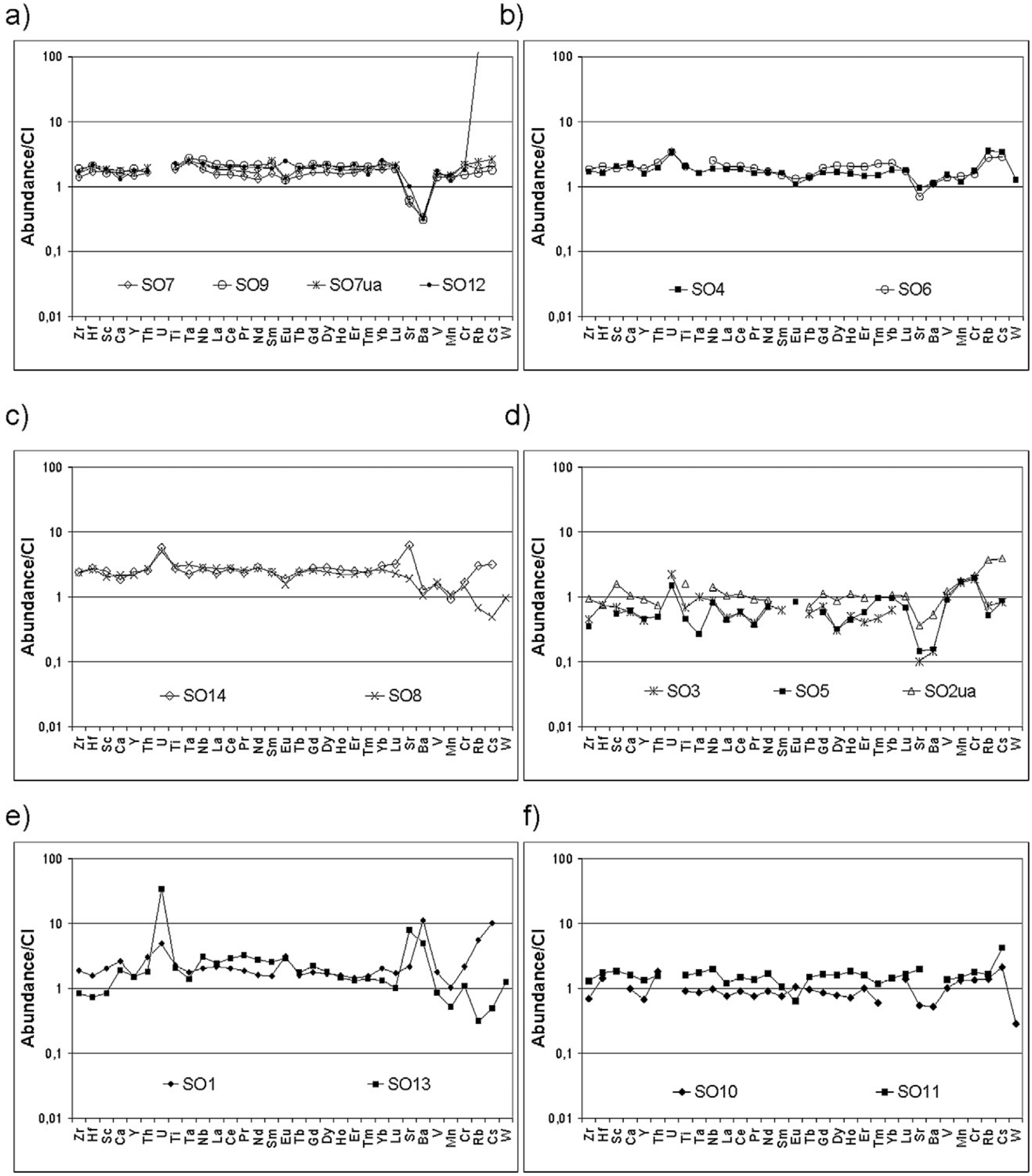

SO: Sahara 97210, ua: unaltered

Fig. 11. Bulk and phase analyses of lithophile trace elements normalized to Cl abundances in objects of the UOCs Sahara 97210 (LA-ICP-MS data).

REE are not fractionated but display a flat abundance pattern. Also in this object the abundances of volatile elements are irregularly fractionated, indicating independent behavior from that of the refractory elements.

Objects MM22 and MM13 have negative Sr and Ba abundance anomalies and positive Al and Eu (MM2) and Ca, U, and Eu (MM13) anomalies. Object MM13 is surrounded by a thick olivine rim. Interestingly, the chemical composition of the rim is similar to that of the central object, in particular for the REE contents (except for a slight negative Eu anomaly instead of the positive Eu anomaly of the object itself). Additionally, the olivine rim has a positive Nb anomaly as well as a positive Mn anomaly. But the element contents of the olivine rim should be interpreted with care, because the analysis intervals were very short due to the fact that the laser was burning through the object (in a thin PTS) very quickly.

In objects SO7, SO9, and SO12 volatile element abundances are unfractionated, which could indicate either that they retained solar abundances during object evolution, or, what seems to be more probable, that they equilibrated with a system with chondritic elemental proportions, by subsolidus metasomatic elemental exchange.

(c) Objects with variations in the moderately volatile elements Mn, V, Cr, Rb, and Cs: Almost all objects from the studied UOC show irregular abundance variations of the moderately volatile elements, which are probably due to incomplete late stage metasomatic processes. These elements are mobile and are involved in metasomatic vapor–solid exchange processes—as is FeO, which we already discussed above as a major element.

For many Mezö-Madaras objects, Mn, V, and Cr have abundances around 1–1.5 × Cl, which is a characteristic features for them. Addition of these elements must have taken place for almost all objects under similar conditions. This suggests that V and Cr have either never fractionated from the original ratio in all Mezö-Madaras objects, or more probably, that V and Cr equilibrated in all of the objects within a chondritic, closed system. Because these elements are olivine and pyroxene compatible, their concentrations in the objects apparently easily equilibrate with the nebula.

Objects TS26, TS24, TS14, and TS44 have a distinct pattern for Mn, V, Cr, Rb, and Cs. The elements Mn and Cr are enriched, whereas V is close to the Cl value, Rb and Cs are depleted. These similarities show that those objects must have experienced a similar evolution history; however, they do not show the same textures and mineralogy. Thus, these features obviously are not governed by the high-temperature formation event but rather by subsolidus elemental exchange reactions that affected all objects, regardless of their origins. Early separation of these objects from the vapor prevented the full acquisition of the volatile elements Rb and Cs.

In Sahara 97210 objects (Fig. 11), a characteristic feature in the trace element pattern compared to those of other UOC objects is that the moderately volatile elements Mn, V, Cr, Rb, and Cs are less depleted. They are either nearly unfractionated or enriched relative to the RLE, suggesting that they fairly effectively equilibrated with a system with chondritic elemental proportions, by subsolidus metasomatic elemental exchange.

(d) Objects with a positive U anomaly (KR5, KR6, KR12, KR14, TS26, TS24, TS44, SO1, SO4, SO5, SO6, SO8, SO13, SO14). This anomaly seems to be common in many objects of chondrites. The reason is not clear but possibly also related to volatility. In the objects KR6, KR7, KR12, and KR14 the most refractory element Zr is depleted. This could be due to separation of an earlier solid refractory condensate from the gas.

Objects from Sahara 97210 (SO) could carry a terrestrial contamination because the U(+) anomaly occasionally is accompanied by Sr(+) and/or Ba(+) abundance anomalies.

(e) Objects with low trace element abundances and strongly fractionated patterns (MM10, MM17, MM21, TS37): Most of the normalized element abundances of these four objects are below 1 × Cl (Fig. 9c). Positive anomalies in U, Nb, and Ce abundances occur and the HREE are depleted relative to the LREE. Moderately volatile elements Sr and Ba are depleted relative to the LREE. These patterns could suggest fractionation via a mineral phase enriched in HREE as well as Sc and Zr (hibonite?). The positive Ce anomaly could also suggest vapor fractionation. Conditions prevailing seem to have been reducing, as indicate by the negative Eu anomaly. Thus, these objects could have evolved through condensation from a vapor depleted in refractory elements and Eu. However, redox conditions changed towards more oxidizing ones as indicate by the anomalies of Ce, Ti, and Ca. The positive Ce anomaly suggest that this element apparently was present as Ce^{4+} and became enriched in the vapor phase—because it is possibly less refractory than Ce^{3+} (Boynton, 1978; Davis et al., 1982)—and does not follow the other REE into the condensing phases. Note that the compatible moderately volatile elements Mn, V, and Cr have abundances in these objects that are comparable to those in most other objects.

(f) Objects with almost identical elemental abundance patterns but with different mineralogy and texture (BP3, BP5, BP2, BP7, BP1, BP8, SO4, SO6, SO8, SO14). This characteristic feature is clear evidence for the fact that the trace element abundances and patterns do not correlate with neither textures nor the mineralogy of the objects. Objects BP3 and BP5 have almost identical abundance patterns in spite of the fact that BP5 contains low-Ca pyroxene and glass and BP3 contains additional olivine. The same holds for objects BP2, BP7, BP1, TS27, and TS32, and also TS10 and TS19. They share similar trace element contents, but are completely different in texture and mineralogy. Object SO4 is a barred olivine object and SO6 a barred olivine object with additional coarse grains of low-Ca pyroxene, however, they have almost identical trace element patterns. Another pair of objects that fulfills this characteristic feature is SO14 and SO8, except for a positive Sr, Rb, and Cs abundance anomalies observed in SO14.

(g) Objects with evidence for secondary terrestrial processes: Several objects in Sahara 97210 (the only find among our samples) show this evidence, like the strong positive U anomaly in SO13, the positive Sr and Ba anomalies in SO1 and SO13, the fractionated REE in SO13 as well as the high Rb content of SO12 and SO1 (but the high Rb content of SO12 could also be an analytical artifact, because the object lies on a very thin region of the thin section, where the laser was burning through very quickly). Also object SO14 has a combined positive U and positive Sr anomaly, which is probably due to terrestrial alteration. The enrichment of U, Sr, and Rb and Cs in SO14 could probably be attributed to terrestrial contamination. The same can be seen in objects SO1 and SO13, where a positive U anomaly is accompanied by positive Sr and Ba as well as positive Rb and Cs anomalies in SO1. In SO1 (a very fine-platy barred olivine object, containing olivine and glass) additional positive Eu and Ca anomalies occur.

(h) Interesting pattern: An interesting trace element abundance pattern shows object MM4 (Fig. 9d). This object consists in the core of low-Ca pyroxene and glass, which seems to be the

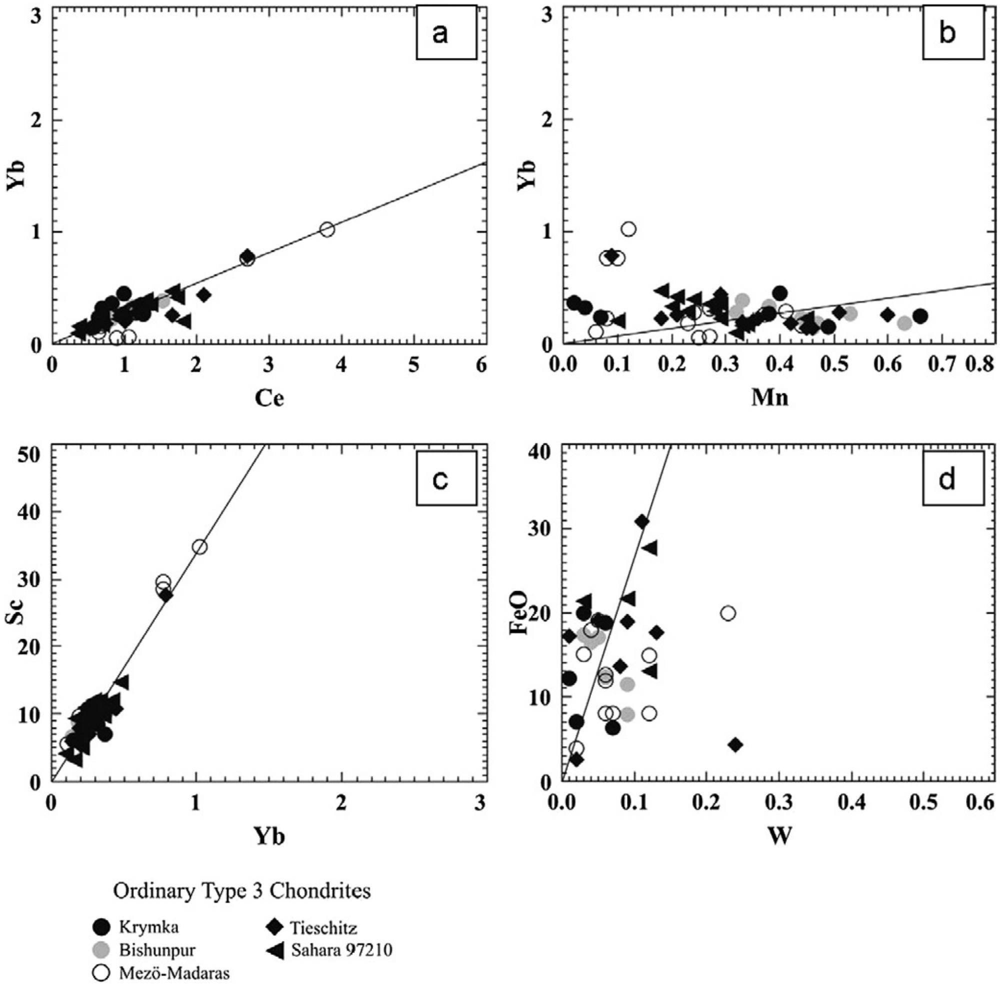

Fig. 12. Element correlation plots for Yb vs Ce (a), Yb vs Mn (b), Sc vs Yb (c), and FeO vs W (d) of object in UOCs compared to Cl ratio (Anders and Grevesse, 1989).

original phase composition. From the rim to the center, FeO is introduced due to a secondary metasomatic process which also changes the mineralogy of the chondrule:

$$\mathrm{MgSiO_3 + FeO = (Mg, Fe)_2SiO_4}$$
$$\text{(pyroxene + FeO = olivine).}$$

The center of the object is thus dominated by pyroxene and the rim is dominated by olivine. The center part with the primary mineralogy and the rim region with high olivine content show almost identical trace element patterns, except for Eu, Sr, and Ba which are depleted in the rim but in the central part Eu is unfractionated and Sr and Ba are enriched relative to the majority of the other elements. The abundance of the medium volatile elements Mn, Cr, Rb, and Cs are identical in both, core and rim, as is that of V, and all approach chondritic values. The abundances of Eu, Sr, and Ba apparently changed due to the reaction of pyroxene to olivine, and the object possibly acted as a closed system for Ba and Sr, redistributing these elements just between core and rim (pyroxene and olivine). Only Eu apparently was lost during the reaction causing a depletion of Eu in the rim.

6.4. *Trace element ratios*

Some trace elements with certain geochemical and cosmochemical behavior are plotted against each other for the objects of different chondrites in Fig. 12. The compatible/refractory element Yb is plotted against the incompatible/refractory element Ce as well as against the compatible/volatile element Mn, and the compatible/refractory element Sc. In addition, a comparison of FeO vs W contents (Fig. 12d) can shed light on the redox-conditions and the history of W. High FeO contents correlating with high W contents would indicate oxidizing conditions and secondary enrichment of W (in oxidizing conditions W becomes lithophile and is therefore incorporated into silicates), and low FeO contents correlating with high W contents could indicate primary features (Fegley and Palme, 1985).

The abundances of Yb and Ce as well as of Yb and Sc are clearly correlated and the composition of almost all objects lies on the solar ratio correlation line (Fig. 12). This indicates that those elements were not fractionated during evolution of the objects due to a similar cosmochemical behavior. The fact that Ce has a different geochemical behavior than the two other elements (it is incompatible in contrast to Yb and Sc which are compatible) and that in spite of this, it is also not fractionated from Yb is clear evidence against geochemical fractionation. The strong correlation between the abundances of RLE, independent of their geochemical behavior, indicates a predominance of cosmochemical processes determining the elemental abundances.

The contents of Yb and Mn (Fig. 12) show no correlation in the objects. Both elements are compatible but Mn is volatile in contrast to the refractory Yb. The decoupling of the abundances of these two elements cannot be due to geochemical processing but rather indicates volatility-controlled cosmochemical processes are responsible for their abundances. As we have already seen in other trace element diagrams, Mn is a mobile element and it is likely that it has been added to the objects by subsolidus metasomatic processes. The same holds for the oxide FeO (Fig. 12d): No correlation with W content exists and only very few objects lie on the solar line—their abundances are totally independent of each other. Thus, at least one of these elements, most likely Fe^{2+}, appears to have been added secondarily by subsolidus metasomatic processes. The surprisingly high abundances of W in some objects cannot be interpreted now because there is no obvious correlation between the abundances of W and RLE and any possible correlation between the abundances of W and refractory siderophile elements cannot be evaluated because of lack of data. However, because W abundance appear to be as stochastic as those of Rb and Cs, it shall also be considered to be an incompatible and volatile element, which W is under oxidizing conditions. The similarity between normalized W and (Cs) abundances is striking: $<$Cl: 15 (17), $\sim$Cl: 16 (14) and $>$Cl: 3 (19). This feature indicates that a similar process in supplying these elements was involved. The most likely is nebular metasomatism event, which added these elements to the objects. Oxidizing conditions are needed for W. The deficit in objects enriched in W simply could reflect the partition of W between an oxidized and a reduce reservoir. The non-existing correlation between W and Fe also indicates different reservoirs for these elements.

In summary, the majority of objects of the different unequilibrated chondrites shows mostly flat RLTE abundance patterns, with or without specific abundance anomalies. Objects with pyroxene-dominated mineralogy and thus fractionated SiO_2 and MgO contents but without fractionated REE patterns cannot be produced by mixing of solid precursors or by igneous fractionation, but could result from condensation. Consequently, most of the objects selected for this study appear to represent genuine liquid condensates from a vapor with solar relative abundances of refractory and moderately volatile elements. The negative abundance anomalies of Sr and Ba are interpreted as vapor–solid/liquid fractionations, since Sr and Ba are more volatile than the RLE elements. Anomalies in the abundances of Eu, U, and Ca can indicate either a fractionation by isolation of certain mineral phases (condensation from a fractionated nebula gas) or a mobilization of those elements during metasomatic processes. Another possibility would be fractional crystallization of certain phases, but for the origin of the combination of Ca, Eu, and Sc abundance anomalies, plagioclase fractionation can be ruled out because in this case the Eu anomaly is not accompanied by a Ca (Na) anomaly. In addition, the LREE should be depleted if plagioclase has been removed from the system, but this is not the case. Low Ca contents are commonly accompanied by high Na contents indicating effective nebular elemental solid–gas exchange.

Moderately volatile elements Cr and Mn and also V show similar behavior and have comparable abundances (between 1–2 × Cl) which are independent of the abundances of other elements in most objects. As these elements are also olivine/pyroxene compatible, their almost uniform abundances could indicate efficient metasomatic addition by vapor–solid equilibration with the chondritic nebular reservoir. The volatile elements are either depleted according to their volatility, which clearly indicates vapor fractionation (especially in barred olivine objects) or they have highly variable abundances and are strongly fractionated. This chaotic behavior is likely due to variable efficiency of metasomatic processes that took place during and/or after chondrule formation.

Some objects have flat element abundance patterns with practically all elements at about chondritic abundances—with some minor irregularities. These patterns could be the result of an almost successful equilibration of moderately volatile and volatile element abundances of a refractory condensate with the chondritic reservoir.

Fig. 13 shows the possible evolutionary history of the trace element patterns of unequilibrated non-porphyritic objects. The primary elemental abundances of the objects are those of a high-temperature condensate, therefore the pattern is flat with deficits in the moderately volatile and volatile elements (Fig. 13a). This condensate would have been a liquid. The liquid was supercooled, quenched, and solidified. Certain abundance anomalies, such as negative abundance anomalies of Zr, Nb, Ti, etc., could be primarily present due to fractional removal of high-temperature Ca, Al-rich condensates. Because these abundance anomalies are variable they are not indicated on the sketch. Fig. 13b illustrates the effect of exchange, by all phases of the objects, of Mg for moderately volatile elements Cr and Mn (probably together with some V and Fe^{2+}) with the cooling vapor. As these elements are olivine and pyroxene compatible, they were taken up mainly by those major minerals. The equilibration with the chondritic reservoir was successful in many objects from all UOC objects. The moderately volatile elements Sr and Ba are both incompatible and would not have been successfully emplaced in the now mostly crystalline objects. The result is that these elements have depleted abundances in most objects as compared to the RLE.

The volatile elements are all incompatible in olivine and pyroxene, and were exchanged (mainly for Ca) by the glasses and matrices with variable efficiency (Fig. 13c). Some few objects managed to fully equilibrate their moderately volatile and volatile element abundances with the chondritic reservoir, as illustrated in Fig. 13d.

7. Condensation calculations

For modeling the condensation of major rock forming elements more recent condensation studies (Yoneda and Grossman, 1995; Ebel and Grossman, 2000) consider various possi-

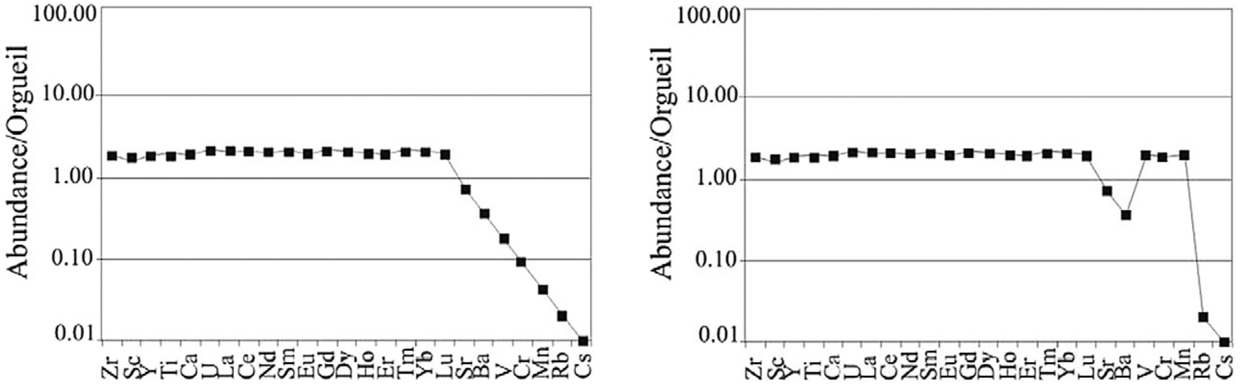

1. Condensation and vapor fractionation (deficit of volatile elements)

2. Metasomatic addition of moderately volatile elements V, Cr, mn (re-equilibration with the chondritic reservoir)

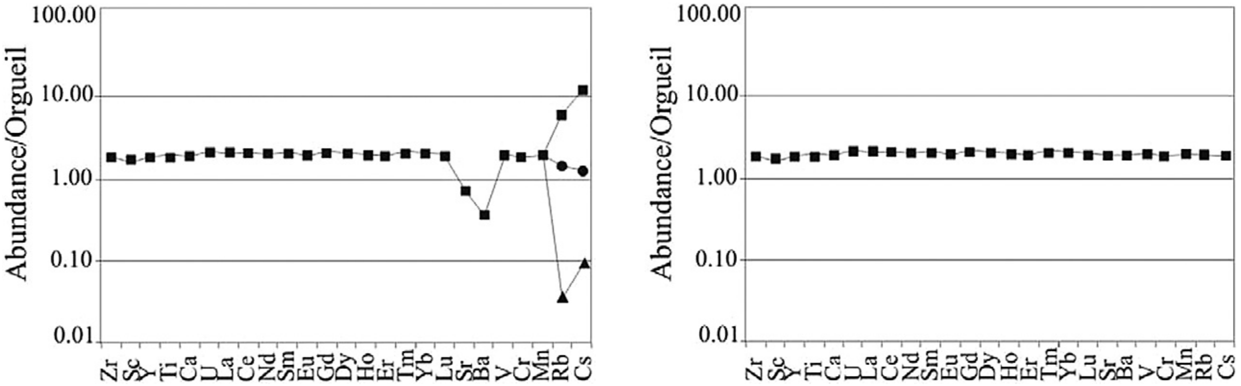

3. Addition of volatile elements during metasomatic processes (with variable efficiency)

4. Re-equilibration of moderately volatile and volatile elements with the chondritic reservoir

Fig. 13. Possible evolutionary history of the trace element patterns in chondrules, aggregates and other objects of unequilibrated chondrites.

ble nebular conditions, like different dust/gas ratios, possibilities which were excluded in former calculations. Accordingly, they show that silicate liquids and FeO-bearing silicates can be thermodynamically stable in dust-enriched systems at $10^{-6} < p_{\text{tot}} < 10^{-3}$ bar, and that silicate liquids can be in equilibrium with forsterite. Dust enrichment increases oxygen fugacity, the partial pressure of condensable species, as well as condensation temperatures, to temperatures at which partial melts are stable (Ebel and Grossman, 2000; Ebel, 2005). Thus, regions with enhanced condensable element/H ratios (e.g., dust-enriched regions) with increased partial pressure of condensable species can be considered as regions in the solar nebula where formation of chondrules as condensates from vapor is possible.

The shapes, textures as well as the smooth surfaces of non-porphyritic chondrules (like radiating pyroxene chondrules, fine-grained pyroxene chondrules, etc.) indicate that they may represent quenched liquids. As the majority of the unequilibrated objects studied are pyroxene-dominated non-porphyritic objects and have fractionated SiO_2 and MgO contents compared to the solar abundances, coupled with mostly unfractionated REE trace element abundance patterns, it was important to test if it is thermodynamically possible that non-porphyritic pyroxene-rich chondrules represent quenched liquid droplets formed by equilibrium condensation in the solar nebula. The calculations focused upon the question, under which conditions is pyroxene the sole stable liquidus phase? These conditions would allow the formation of non-porphyritic pyroxene chondrules as liquid condensates in the solar nebula. Therefore we have performed full equilibrium calculations of the sequence of condensation of the elements from cosmic gases in dust-enriched systems, but with a fraction of Mg removed as forsteritic olivine (Mg_2SiO_4).

In a system with solar bulk composition as well as systems enriched with dust of CI composition (the Mg/Si ratio of those systems is 1.074), olivine would be the stable liquidus phase before orthopyroxene in all cases, independent of the dust enrichment factor and the temperature. Fig. 14a shows that the stability field of orthopyroxene lies at lower temperature than the stability field of olivine in those systems. Therefore, if some chondrule types were formed as liquid condensates in a nebula with solar element ratios, in all cases—independent of the dust enrichment factor—olivine-rich chondrules with flat REE-patterns would be generated first. One possibility for changing the stability fields is to fractionate Mg from Si in these systems, and to simulate a fractional condensation. This scenario has already been explored for the mechanism of isolation of minerals during condensation (Petaev and Wood, 1998). Magnesium could be extracted in the form of forsterite at high temperatures, and subsequent fractional condensation at lower temperatures would result in different stability fields for the liquidus phases of the system. Thus we tested whether it is theoretically possible to form pyroxene chondrules through fractional condensation in the solar nebula for systems with different dust enrichment and how much forsterite must be extracted from the

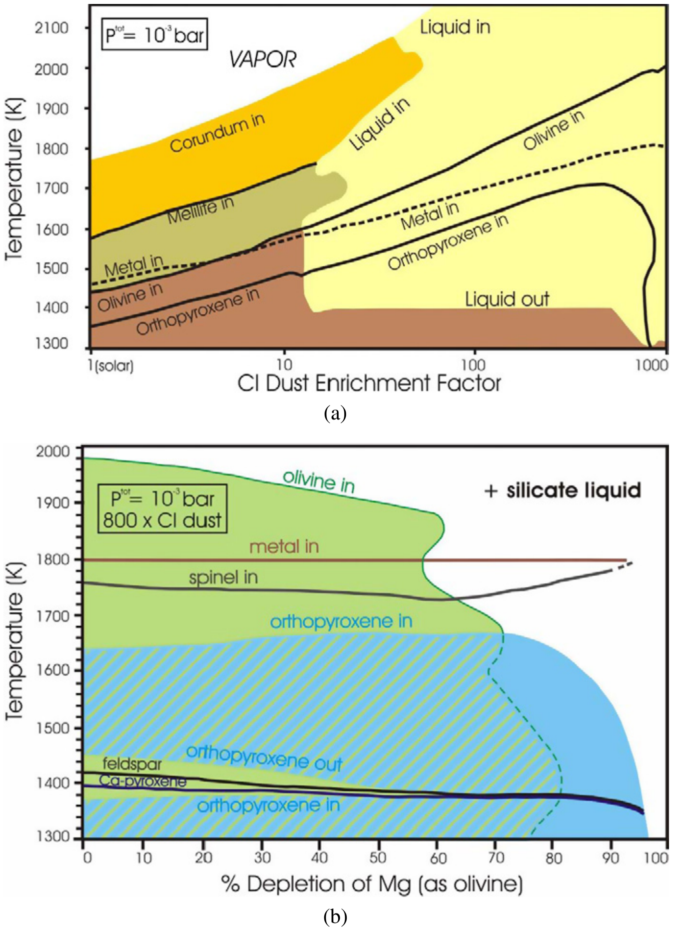

Fig. 14. (a) Stability fields of liquid, olivine and orthopyroxene in solar nebula gas with different dust enrichment factors [slightly modified after Ebel et al. (2003)]. (b) Stability fields of olivine and pyroxene in 800× dust-enriched solar nebula gas with different percentage of Mg depletion as forsterite [slightly modified after Ebel et al. (2003)].

system to get enstatite as a stable liquidus phase. This process would fractionate the Mg/Si ratio, but as the REE are hosted mostly by the glass (former silicate liquid) and pyroxene it would not change the REE contents significantly (the relative abundances of RLE should not change and stay chondritic), and the resulting chondrules would be fine-grained pyroxene chondrules with unfractionated REE abundances.

Ebel and Grossman (2000; cf. Ebel, 2005) created an algorithm that has been implemented in a computer code for the calculation of condensation sequences in cosmic nebular gases with high dust-enrichment. This code named "VAPORS" contains data for 23 elements (H, He, C, N, O, F, Ne, Na, Mg, Al, Si, P, S, Cl, Ar, K, Ca, Ti, Cr, Mn, Fe, Co, and Ni) distributed among 374 gas species and a variety of potential condensates, which are considered in every calculation run. The gas species include all species listed in Ebel and Grossman (2000), Yoneda and Grossman (1995), and Grossman (1972). Thermodynamic data for elements and gas species are from the JANAF database (Chase et al., 1985) corrected for errors (Ebel and Grossman, 2000; Lodders, 2004), Knacke et al. (1991), and Pedley and Marshall (1983). For potential solid condensates and for most end-member components of the solid solution series thermodynamic data were taken from Berman (1983, 1988) and Berman and Brown (1985).

For silicate liquids two different models are used: First, the CMAS liquid model (Berman, 1983) for refractory systems rich in CaO–MgO–Al_2O_3–SiO_2, and second the MELTS liquid model for systems with the components SiO_2–TiO_2–Al_2O_3–Fe_2O_3–Fe_2SiO_4–Mg_2SiO_4–$MgCr_2O_4$–$CaSiO_3$–Na_2SiO_3–$KAlSiO_4$–$Ca_3(PO_4)_2$–H_2O (Ghiorso and Sack, 1995; Berman, 1988). At high temperatures, the silicate liquids in dust-enriched systems are rich in CaO and Al_2O_3 (CMAS-liquid model is used) but with decreasing temperature liquid contents of SiO_2 and MgO increase. At the temperature where olivine (or pyroxene) becomes stable, the CMAS liquid and the MELTS liquid have nearly identical compositions (Ebel, 2005). Therefore, at the temperature of olivine (or pyroxene) stability, the switch is made from the CMAS liquid model to the MELTS silicate liquid model in the calculation.

7.1. Condensation calculation results

Minor Ca-, Al-rich refractory phases have been omitted from Fig. 14b. Silicates, metal and spinel crystallize from liquid at high temperatures, as elements continue to condense into the liquid from the vapor phase (Ebel et al., 2003). We found a very narrow range of conditions in which pyroxene is a stable liquidus phase at a higher temperature than olivine (Fig. 14b). It is theoretically possible to form pyroxene-rich chondrules through extreme fractional condensation at a p_{tot} of 10^{-3} bar in a system with a gas enriched 800× in CI dust. The resulting stability fields of silicates are shown in Fig. 14b (Ebel et al., 2003). The stability fields of olivine and orthopyroxene are plotted against temperature as functions of the percentage of Mg depletion (forsterite extraction). Over the whole range of olivine depletion, stable silicate liquids coexist with the mineral phases at high temperatures in this dust-enriched system up to about 75% olivine depletion, olivine is the liquidus phase, with its temperature of appearance decreasing from about 1980 K in the undepleted system to 1900 K at 60% olivine depletion. Enstatite appears as a stable liquidus phase at much lower temperatures (at about 1640–1680 K) over this range of olivine depletions. Spinel persists up to high percentages of Mg-extraction. In Fig. 14b the hatched area marks the broad temperature and composition range where olivine together with orthopyroxene appears as a stable phase coexisting with liquid above ∼1400 K. At about 1400 K (in the undepleted system, with somewhat lower temperatures in depleted systems) liquids crystallize entirely mainly into pyroxenes and feldspar. When about 72% of Mg is removed (as forsterite) from the system, olivine ceases to be stable, and orthopyroxene becomes the stable Mg-silicate, appearing at ∼1680 K. With increasing Mg depletion, the orthopyroxene stability field shrinks to lower temperatures, and above about 96% Mg depletion the orthopyroxene stability field disappears, as it must in the absence of Mg. We also investigated systems 200 and 500× in CI dust. In those systems, enstatite exists as a stable liquidus phase only at temperatures below that of olivine stability.

Our condensation calculation reveals a narrow range of possible conditions in which pyroxene-rich objects could condense directly from vapor. It is possible to get enstatite as the stable high-temperature liquidus phase (before olivine) in systems highly enriched in pre-condensed CI dust ($>500\times$), at a p_{tot} of 10^{-3} atm, and then only if between 72% and 95% of the Mg is removed from the system as forsterite.

In summary, the generation of pyroxene-rich non-porphyritic objects as liquid condensates is theoretically possible, but only within this fractionation mode under very special conditions. We have varied only two parameters (CI dust enrichment, and Mg fractionation), while holding total pressure, and dust type, constant. A great variety of parameters could be varied to explore other conditions for pyroxene stability (e.g., Ebel and Alexander, 2005). The model shows that all pyroxene-dominated non-porphyritic objects would have to be formed in locally Ol-depleted environments within a narrow range of possible bulk compositions. For our calculations only Mg-depletion by olivine removal was considered. However, there exist several cosmochemical ways to remove Mg from the system in a more effective way, such as by separating Mg under reducing conditions. Such a process very likely was active in the enstatite chondrite formation regions and these meteorites are very rich in pyroxene-rich and SiO_2-oversaturated chondrules, an indication of a highly fractionated Mg/Si ratio. Considering the emerging view that the protoplanetary disk was complex, inhomogeneous and dynamic, chondrule formation models that require extreme conditions should not be excluded from investigation. Simple equilibrium condensation of a vapor of solar composition (e.g., Grossman, 1972; Lodders, 2003) is not sufficient to address chemical processes in the overall nebula. Scenarios combining dust enrichment (Wood, 1967; Ebel and Grossman, 2000) and fractional condensation (e.g., Larimer, 1967; Petaev and Wood, 1998) seem to be required. The high concentration of grossite in certain CAIs as well as the existence of silica-rich objects in CH chondrites points towards an effective isolation of condensates from nebular gases during condensation, which would result in a fractionated residual nebular gas (Petaev and Krot, 1999). Also, the possibility that during condensation a specified fraction of condensates was withdrawn from the gas in particular disk regions as a consequence of growth and aggregation of condensed mineral grains, introduces important potential effects on the sequence of minerals in equilibrium with the gas (Petaev and Wood, 1998). A difficulty with such fractional condensation scenarios is that different fractionation factors can, or must, be invoked to explain every unique object. Here, however, a large class of objects is being considered to possibly result from a single kind and degree of major element fractionation. The formation of aggregates and chondrules of early condensates (e.g., Varela et al., 2005) may deplete the gas enough to enable the condensation of pyroxene-rich liquids which can be quenched to produce cryptocrystalline and/or radiating pyroxene chondrules.

As these fine-grained objects are omnipresent in all chondrite classes, such formation conditions must have been available throughout the solar nebula and represent normal rather than special conditions.

7.2. Did non-porphyritic pyroxene and barred-olivine chondrules share the same formation region in the nebula?

Our recent studies of BO chondrules from LL3.1, CM2, CH3, and C3-UNGR chondrites revealed that they possibly represent primary liquid condensates of the solar nebula (Varela et al., 2006). Their bulk major and trace element composition is compatible with that theoretically predicted for early solar nebula liquid condensates. Thus, according to our calculations and based on earlier results (Ebel and Grossman, 2000; Alexander, 2004; Ebel, 2005), for a temperature of 1700 °C and a pressure of 10^{-3} atm, the primary condensate liquid from which BO chondrules could form will condense in regions of the solar nebula with a dust enrichment of $\sim 700P\times$. This dust (minimum) enrichment factor is surprisingly similar to that reported here for enstatite stability as liquidus phase. If BO and non-porphyritic pyroxene chondrules can have an origin by direct liquid condensation in extremely dust-enriched systems, it is possible that both could have been generated in the same nebular region. Spinel is also a stable phase (Fig. 14) and is frequently observed associated with the glass in the primary glass inclusions hosted by the barred olivine crystals. Thus both objects could share the same formation process: The primary liquid condensation process (Varela et al., 2005). Because liquids can nucleate from a vapor much more easily than can crystals, the PLC model proposes that the first condensate to appear in the solar nebula is likely to be a liquid. Liquids generated in this way will have a chemical composition that is governed by gas–liquid equilibria.

Both types of chondrules can part the same nebular region, if formation of BO chondrules promotes removal of sufficient Mg as forsterite, and creates the olivine-depleted conditions necessary for the stability of low-Ca pyroxene-rich liquids. These objects can, therefore, represent samples of a very early (the BO chondrules) and of a late (the non-porphyritic pyroxene chondrules) liquid condensation of major elements in a single, dust-enriched solar nebular region.

8. Conclusions

The petrographic observations of chondrites show that each individual building block, each type of object, reflects a very complex and possibly unique evolution history. Textures clearly indicate that many objects once must have been liquids which were quenched, which is the base for all major chondrule models. Both chondrule formation mechanisms discussed above can produce SiO_2-rich compositions, either by sampling and melting of appropriate mineral precursors, or by fractional condensation. However, if pyroxene-dominated non-porphyritic chondrules were produced by sampling and melting of precursors, we should expect some fractionation of REE abundance pattern, as well as fractionated CaO/Al_2O_3, Yb/Ce, and Sc/Yb ratios according to the mineralogy of the objects. The fact that we do not see these fractionations in the majority of the unequilibrated chondrite objects—in spite of the fractionation of SiO_2 relative to MgO—makes this genetic model difficult to apply. These chemical features rather support an origin by direct condensation as do the abundant signs of vapor fractionation, in particular the negative abundance anomalies of medium volatile elements Sr and Ba, common features in objects of all chondrites. The common abundance anomalies of Eu, U, and Ca could be due to the fractionation of one or more unidentified mineral phases. This fractionation could be achieved applying both genetic models. The only constraint they provide is that the phase which caused the fractionated abundances of these elements did not fractionate the REE patterns of the residual vapor. For this reason, also in this case subsolidus vapor-related processes are likely to have been active. However, only for Ca the case is clear-cut as it is obvious that loss of Ca was compensated by gain of Na (and other alkali elements). Europium either followed the medium volatile elements Si and Ba or was mobilized after solidification of the objects and found a site in the fine-grained dust of the local nebula. Enrichments in Eu are indeed common in matrices of chondrites; see the "holy smoke" of Rambaldi et al. (1981). Uranium preferentially stays in chondrules and chondrules-like constituents.

Our condensation calculations show that it is theoretically possible that pyroxene-dominated chondrules with flat REE patterns can be produced as liquid condensates. Because pyroxene-dominated chondrules need dust-enriched regions with similar dust/gas ratios (>500 × Cl) to those needed to form BO chondrules (700 × Cl) also as liquid condensates, both objects could shared a related origin in the same nebular region as they usually share the same chondrite. Formation of BO chondrules as early liquid condensate (Varela et al., 2006) and formation of porphyritic aggregates and chondrules by liquid-supported condensation of olivine from the nebula will increase the Si/Mg ratio of the system. Indeed, a majority of BO chondrules are mantled by olivine, with an outer pyroxene rind, which could isolate these objects from further chemical reaction. This fractionation process could create conditions for the formation of non-porphyritic, pyroxene-dominated chondrules by condensation.

Continuing communication of the pyroxene-rich objects with the cooling nebula would promote a variety of elemental exchanges between the chondrule and the nebula gas. In this way, moderately volatile elements as well as volatile elements could have been added to the objects by metasomatic processes (equilibration with the chondritic reservoir; e.g., Cr, Mn, FeO as well as K and Na in exchange for Mg and Ca). The olivine- and pyroxene-compatible elements apparently readily entered the non-porphyritic pyroxene-dominated chondrules and were easily accommodated with the result that in many chondrules these elements are present in slightly super-chondritic amounts and unfractionated relative abundances.

Acknowledgments

Financial support was received from FWF (P13975.GEO and P14938), Austria, from CONICET (PIP 5005) and SECYT (P 07-08176), Argentina. We appreciate the reviews by A. Rubin and A. Davis, that have contributed to improve this manuscript, and the handling of the paper by the associated editor A. Ingersoll.

Appendix A
Petrography of Bishunpur (LL3.1) objects

Object	Shape	Diameter	Texture	Ax. grain size	Surface features	Mineralogy	Annotations
BP1	IO irregular	160 µm	GP (granular)	5–10 µm	Irregular surface	Ow-Ca px, glass, M, S	
BP2	U strongly irregular	800 µm	GOP-POP (granular-porphyritic)	20 µm	Irregular surface M, S mantle	Ol, low-Ca px, glass M, S	Contains coarse M, S grains; some big voids
BP3	IO irregular	400 µm	RPO (fibrous-granular)	<10 µm	Irregular surface	Low-Ca px, ol, glass M, S	Distribution of px and ol plates is inhomogeneous
BP4	CF rounded	300 µm	RP (platy px)	10 µm	Irregular surface fine-grained silicate mantle	Low-Ca px, glass M, S	Various large voids and cracks
BP5	IO irregular	180 µm	GP (granular-cryptocrystalline)	1 µm	Irregular surface	Low-Ca px, glass	Various large cracks
BP6	C spherical	1.1 mm	RP (fibrous-excentric-radiating)	<10 µm	Fine-grained silicate mantle M, S grains attached	Low-Ca px, glass, M, S	Various large cracks; porous parts
BP7	IO irregular	300 µm	RPO (fibrous)	<5 µm	Irregular surface	Ol, low-Ca px, glass, M, S	No ol in outermost parts various large cracks
BP8	IO irregular	400 µm	GP (fibrous-granular)	1 µm	Irregular surface	Low-Ca px, glass, M, S	Homogeneous structure: mantle and local parts contain glass, others voids instead

Abbreviations: C: chondrule, GP: granular pyroxene, M: metal, ol: olivine, CF: chondrule fragment, GOP: granular olivine–pyroxene, S: sulfide, px: pyroxene, IO: irregular object, POP: porphyritic olivine–pyroxene.

(*continued on next page*)

Appendix A (*continued*)
Petrography of Krymka (LL3.1) objects

Object	Shape	Diameter	Texture	Ax. grain size	Surface features	Mineralogy	Annotations
KR1	C spherical	550 μm	RP-GP (fibrous)	<5 μm	Outhermost part porous locally altered, round depression (∼100 μm)	Low-Ca px, glass, M, S, high-Ca px	High-Ca px occurs subordinate, forms rims on low-Ca px
KR2	IO rounded	800 μm	GP (granular)	10 μm, 60 μm	Irregular surface with coarse M/S grains	Low-Ca px, high-Ca px glass, SiO2, M, S	SiO2 is approx. regularly distributed inside the object: few px crystals up to 60 μm
KR3	CF rounded	2.3 mm	GP-RP (crypto-crystalline)	1 μm	Porous mantle, which originated after chondrule breakup	Low-Ca px, ol, glass	Many cracks
KR5	CF partly rounded	400 μm	RP (platy: coarse px plates)	30 μm	Irregular surface	Low-Ca px, high-Ca px, glass	Alteration along cracks
KR6	U irregular	1.4 mm	RP-GP? (platy px)	70–80 μm	Irregular surface	Low-Ca px, high-Ca px glass, M, S	High-Ca px forms rims on low-Ca px
KR7	CF sperical	1 mm	RP (platy px)	<10 μm	Porous mantle, round depression (∼200 μm)	Low-Ca px high Ca-Px glass, M, S	High-Ca px forms rims on low-Ca px
KR12	IO partly rounded	700 μm	BO (platy, dendritic)	<10 μm	Irregular surface	Ol, glass	Ol and glass donot show sharp grain boundaries
KR14	IO irregular	250 μm	BO (platy olivine)	20 μm	Highly irregular surface	Ol, glass	Object boundary is difficult to define

Abbreviations: C: chondrule, RP: radiating pyroxene, M: metal, CF: chondrule fragment, BO: barred olivine, S: sulfide, IO: irregular object, GP: granular pyroxene, px: pyroxene, U: unclassified object, ol: olivine.

Petrography of Mezo-Madaras (L3.7) objects

Object	Shape	Diameter	Texture	Ax. grain size	Surface features	Mineralogy	Annotations
MM2	C spherical	1.5 mm	GP (fibrous-granular)	10 μm	Round depression (500 μm)	Low-Ca px, glass, M, S	
MM4	CF rounded	600 μm	GPO (granular)	5 μm	Irregular surface	Low-Ca px, glass, ol	Ol in the rim areas only: Fe-enrichment commencing from the rim?
MM5	IO irregular	250 μm	GP (granular)	10 μm	Irregular surface	Low-Ca px, glass high Ca-px	High-Ca px occurs only as small crystals at the rims of low-Ca px
MM6	IO partly rounded	500 μm	GP (granular-platy)	10 μm	Irregular surface with coarse-grained M, S attached	Low-Ca px, glass ol, high-Ca px	High-Ca px occurs only as small crystals at the rims of low-Ca px
MM7	IO partly rounded	700 μm	GP (platy-granular)	40 μm	Irregular surface with coarse-grained M, S attached	Low-Ca px high-Ca px, glass, M, S	High-Ca px occurs as rims on low-Ca px; coarse-grained object
MM10	C spherical-ellipsoidal	400 μm	RPO-GPO (fibrous-granular)	<10 μm	Irregular surface outermost parts without ol	Low-Ca px, ol	No ol in the rim; various voids inside object
MM11	C ellipsoidal	1 mm	RPO GP+BO? (platy combined with granular)	<10 μm	Ol rim, irregular surface round depression (∼100 μm)	Low-Ca px ol, glass, M, S	Partly barred olivine (thin ol plates with glass) partly coarse-grained low-Ca px
MM12	U irregular	300 μm	GP (granular)	<10 μm	Highly irregular surface; fine-grained mantle (silicate phases)	Low-Ca px, ol glass, M, S chromite	Opx is inhomogeneous; ol: secondary phase?
MM13	CF partly rounded	350 μm	GP-RP (platy-granular)	10 μm	Thick ol-mantle (with subodinated opx)	Low-Ca px, Ca-px, glass, SiO2	Ca-px occurs along cracks and rims low-Ca px
MM15	C spherical	300 μm	GP (fibrous-granular)	2–3 μm	Irregular surface; the outermost part is locally altered	Low-Ca px, glass, M, S	Metasomatic Fe-enrichment in outermost parts
MM17	CF partly rounded	500 μm	RPO (fibrous-granular)	2–3 μm	Regular surface; outermos ol, part without ol; thin or thick mantle of ol, px and glass attached	Low-Ca px, M, S	Bordered by large M, S grains

Appendix A (*continued*)

Object	Shape	Diameter	Texture	Ax. grain size	Surface features	Mineralogy	Annotations
MM19	C spherical	500 μm	BO (platy-ol)	30 μm	Irregular surface	Ol, glass, Ca-px, M, S	Ol crystals seem to be zoned (or due to section preparation?)
MM21	IO partly rounded	400 μm	RPO (fibrous-granular)	2–3 μm	Regular surface, outermos parts without ol but with a chromite zone; thin to thick ol mantle attached	Low-Ca px, ol, M, S, cr	Various voids (a lost mineral phase?)
MM22	IO irregular	200 μm	RO (fibrous)	3–4 μm	Irregular surface with thin ol mantle, few px	Ol, glass, M, S	

Abbreviations: C: chondrule, IO: irregular object.

Petrography of Tieschitz (H/L 3.6) objects

Object	Shape	Diameter	Texture	Ax. grain size	Surface features	Mineralogy	Annotations
TS10	C spherical-ellipsoidal	200 μm	ROP (fibrous-granular)	<10 μm	Irregular surface fine-grained silicate mantle as well as M/S grains attached	Ca-px, ol, glass, M/S	Parts with glass and parts without glass (voids instead) local voids filled with M/S outermost part is porous
TS14	CF partly rounded	800 μm	GP-RP (fibrous-granular)	<10 μm	Fine-grained silicate mantle round depression (∼150 μm)	Low-Ca px, glass, M/S	(Zone originated after chondrule breakup) M/S along cracks (center)
TS19	C ellipsoidal-spherical	400 μm	GPO-BOP (platy-granular)	20 μm	Irregular surface fine-grained silicate mantle	Low-Ca px, ol Ca-px, mes, cr	Ol-zoning (Fe-rich rims) mesostasis with coarse-grained crystals
TS20	U irregular	500 μm	GP (platy-granular)	10 μm	Strongly irregular surface fine-grained mantle (silicates and M/S)	Low-Ca px	Various voids
TS24	U irregular	400 μm	C-GP (fibrous-dendritic)	1 μm	Irregular surface	Low-Ca px, glass, M/S	Large cracks lost mineral phase?
TS26	IO partly rounded	800 μm	GP-RP (fibrous)	1 μm	Irregular surface fine-grained silicate mantle as well as M/S grains attached	Low-Ca px, glass M/S	Big voids and various cracks lost mineral phase?
TS27	IO partly rounded	700 μm	GP (platy-granular)	5–50 μm	Irregular surface fine-grained silicate mantle subordinat M, S	Low-Ca px	Various voids highly variable grain sizes; secondary altered zone (local Fe enrichment)
TS28	IO irregular	600 μm	GPO (fibrous-crypto-crystalline)	1 μm	Irregular surface fine-grained silicate mantle	Low-Ca px, ol, glass	Outermost part is porous and Fe-rich
TS32	U irregular	850 μm	GPO BO + GP (fibrous-granular)	10–50 μm	Irregular surface fine-grained silicate mantle	Low-Ca px, glass, M,	Partly barred olivine (fine ol plates and glass) partly coarse-grained low-Ca px
TS37	CF partly rounded	400 μm	CP-GP (crypto-crystalline)	<1 μm	Fine-grained silicate mantle	Low-Ca px, glass, M, S	Outermost part is Fe enriched
TS44	U irregular	600 μm	GP (platy-granular)	<10 μm	Irregular surface fine-grained silicate mantle	Low-Ca px, M, S	Various voids; local Fe enrichment
TS47	C rounded	800 μm	PP (granular-porphyritic)	>10 μm	Irregular surface fine-grained silicate mantle	Low-Ca px, high-Ca px glass, M, S	Altered zone with coarse-grained M, S and granular texture

Abbreviations: C: chondrule, IO: irregular object.

Petrography of Sahara 97210 (L/LL3.6) objects

Object	Shape	Diameter	Texture	Ax. grain size	Surface features	Mineralogy	Annotations
SO1	IO irregular	430 μm	BO (fine platy ol)	3–4 μm	Irregular surface; local ol-(gl) mantle	Ol, glass	Ol plates are very fine
SO2	IO irregular	600 μm	GPO (granular)	<10 μm	Irregular surface fine-grained silicate mantle	Low-Ca px, glass, ol	Ol secondary (alteration?)
SO3	CF partly rounded	1 mm	GP-RP (fibrous)	10 μm	Irregular surface local coarse M, S attached	Low-Ca px, glass, ol, M, S	Zoned px: core is richer in Mg than rim; local secondary ol in outermost parts

(*continued on next page*)

Appendix A (*continued*)
Petrography of Sahara 97210 (L/LL3.6) objects

Object	Shape	Diameter	Texture	Ax. grain size	Surface features	Mineralogy	Annotations
SO4	IO irregular	850 µm	BO (platy ol)	<10 µm	Irregular surface, ol mantle local coarse-grained M, S attached	Ol, glass, M, S	
SO5	U partly rounded	300 µm	GPO (platy-fibrous)	<10 µm	Irregular surface with ol mantle	Low-Ca px, high-Ca px, ol	Opx is inhomogeneous: secondary Fe-enrichment ol secondary?
SO6	IO irregular	700 µm	BO + GP (platy and granular)	ol <10 µm, px 50 µm	Irregular surface with ol mantle	Ol, low-Ca px glass, M, S	Partly barred olivine (thin ol plates with glass) partly coarse-grained low-Ca px
SO7	CF ellipsoidal	1.7 mm	GP (granular-fibrous)	20 µm	Irregular surface, local coarse M, S attached	Low-Ca px, high-Ca px glass, SiO2, M, S	Inhomogenous px (low-Ca core, high-Ca rim)
SO8	CF partly ellipsoidal	6.5 mm	GPO (granular-fibrous)	20 µm	Irregular surface	Low-Ca px, high-Ca px mes, ol, M, S	Inhomogenous px (low-Ca core, high-Ca rim)
SO9	CF ellipsoidal	1.5 mm	RP-GPO (platy combined with granular)	<100 µm	Irregular surface	Low-Ca px, high-Ca px ol, mes, M, S	Zoned Px (high-Ca rim); px and ol have different textures
SO10	CF partly rounded	900 µm	GPO (fine granular)	<1 µm	Irregular surface	Low-Ca px, ol, glass	Local Fe-enrichment
SO11	C ellipsoidal	950 µm	RPO-GPO (platy)	<30 µm	Irregular surface	Low-Ca px, ol, glass, M, S	Zoned px (high-Ca rim) local Fe-enrichment
SO12	C ellipsoidal-spherical	1.3 mm	BO (crypto-crystalline-platy-ol)	<5µm	Irregular surface with ol mantle	Ol, glass	Ol plates are very thin; local secondary Fe-enrichment
SO13	IO irregular	2.1 mm	GPO (granular)	20 µm	Irregular surface with ol mantle	Ol, low-Ca px, glass	Ol abundance decreases from center to surface Fe-enrichment?
SO14	IO irregular	700 µm	GPO (granular)	20 µm, ol 70 µm	Irregular surface	Px, ol, glass	Dx sometimes with Ca-rich rims and Fe-enrichment

Abbreviations: C: chondrule, IO: irregular object.

Appendix B
Representative analysis of mineral phases in the UOC: BISHUNPUR

Object	BP1_2	BP2_7	BP2_22	BP3_7	BP3_11	BP3_px	BP4_px	BP6_px	BP7_px	BP8_10	BP8_12r
Pyroxene											
SIO2	55.6	59.5	55.5	56.4	53.8	55.0	57.3	54.5	54.6	55.3	54.8
TIO2	b.d.	0.3	b.d.	0.1	0.3	0.10	0.04	0.02	0.08	0.4	b.d.
AL2O3	0.5	2.1	0.4	1.9	0.9	1.47	0.44	0.08	1.26	b.d.	0.1
CR2O3	0.3	1.1	0.8	0.7	1.1	0.81	0.77	0.74	0.89	0.4	1.1
FEO	15.8	3.6	3.9	7.6	8.4	8.4	8.5	18.6	15.5	17.6	18.6
MNO	0.8	0.7	1.0	0.2	0.7	0.45	0.74	0.75	0.74	0.4	0.3
MGO	25.0	28.8	36.1	30.9	33.9	33.2	32.0	24.3	26.3	24.0	23.4
CAO	0.6	2.4	2.2	1.9	0.9	1.14	0.44	0.64	1.39	1.3	1.3
NA2O	0.2	0.4	0.3	b.d.	b.d.	0.08	0.01	0.07	0.07	0.2	0.3
K2O	0.1	0.1	b.d.	b.d.	b.d.	b.d.	b.d.	b.d.	b.d.	b.d.	b.d.
TOTAL	98.8	99.0	100.0	99.9	99.9	100.7	100.2	99.7	100.8	99.6	99.9
WO	1.20	5.21	3.83	3.76	1.69	2.10	0.84	1.29	2.75	2.71	2.74
EN	72.04	87.49	89.43	84.31	85.51	85.14	85.39	68.20	72.24	68.54	67.02
FS	26.76	7.30	6.74	11.93	12.80	12.77	13.77	30.51	25.01	28.76	30.24
JD	1.41	3.06	0.00	0.00	0.00	0.00	0.07	0.51	0.50	0.00	2.19
AE	0.00	0.00	0.02	0.00	0.00	0.01	0.00	0.00	0.00	0.02	0.00

Object	BP1_7	BP2_gl	BP6_11	BP6_gl	BP7_3	BP7_6	BP8_3
Glass							
SiO2	68.7	72.0	78.2	72.7	60.5	64.3	76.0
TiO2	0.3	0.55	b.d.	0.2	0.7	0.5	0.1

Appendix B (*continued*)

Object	BP1_7	BP2_gl	BP6_11	BP6_gl	BP7_3	BP7_6	BP8_3
AI2O3	11.1	19.2	9.1	6.5	19.1	19.2	7.8
Cr2O3	b.d.	0.17	b.d.	0.2	0.2	b.d.	0.3
FeO	6.3	1.46	2.6	8.2	3.6	4.1	5.1
MnO	0.3	0.06	b.d.	0.2	0.2	b.d.	b.d.
MgO	5.3	1.27	1.4	4.9	2.6	4.2	5.8
CaO	1.6	0.92	0.6	1.0	3.1	2.6	0.9
Na2O	3.5	1.30	5.6	2.3	7.8	4.1	1.9
K2O	0.4	0.94	1.0	0.8	0.6	0.6	0.7
P2O5	0.9	n.a.	0.6	n.a.	0.4	0.2	0.7
SO4	0.8	n.a.	b.d.	n.a.	0.3	b.d.	0.2
TOTAL	99.0	97.9	99.1	97.0	99.1	99.8	99.7

Abbreviations: n.a. = not analyzed; b.d. = below dedection limit r = rim.

Object	BP2_5	BP2_ol*	BP3_5r	BP3_14	BP3_15	BP6_20	BP7_2	BP7_9
Olivine								
SIO2	42.5	42.0	47.3	41.4	43.3	41.9	40.0	40.3
TIO2	b.d.	0.02	b.d.	b.d.	b.d.	0.1	b.d.	0.3
AL2O3	b.d.	b.d.	0.4	0.3	1.8	b.d.	0.1	0.5
CR2O3	0.3	0.23	1.2	0.6	0.7	0.9	0.3	0.3
FEO	6.8	6.6	10.1	13.2	13.1	33.7	24.5	23.9
MNO	0.1	0.50	0.4	b.d.	0.1	b.d.	1.0	0.7
MGO	50.1	51.2	39.2	43.0	39.2	22.4	33.2	32.2
TOTAL	99.8	100.5	98.5	98.5	98.1	99.0	99.0	98.1
XFA	0.07	0.07	0.13	0.15	0.16	0.46	0.29	0.29
XFO	0.93	0.93	0.87	0.85	0.84	0.54	0.71	0.71

Note. Na, Ca, K: below dedection limit.

Representative analysis of mineral phases in the UOC: KRYMKA

Object	KR2	Kr2_13	Kr2_25r	Kr3_14	KR5	KR5_2	KR6	KR6_2	KR7	Kr7_5
Pyroxene										
SIO2	57.9	56.9	54.5	52.4	58.7	51.6	56.5	52.7	57.6	55.1
TIO2	0.04	0.4	0.3	0.2	0.06	0.90	b.d.	0.06	0.02	0.2
AL2O3	0.36	1.0	1.9	1.9	0.65	6.4	0.13	0.45	0.26	2.2
CR2O3	0.87	1.3	1.8	0.8	0.52	1.38	0.51	1.19	0.85	1.3
FEO	6.1	7.5	7.2	18.9	3.8	6.6	12.7	21.8	8.5	9.1
MNO	0.69	1.3	2.6	0.6	0.17	0.73	0.39	0.93	0.74	1.3
MGO	33.5	29.9	22.9	22.8	35.7	15.7	29.8	21.0	32.0	20.3
CAO	0.53	1.1	8.1	1.5	0.44	15.7	0.16	1.84	0.43	9.7
NA2O	b.d.	0.2	0.1	0.2	0.09	2.17	b.d.	0.06	0.00	0.2
K2O	b.d.	0.1	0.2	0.1	0.06	0.36	b.d.	b.d.	0.01	0.2
TOTAL	100.0	99.7	99.5	99.3	100.1	101.6	100.1	100.0	100.4	99.5
WO	1.01	2.14	17.02	3.08	0.83	36.15	0.31	3.78	0.82	21.07
EN	88.85	83.90	66.78	65.53	93.41	50.55	80.00	59.86	85.36	61.33
FS	10.15	13.97	16.21	31.39	5.77	13.30	19.69	36.37	13.82	17.60
JD	0.07	1.37	0.83	1.77	0.61	15.36	0.07	0.00	0.00	1.17
AE	0.00	0.00	0.00	0.00	0.00	0.00	0.00	0.01	0.00	0.00

Abbreviations: c = core, r = rim; b.d. = below dedection limit.

Object	Krl_1	KR2_1	Kr2_9	Kr2_10	Kr2_15	Kr3_2	KR6	KR7	KR12	KR14
Glass										
SiO2	74.5	98.5	92.9	96.3	69.6	68.2	70.2	71.1	55.0	69.4
TiO2	0.4	0.05	0.3	0.2	0.6	0.1	0.52	0.50	0.98	0.39
AI2O3	8.9	0.64	3.5	1.5	16.9	4.3	16.6	17.3	20.1	9.4
Cr2O3	0.3	0.03	0.2	0.2	0.3	0.2	0.03	0.05	0.19	0.02
FeO	2.2	0.38	0.2	0.1	3.2	11.2	5.6	2.9	0.36	7.5
MnO	0.4	0.03	0.2	0.1	0.6	0.4	0.09	0.12	0.03	0.28
MgO	8.9	0.64	1.1	0.3	0.3	12.9	0.23	1.03	4.5	4.1
CaO	2.4	0.11	0.4	0.4	2.8	1.2	1.63	0.48	16.6	2.2
Na2O	0.1	0.19	0.3	0.1	4.4	0.4	1.76	5.4	2.9	3.5
K2O	1.1	b.d.	0.2	0.1	0.9	0.7	1.10	0.02	0.08	0.95

(*continued on next page*)

Appendix B (*continued*)

Object	Krl_1	KR2_1	Kr2_9	Kr2_10	Kr2_15	Kr3_2	KR6	KR7	KR12	KR14
P2O4	0.2	n.a.	0.3	0.2	b.d.	0.1	n.d.	n.a.	n.a.	n.a.
SO3	0.4	n.a.	0.4	0.3	b.d.	0.3	n.d.	n.a.	n.a.	n.a.
TOTAL	99.8	100.6	99.9	99.8	99.5	99.9	97.8	98.9	100.8	97.8

Abbreviations: n.a. = not analyzed; b.d. = below dedection limit.

Object	Krl2_6	KR12	Krl4_3r	Krl4_6r	Krl4_2c	Krl4_5c	KR14
Olivine							
SIO2	43.2	43.0	36.5	37.6	37.9	38.1	38.5
TIO2	0.4	0.14	0.5	0.2	0.2	0.2	b.d.
AL2O3	0.6	0.44	0.5	0.5	0.5	0.7	b.d.
CR2O3	0.4	0.20	0.4	0.2	0.4	0.5	0.21
FEO	0.7	0.55	26.5	24.2	21.1	21.7	20.3
MNO	0.2	0.09	1.1	0.9	0.9	0.7	0.61
MGO	53.4	54.4	33.0	35.3	37.6	36.9	40.4
TOTAL	98.8	98.9	98.4	98.8	98.6	98.7	100.0
XFA	0.01	0.01	0.31	0.28	0.24	0.25	0.22
XFO	0.99	0.99	0.69	0.72	0.76	0.75	0.78

Abbreviations: c = core, r = rim; b.d. = below dedection limit. Na, Ca, K: below dedection limit.

Representative analysis of mineral phases in the UOC: MEZÖ-MADARAS

Object	MM4	MM5_1	MM6	MM7	MM10	MM11	MM12	MM13	MM15	MM15_r	MM17	MM17_18	MM21
Pyroxene													
SIO2	56.0	57.8	58.0	54.3	54.9	55.1	53.6	59.1	57.7	55.4	53.9	56.2	55.2
TIO2	0.40	0.11	0.08	0.23	0.13	0.09	0.02	0.04	0.06	0.07	0.04	b.d.	b.d.
AL2O3	5.1	1.12	0.59	1.53	0.81	0.20	0.47	0.37	0.95	0.96	0.36	0.2	0.08
CR2O3	0.46	0.78	0.68	1.45	0.53	0.93	0.77	0.47	0.77	0.72	0.70	b.d.	0.39
FEO	1.30	3.9	3.6	7.1	13.0	11.6	18.0	2.6	9.2	9.4	14.1	14.8	17.2
MNO	0.19	0.17	0.37	1.15	0.40	0.77	0.60	0.07	0.83	1.09	0.32	b.d.	0.39
MGO	32.7	35.6	37.2	25.0	29.5	28.3	25.1	37.4	30.7	28.2	30.7	27.5	27.3
CAO	4.3	1.75	0.35	9.5	0.79	2.8	0.88	0.51	0.91	4.8	0.59	0.5	0.29
NA2O	0.42	0.26	0.10	0.40	0.03	0.12	0.23	0.10	0.15	0.21	0.03	0.5	0.03
K2O	0.07	0.05	b.d.	0.03	b.d.	b.d.	b.d.	b.d.	0.10	0.03	b.d.	b.d.	b.d.
TOTAL	100.9	101.5	100.9	100.7	100.1	99.9	99.8	100.6	101.3	100.9	100.8	99.8	100.9
WO	8.46	3.22	0.64	18.72	1.51	5.38	1.75	0.93	1.77	9.21	1.08	0.91	0.56
EN	89.25	90.97	93.78	68.59	78.45	76.04	69.39	95.31	83.07	75.09	78.23	76.09	72.99
FS	2.29	5.81	5.58	12.69	20.04	18.58	28.87	3.76	15.16	15.71	20.69	23.00	26.46
JD	2.90	0.00	0.00	0.00	0.00	0.00	0.00	0.66	1.04	0.00	0.00	3.74	0.00
AE	0.00	0.02	0.01	0.03	0.00	0.01	0.02	0.00	0.00	0.02	0.00	0.00	0.00

Object	MM2_11	MM6_14	MM6	MM7	MM11	MM13_1	MM19
Glass							
SiO2	76.0	64.0	63.6	68.8	71.6	95.7	61.1
TiO2	0.3	0.3	0.55	0.18	0.44	b.d.	0.96
Al2O3	11.9	16.9	23.6	20.0	14.7	0.1	19.1
Cr2O3	0.3	0.1	0.04	0.17	0.08	b.d.	0.47
FeO	0.6	2.3	1.51	1.45	1.21	2.0	3.6
MnO	0.3	b.d.	0.06	0.08	0.04	0.4	0.09
MgO	2.5	3.6	2.5	2.65	1.11	1.0	6.2
CaO	1.7	3.1	1.34	0.89	0.91	0.4	4.9
Na2O	5.4	8.4	6.1	4.6	2.8	0.1	3.2
K2O	0.5	0.2	0.06	0.61	3.5	b.d.	0.19
P2O5	b.d.	0.3	n.a.	n.a.	n.a.	0.3	n.a.
SO3	0.4	0.2	n.a.	n.a.	n.a.	b.d.	n.a.
TOTAL	99.8	99.5	99.3	99.4	96.4	100.0	99.8

Abbreviations: n.a. = not analyzed; b.d. = below dedection limit.

Object	MM2_r	MM6_4	MM7_16	MM13_r	MM15_29	MM17_o	MM17_r
Olivine							
SIO2	38.5	44.9	39.0	36.7	39.0	48.2	36.9

Appendix B (*continued*)

Object	MM2_r	MM6_4	MM7_16	MM13_r	MM15_29	MM17_o	MM17_r
TIO2	b.d.	b.d.	0.2	b.d.	0.2	0.1	b.d.
AL2O3	1.5	0.1	b.d.	0.21	b.d.	0.3	0.03
CR2O3	0.6	0.1	0.1	0.04	b.d.	0.3	0.05
FEO	23.6	8.1	21.3	31.0	23.9	20.1	29.0
MNO	0.9	b.d.	0.6	0.55	0.4	0.4	0.50
MGO	33.8	45.8	38.1	31.2	36.0	31.2	33.3
TOTAL	98.8	99.0	99.3	99.7	99.4	100.4	99.8
XFA	0.28	0.09	0.24	0.36	0.27	0.27	0.33
XFO	0.72	0.91	0.76	0.64	0.73	0.73	0.67

Representative analysis of mineral phases in the UOC: TIESCHITZ

Object	TS14_c	TS14_r	TS19	TS20	TS24	TS26	TS27	TS28	TS32	TS44	TS47_6r
Pyroxene											
SIO2	55.1	55.1	54.7	56.7	53.9	52.9	58.4	53.3	56.0	55.5	52.1
TIO2	0.07	0.04	0.14	b.d.	0.05	0.07	0.15	0.1	0.06	0.06	0.9
AL2O3	0.46	0.50	1.05	0.12	0.85	0.93	1.77	1.1	0.32	0.31	7.1
CR2O3	0.76	0.74	0.83	0.69	0.69	0.78	0.50	0.6	0.84	0.84	1.7
FEO	14.9	15.1	15.3	11.2	19.7	20.1	1.05	17.2	12.3	13.8	2.5
MNO	0.67	0.69	0.38	0.63	0.79	0.76	0.08	0.6	0.54	0.83	0.9
MGO	27.4	27.3	27.0	30.9	23.0	23.0	37.4	25.6	29.8	28.6	19.8
CAO	1.00	1.08	1.48	0.42	1.25	1.50	0.97	1.6	0.88	0.74	12.3
NA2O	0.09	0.15	0.02	0.02	0.20	0.20	0.09	0.2	0.06	0.11	2.0
K2O	b.d.	b.d.	b.d.	b.d.	0.03	0.02	0.02	b.d.	0.03	b.d.	0.3
NIO	b.d.	0.02	b.d.	0.03	b.d.	b.d.	b.d.	b.d.	b.d.	b.d.	0.3
TOTAL	100.5	100.8	100.9	100.7	100.4	100.2	100.5	100.4	100.8	100.7	99.7
WO	1.95	2.10	2.88	0.80	2.54	3.02	1.80	3.20	1.68	1.43	28.98
EN	74.29	73.92	73.23	81.63	65.06	64.27	96.56	69.64	79.21	76.54	64.90
FS	23.76	23.98	23.89	17.57	32.41	32.71	1.64	27.15	19.11	22.04	6.12
JD	0.00	0.00	0.14	0.00	1.45	0.00	0.60	0.00	0.00	0.00	14.25
AE	0.01	0.01	0.00	0.00	0.00	0.02	0.00	0.02	0.01	0.01	0.00

Abbreviations: c = core, r = rim.

Object	TS14_10	TS26_2	TS28_15	TS32_6	TS32	TS47_9
Glass						
SiO2	61.0	48.7	53.4	59.2	60.4	57.8
TiO2	0.4	0.7	0.6	0.3	0.5	0.5
A12O3	14.5	5.5	5.6	14.8	13.7	22.4
Cr2O3	0.4	0.1	0.2	0.1	0.2	0.1
FeO	4.6	22.8	18.8	2.7	4.4	1.8
MnO	b.d.	0.8	0.7	b.d.	0.1	0.1
MgO	5.0	13.7	13.1	5.0	7.3	2.6
CaO	3.3	3.6	4.3	7.7	10.1	6.3
Na2O	10.0	2.4	2.9	9.5	2.6	8.1
K2O	0.1	0.3	0.5	0.1	0.1	0.2
P2O5	0.3	0.9	b.d.	0.3	n.a.	b.d.
SO3	b.d.	0.4	0.1	0.2	n.a.	b.d.
TOTAL	99.7	100.0	100.0	100.0	99.3	99.8

Abbreviations: n.a. = not analyzed; b.d. = below dedection limit.

Object	TS19_2c	TS19_r	TS27_34	TS32_5	TS32_16	TS32	TS47_16
Olivine							
SIO2	39.0	36.9	36.2	38.7	36.1	37.0	37.4
TIO2	0.1	0.02	0.1	b.d.	b.d.	b.d.	0.3
AL2O3	b.d.	0.07	b.d.	b.d.	0.3	0.03	0.2
FEO	25.9	31.3	38.4	27.6	33.5	30.6	42.0
MNO	0.4	0.33	0.3	0.8	0.3	0.32	0.4
MGO	33.8	31.7	23.8	32.1	28.2	32.7	18.3
TOTAL	99.3	100.7	99.8	99.8	99.8	100.7	99.0
XFA	0.30	0.36	0.47	0.33	0.40	0.34	0.56

(*continued on next page*)

Appendix B (*continued*)

Object	TS19_2c	TS19_r	TS27_34	TS32_5	TS32_16	TS32	TS47_16
XFO	0.70	0.64	0.53	0.67	0.60	0.66	0.44

Abbreviations: c = core, r = rim, b.d. = below dedection lir. Na, Ca, K: below dedection limit.

Representative analysis of mineral phases in the UOC: SAHARA 97210

Object	SO2	SO3	SO5_1	SO5_2	SO5	SO6	SO7	SO11	SO11_1	SO13	SO14	SO14_1
Pyroxene												
SIO2	55.5	52.4	53.9	52.6	55.0	55.7	55.7	53.0	56.6	56.4	59.1	52.5
TIO2	0.14	0.03	0.03	0.07	0.23	0.05	0.11	0.23	0.03	0.04	0.02	0.85
AL2O3	1.13	0.30	0.71	0.74	8.7	0.31	0.83	2.04	0.46	0.55	0.20	9.0
CR2O3	0.82	0.64	0.65	0.75	0.25	0.58	1.96	1.35	0.59	0.43	0.28	2.16
FEO	11.4	25.4	18.5	22.2	10.0	13.9	11.7	12.2	9.7	10.1	4.6	2.8
MNO	0.63	0.68	0.45	0.77	0.29	0.66	0.64	1.04	0.46	0.18	0.23	0.97
MGO	25.8	20.2	24.9	22.4	15.4	27.4	27.2	20.2	31.5	30.8	35.4	15.3
CAO	5.7	0.69	1.12	0.80	8.5	1.45	1.18	9.6	0.56	1.18	0.22	16.1
NA2O	0.36	0.03	0.13	0.07	1.02	0.06	0.68	0.32	0.08	0.03	0.03	0.59
K2O	0.03	b.d.	0.03	b.d.	0.35	b.d.	b.d.	b.d.	b.d.	b.d.	0.02	0.17
TOTAL	101.5	100.3	100.4	100.3	99.7	100.1	100.0	100.0	100.0	99.7	100.1	100.4
WO	11.17	1.40	2.21	1.61	22.35	2.85	2.43	20.03	1.07	2.27	0.41	39.91
EN	70.36	57.13	68.52	62.45	56.51	74.88	77.81	58.48	83.72	82.30	92.47	52.77
FS	18.47	41.47	29.27	35.94	21.15	22.27	19.76	21.49	15.22	15.44	7.12	7.32
JD	2.50	0.00	0.00	0.00	8.86	0.43	4.82	2.36	0.55	0.21	0.20	5.03
AE	0.00	0.00	0.01	0.01	0.00	0.00	0.00	0.00	0.00	0.00	0.00	0.00

Object	SO3	SO4	SO6	SO7_1	SO7_2	SO11	SO13	SO14
Glass								
SiO2	61.1	67.3	69.1	98.5	68.9	60.5	47.5	61.6
TiO2	0.1	0.43	0.47	0.08	0.42	0.60	0.06	0.47
A12O3	8.1	10.4	15.7	0.94	18.6	20.6	33.1	18.6
Cr2O3	0.5	0.22	0.19	0.03	0.15	0.21	b.d.	0.35
FeO	13.3	4.2	2.65	0.40	2.21	2.8	0.67	2.55
MnO	0.3	0.13	0.09	0.02	0.05	0.07	0.00	0.07
MgO	9.4	5.8	3.4	0.11	2.6	4.0	0.63	4.8
CaO	1.1	7.8	3.8	0.13	2.21	3.8	15.9	5.2
Na2O	0.9	1.71	3.5	0.17	2.9	2.6	2.61	1.45
K2O	0.7	0.64	0.67	0.04	0.42	1.05	0.06	0.94
P2O5	n.a.	n.a.	n.a.	n.a.	n.a.	n.a.	n.a.	n.a.
SO3	n.a.	n.a.	n.a.	n.a.	n.a.	n.a.	n.a.	n.a.
TOTAL	95.5	98.6	99.5	100.4	98.5	96.2	100.6	96.0

Abbreviations: n.a. = not analyzed; b.d. = below dedection limit.

Object	SO1	SO4	SO5	SO6	SO11	SO13	SO14
Olivine							
SIO2	41.4	37.1	36.5	37.7	38.7	39.4	39.1
TIO2	0.11	0.01	0.05	0.02	0.06	0.00	0.09
AL2O3	1.36	0.01	0.77	0.02	2.28	0.01	0.16
CR2O3	0.41	0.10	0.10	b.d.	0.10	0.05	0.21
FEO	23.3	28.7	30.3	30.8	25.5	16.9	18.8
MNO	0.40	0.45	0.47	0.47	0.44	0.19	0.16
MGO	32.8	33.9	30.8	31.1	31.8	43.8	42.0
TOTAL	99.7	100.2	98.9	100.0	98.9	100.3	100.5
XFA	0.28	0.32	0.36	0.36	0.31	0.18	0.20
XFO	0.72	0.68	0.64	0.64	0.69	0.82	0.80

Note. Ca, Na, K: below dedection limit.

Appendix C

Bulk chemical compositions and CIPW norm calculations of individual object in Ordinary Type 3 chondrites

SAMPLE	BP1*	BP2	BP3*	BP4	BP5*	BP6*	BP7*	BP8*
BISHUMPUR								
SIO2	55.9	49.0	52.5	57.3	49.3	57.6	50.9	53.9

Appendix C (*continued*)

SAMPLE	BP1*	BP2	BP3*	BP4	BP5*	BP6*	BP7*	BP8*
TIO2	0.09	0.2	0.14	b.d.	0.15	0.08	0.12	0.07
AL2O3	2.08	4.0	3.04	1.8	3.1	1.87	2.44	0.89
CR2O3	0.63	1.0	0.69	1.1	0.72	0.58	0.76	0.69
FEO	16.6	8.2	12.4	7.9	11.5	17.4	16.7	17.1
MNO	0.62	0.6	0.61	0.7	0.43	0.65	0.71	0.84
MGO	21.7	30.3	26.0	26.5	31.5	18.6	25.4	22.3
CAO	1.40	2.2	1.80	1.6	2.10	1.45	1.74	1.30
NA2O	0.67	2.5	1.58	2.9	1.46	1.11	0.87	0.50
K2O	0.14	0.3	0.22	b.d.	0.18	0.20	0.06	0.06
P2O5	0.10	b.d.	0.05	b.d.	b.d.	0.06	0.09	0.03
S	0.14	0.5	0.07	b.d.	0.03	0.16	0.11	0.16
NI	b.d.	0.4	0.12	b.d.	b.d.	0.02	b.d.	0.04
TOTAL	100.2	99.8	100.0	99.9	100.5	99.9	100.0	98.1
(numbers in wt%)								
Q	2.77	0.00	0.00	5.93	0.00	11.49	0.00	1.13
C	0.00	0.00	0.00	0.00	0.00	0.00	0.00	0.00
OR	0.83	1.82	1.32	0.00	1.07	1.20	0.36	0.37
AB	5.70	0.00	13.59	0.00	12.38	0.00	7.42	4.36
AN	2.27	0.00	0.56	0.00	1.24	0.00	2.60	0.01
NS	0.00	5.06	0.00	5.78	0.00	2.21	0.00	0.00
DI	3.36	8.90	6.60	6.39	7.30	5.65	4.52	5.25
DIWO	1.73	4.68	3.44	3.36	3.82	2.89	2.33	2.70
DIEN	1.04	3.49	2.32	2.45	2.73	1.62	1.46	1.61
DIFS	0.60	0.73	0.84	0.58	0.75	1.15	0.73	0.95
HY	84.68	55.69	53.28	80.08	28.63	77.51	60.11	88.70
HYEN	53.70	46.07	39.10	64.67	22.46	45.38	40.12	55.85
HYFS	30.99	9.62	14.18	15.41	6.18	32.13	20.00	32.85
OL	0.00	24.37	24.27	0.00	49.08	0.00	24.57	0.00
OLFO	0.00	19.81	17.33	0.00	37.65	0.00	15.85	0.00
OLFA	0.00	4.57	6.94	0.00	11.43	0.00	8.72	0.00
IL	0.17	0.39	0.27	0.00	0.29	0.15	0.23	0.14
AP	0.22	0.00	0.11	0.00	0.02	0.13	0.20	0.07

Notes. Measured with SEM or EMPA (* EMPA analyses). b.d. = below dedection limit.

Bulk chemical compositions and CIPW norm calculations of individual objects in Ordinary Type 3 chondrites

SAMPLE	KR1*	KR2	KR3	KR5	KR6	KR7	KR12
KRYMKA							
SIO2	61.8	61.1	52.0	57.6	56.5	56.5	46.2
TIO2	0.13	0.2	0.3	0.2	0.3	0.3	0.4
AL2O3	2.9	3.1	1.9	2.1	1.7	2.0	12.0
CR2O3	0.78	1.0	0.9	0.5	0.7	0.9	0.2
FEO	4.1	7.1	19.9	6.4	18.8	12.2	4.7
MNO	0.85	1.1	0.8	0.2	0.8	0.9	0.2
MGO	26.3	23.4	21.0	30.4	18.5	23.8	24.2
CAO	1.71	1.7	1.4	1.9	1.7	1.8	7.7
NA2O	1.27	0.5	0.1	0.3	0.2	0.2	2.8
K2O	0.43	0.2	0.3	0.1	0.3	0.1	0.3
P2O5	b.d.	b.d.	0.1	0.1	0.2	0.1	0.2
S	0.09	0.1	0.4	0.1	0.1	0.4	0.3
NI	0.02	0.2	0.2	0.2	0.2	0.2	0.2
TOTAL	100.4	99.8	99.7	100.2	100.2	99.8	99.8
(numbers in wt%)							
Q	7.40	12.81	0.00	1.74	8.22	5.96	0.00
C	0.00	0.00	0.00	0.00	0.00	0.00	0.00
OR	2.56	1.20	1.81	0.60	1.79	0.60	1.80
AB	10.79	4.29	0.86	2.55	1.71	1.73	12.24
AN	0.81	5.71	3.93	4.11	2.88	4.35	19.53
NE	0.00	0.00	0.00	0.00	0.00	0.00	6.36
DI	6.04	2.28	2.11	3.78	3.65	3.36	14.20

(*continued on next page*)

Appendix C (*continued*)

SAMPLE	KR1*	KR2	KR3	KR5	KR6	KR7	KR12
DIWO	3.20	1.20	1.08	2.00	1.86	1.74	7.52
DIEN	2.51	0.87	0.60	1.54	1.01	1.16	5.88
DIFS	0.34	0.22	0.43	0.24	0.78	0.46	0.80
HY	72.14	73.34	89.20	86.61	80.74	83.21	0.00
HYEN	63.61	58.58	52.05	74.99	45.70	59.62	0.00
HYFS	8.52	14.75	37.15	11.62	35.04	23.59	0.00
OL	0.00	0.00	1.29	0.00	0.00	0.00	44.66
OLFO	0.00	0.00	0.72	0.00	0.00	0.00	38.81
OLFA	0.00	0.00	0.57	0.00	0.00	0.00	5.85
IL	0.25	0.39	0.58	0.38	0.58	0.58	0.77
AP	0.02	0.00	0.22	0.22	0.44	0.22	0.44

Notes. Measured with SEM or EMPA (* EMPA analyses). b.d. = below dedection limit.

Bulk chemical compositions and CIPW norm calculations of individual objects in Ordinary Type 3 chondrites

SAMPLE	MM2	MM4*	MM5	MM6	MM7*	MM10*	MM11	MM12	MM13	MM15*	MM17*	MM19	MM21	MM22*
MEZÖ-MADARAS														
SIO2	58.0	52.1	56.6	51.0	56.2	51.5	52.3	49.8	58.2	59.5	47.5	46.5	52.8	49.6
TIO2	b.d.	0.36	0.2	0.5	0.19	0.06	0.50	0.1	0.1	0.10	0.05	1.0	b.d.	0.48
AL2O3	1.8	7.6	2.3	3.6	3.7	0.36	3.4	0.9	1.0	2.22	0.29	10.0	0.4	5.2
CR2O3	1.0	0.42	0.1	0.7	0.82	0.46	0.7	1.3	0.5	0.73	0.55	0.7	0.3	0.77
FEO	7.5	3.8	5.0	7.0	8.1	15.1	12.7	20.0	8.0	8.1	19.1	11.9	17.9	14.9
MNO	0.3	0.18	0.6	b.d.	0.53	0.44	0.50	0.8	b.d.	0.78	0.42	0.2	0.4	0.29
MGO	25.0	29.6	29.0	29.5	26.1	31.0	24.6	20.7	27.7	25.4	31.7	20.6	27.0	23.8
CAO	1.7	4.8	1.0	2.0	2.30	0.44	1.80	1.2	2.1	1.92	0.38	2.2	0.4	1.30
NA2O	3.0	1.59	3.9	4.9	1.84	0.02	1.70	1.3	1.2	0.97	0.05	5.8	b.d.	2.9
K2O	b.d.	0.06	0.1	b.d.	0.08	b.d.	0.36	b.d.	0.2	0.31	b.d.	0.1	b.d.	0.04
P2O5	0.4	0.04	0.2	0.2	0.02	b.d.	0.30	0.1	0.2	0.01	0.04	0.5	0.1	0.30
S	0.4	0.04	0.1	0.3	0.1	b.d.	0.2	1.2	b.d.	0.06	b.d.	0.3	0.1	0.11
NI	b.d.	b.d.	0.6	0.2	b.d.	b.d.	0.6	0.6	0.8	0.04	b.d.	b.d.	0.1	0.66
TOTAL	99.4	100.6	100.0	100.3	100.1	99.3	100.0	99.4	100.2	100.2	100.1	99.9	99.6	99.7
(numbers in wt%)														
Q	10.01	0.00	3.64	0.00	0.00	0.00	0.00	0.00	6.22	5.13	0.00	0.00	0.00	0.00
C	0.00	0.00	0.00	0.00	0.00	0.00	0.00	0.00	0.00	0.00	0.00	0.00	0.00	0.00
OR	0.00	0.35	0.60	0.00	0.48	0.00	2.17	0.00	1.20	1.85	0.06	0.48	0.00	0.24
AB	0.00	13.42	0.00	0.00	15.70	0.17	14.64	0.00	0.00	8.26	0.42	27.03	0.00	24.63
AN	0.00	13.36	0.00	0.00	1.56	0.90	0.59	0.00	0.00	0.79	0.54	1.14	1.10	1.10
NE	0.00	0.00	0.00	0.00	0.00	0.00	0.00	0.00	0.00	0.00	0.00	12.05	0.00	0.00
NS	6.04	0.00	7.76	9.77	0.00	0.00	0.00	2.70	2.39	0.00	0.00	0.00	0.00	0.00
DI	4.95	8.12	3.02	7.00	7.83	1.00	5.39	4.63	7.43	6.96	0.90	5.50	0.25	2.94
DIWO	2.60	4.32	1.60	3.70	4.11	0.52	2.80	2.36	3.91	3.65	0.47	2.85	0.13	1.52
DIEN	1.91	3.48	1.25	2.84	3.00	0.35	1.88	1.31	2.91	2.64	0.30	1.89	0.08	0.98
DIFS	0.44	0.32	0.17	0.46	0.71	0.13	0.71	0.96	0.61	0.67	0.14	0.75	0.04	0.44
HY	76.27	33.09	81.95	64.92	64.41	75.24	54.22	88.63	81.34	76.81	53.36	0.00	89.17	25.95
HYEN	62.06	30.32	72.06	55.83	52.07	55.10	39.28	51.11	67.25	61.31	36.75	0.00	59.56	17.84
HYFS	14.21	2.77	9.89	9.09	12.34	20.14	14.94	37.52	14.08	15.50	16.61	0.00	29.61	8.11
OL	0.00	30.89	0.00	13.26	9.62	22.56	21.36	2.67	0.00	0.00	44.54	50.83	9.26	43.56
OLFO	0.00	28.05	0.00	11.24	7.62	16.07	15.05	1.48	0.00	0.00	29.72	35.29	5.98	29.00
OLFA	0.00	2.83	0.00	2.02	1.99	6.49	6.32	1.20	0.00	0.00	14.82	15.54	3.28	14.55
IL	0.00	0.68	0.38	0.96	0.36	0.12	0.97	0.20	0.19	0.19	0.10	1.85	0.00	0.92
AP	0.89	0.09	0.44	0.44	0.04	0.02	0.67	0.23	0.44	0.02	0.09	1.13	0.22	0.66

Note. Measured with SEM or EMPA (* EMPA analyses).

Bulk chemical compositions and CIPW norm calculations of individual objects in Ordinary Type 3 chondrites

SAMPLE	TS10	TS14	TS19	TS20	TS24*	TS26*	TS27	TS28*	TS32	TS37*	TS44*
TIESCHITZ											
SIO2	37.3	49.8	46.3	54.3	52.3	52.4	58.0	51.2	47.9	53.6	54.2
TIO2	b.d.	0.5	0.6	b.d.	0.05	0.07	0.6	0.09	0.2	0.10	0.07
AL2O3	2.3	1.2	2.0	1.0	0.85	1.02	3.4	1.25	2.1	0.84	0.36

Appendix C (*continued*)

SAMPLE	TS10	TS14	TS19	TS20	TS24*	TS26*	TS27	TS28*	TS32	TS37*	TS44*
CR2O3	0.6	0.4	0.5	1.0	0.86	0.76	0.9	0.75	1.0	0.72	0.87
FEO	30.8	17.2	19.0	13.0	19.9	20.3	2.6	19.1	17.6	4.3	13.6
MNO	0.5	0.5	0.5	0.6	0.76	0.75	0.4	0.52	0.2	0.03	0.84
MGO	23.8	22.7	26.6	24.3	23.3	22.3	28.9	25.2	25.5	40.3	27.6
CAO	1.9	1.4	1.2	2.2	1.36	1.74	2.7	1.59	1.8	0.97	1.55
NA2O	0.5	2.8	2.6	1.0	0.30	0.32	1.8	0.32	2.7	0.07	0.14
K2O	b.d.	b.d.	b.d.	0.1	0.02	0.03	0.1	0.04	0.1	b.d.	b.d.
P2O5	1.0	0.7	0.3	0.6	0.02	0.05	b.d.	0.05	0.7	b.d.	b.d.
S	0.4	1.1	b.d.	0.3	0.47	0.16	b.d.	0.02	0.1	b.d.	b.d.
NI	b.d.	b.d.	0.2	0.8	0.06	0.39	0.6	b.d.	b.d.	0.02	b.d.
TOTAL	99.5	99.4	99.8	99.6	100.7	100.6	100.1	100.1	100.0	100.9	99.2
(numbers in wt%)											
Q	0.00	0.00	0.00	3.73	0.00	0.00	0.00	0.00	0.00	0.00	0.00
C	0.17	0.00	0.00	0.00	0.00	0.00	0.00	0.00	0.00	0.00	0.00
OR	0.00	0.00	0.00	0.61	0.12	0.18	0.60	0.24	0.66	0.00	0.06
AB	4.31	0.00	0.00	0.00	2.56	2.73	15.44	2.72	0.00	0.59	1.20
AN	3.63	0.00	0.00	0.00	0.92	1.27	0.91	1.87	0.00	1.97	0.33
NS	0.00	5.69	5.16	2.03	0.00	0.00	0.00	0.00	5.44	0.00	0.00
DI	0.00	2.38	3.43	5.92	4.72	5.85	9.93	4.70	3.77	2.17	5.97
DIWO	0.00	1.22	1.77	3.07	2.42	2.99	5.30	2.42	1.95	1.16	3.10
DIEN	0.00	0.74	1.09	2.02	1.40	1.69	4.36	1.45	1.21	0.94	2.07
DIFS	0.00	0.41	0.57	0.83	0.91	1.17	0.27	0.83	0.61	0.07	0.79
HY	7.58	82.79	53.44	85.45	82.78	82.94	68.75	71.66	62.10	65.85	87.81
HYEN	3.86	53.16	35.07	60.58	50.19	49.02	64.71	45.65	41.20	61.10	63.47
HYFS	3.72	29.63	18.37	24.88	32.59	33.91	4.05	26.01	20.90	4.75	24.34
OL	82.09	5.35	34.22	0.00	8.77	6.80	3.21	18.53	24.12	29.20	4.48
OLFO	39.75	3.31	21.68	0.00	5.11	3.86	3.00	11.38	15.46	26.89	3.15
OLFA	42.33	2.04	12.54	0.00	3.66	2.94	0.21	7.16	8.66	2.31	1.33
IL	0.00	0.98	1.07	0.00	0.10	0.13	1.16	0.17	0.31	0.19	0.14
AP	2.23	1.58	0.66	1.35	0.04	0.11	0.00	0.11	1.59	0.02	0.02

Notes. Measured with SEM or EMPA (* EMPA analyses). b.d. = below dedection limit.

Bulk chemical compositions and CIPW norm calculations of individual objects in Ordinary Type 3 chondrites

SAMPLE	SO1*	SO2*	SO3*	SO4	SO5	SO6	SO7	SO8	SO9	SO10*	SO11	SO12*	SO13c*	SO13a*	SO14
SAHARA 97210															
SIO2	45.0	56.4	51.4	45.5	48.7	49.2	57.8	43.6	47.9	49.2	51.0	47.9	46.3	46.0	53.1
TIO2	0.17	0.10	0.12	0.1	0.5	0.2	0.2	0.2	0.1	0.07	0.3	0.15	0.12	0.12	0.3
AL2O3	2.39	2.26	1.19	1.1	1.0	1.6	2.2	2.4	2.3	1.09	1.8	3.2	1.94	1.61	3.0
CR2O3	0.84	0.78	0.87	0.6	0.1	0.5	0.8	0.6	0.5	0.66	0.8	0.68	0.44	0.43	0.5
FEO	19.6	11.0	25.4	27.6	23.6	24.4	13.0	21.6	21.5	21.3	21.1	12.8	13.1	15.1	13.2
MNO	0.56	0.57	0.65	0.6	1.3	0.4	0.5	0.4	0.6	0.48	0.4	0.39	0.19	0.22	0.3
MGO	26.5	25.7	18.2	21.0	21.7	21.0	23.0	28.5	21.3	23.9	22.1	31.8	34.8	33.6	24.3
CAO	3.5	1.65	0.93	2.6	1.0	2.1	1.8	2.2	1.7	1.70	2.2	0.83	1.92	1.75	2.5
NA2O	1.11	1.14	0.34	0.1	0.4	0.1	b.d.	0.2	0.5	0.59	0.1	1.32	0.14	0.15	0.6
K2O	0.24	0.17	0.12	0.1	0.2	0.1	0.1	0.1	0.1	0.06	0.2	0.85	0.04	0.05	0.3
P2O5	0.06	b.d.	0.12	b.d.	0.1	0.1	0.2	0.0	0.2	0.06	b.d.	0.01	0.06	0.05	0.3
S	0.10	0.20	0.23	b.d.	b.d.	0.1	0.1	b.d.	1.2	0.10	0.5	b.d.	0.17	0.13	0.5
NI	0.12	0.55	0.08	0.2	0.4	0.2	0.2	0.2	0.2	0.04	0.3	b.d.	0.08	0.23	0.2
TOTAL	100.3	101.0	99.9	99.7	99.2	100.2	100.1	100.2	99.4	99.4	101.3	99.9	99.5	99.6	99.6
(numbers in wt%)															
Q	0.00	0.00	0.00	0.00	0.00	0.00	9.01	0.00	0.00	0.00	0.00	0.00	0.00	0.00	0.00
OR	1.43	1.01	0.72	0.60	1.20	0.60	0.60	0.60	0.49	0.36	1.25	5.07	0.24	0.30	1.81
AB	9.47	9.72	2.92	0.86	3.43	0.85	0.00	1.70	4.22	5.07	1.02	11.24	1.20	1.29	5.18
AN	0.83	0.55	1.39	2.28	0.35	3.65	5.77	5.39	4.01	0.15	3.67	0.26	4.61	3.62	4.70
DI	13.13	6.12	2.14	8.92	3.37	5.16	1.68	4.56	2.81	6.58	6.12	3.06	3.75	3.91	4.97
DIWO	6.76	3.19	1.08	4.50	1.71	2.62	0.87	2.34	1.43	3.37	3.13	1.60	1.96	2.04	2.58
DIEN	4.10	2.21	0.52	2.23	0.91	1.37	0.57	1.42	0.78	1.93	1.76	1.12	1.40	1.41	1.71
DIFS	2.27	0.72	0.54	2.19	0.75	1.17	0.24	0.80	0.59	1.29	1.24	0.34	0.39	0.47	0.68
HY	14.25	79.97	89.05	48.55	67.23	70.58	82.12	27.51	65.53	59.56	74.98	22.88	36.57	36.95	76.03

(*continued on next page*)

Appendix C (*continued*)

SAMPLE	SO1*	SO2*	SO3*	SO4	SO5	SO6	SO7	SO8	SO9	SO10*	SO11	SO12*	SO13c*	SO13a*	SO14
HYEN	9.18	60.20	43.62	24.50	36.80	37.95	57.63	17.62	37.29	35.72	43.98	17.59	28.64	27.75	54.33
HYFS	5.08	19.77	45.44	24.05	30.43	32.63	24.49	9.89	28.24	23.84	31.00	5.29	7.93	9.20	21.70
OL	60.43	2.41	3.29	38.61	23.25	18.57	0.00	59.86	22.22	28.03	12.40	57.18	53.27	53.60	6.07
OLFO	37.53	1.77	1.53	18.53	12.16	9.53	0.00	36.95	12.10	16.14	6.97	42.93	40.80	39.23	4.21
OLFA	22.90	0.64	1.76	20.08	11.10	9.04	0.00	22.91	10.12	11.89	5.43	14.26	12.47	14.36	1.86
IL	0.33	0.19	0.23	0.19	0.96	0.38	0.38	0.38	0.24	0.14	0.56	0.29	0.23	0.23	0.58
AP	0.13	0.02	0.27	0.00	0.22	0.22	0.44	0.00	0.50	0.13	0.00	0.02	0.13	0.11	0.67

Notes. Measured with SEM or EMPA (* EMPA analyses). b.d. = below dedection limit.

Appendix D

Trace element analyses of objects and phases in ordinary chondrites (LA-ICP-MS analyses)

Object	BP1	BP2	BP3	BP4	BP5	BP6	BP7	BP8	KR1	KR2	KR3	KR5	KR6	KR7	KR7r	KR14	KR12
Chondrite Bishunpur									*Krymka*								
Zr	4.57	8.14	6.40	4.85	5.77	3.08	5.49	3.88	5.20	5.19	3.29	6.22	1.62	1.97	2.24	6.06	13.81
Hf	0.14	0.24	0.18	0.12	0.15	0.08	0.16	0.10	0.15	0.14	0.09	0.16	0.24	0.19	0.13	0.21	0.61
Sc	b.d.	10.60	10.51	9.63	9.62	6.70	9.60	8.74	8.85	10.74	6.14	10.71	7.05	8.51	b.d.	b.d.	35.74
Y	1.92	3.25	2.61	1.90	2.38	1.26	2.22	1.52	2.16	2.14	1.33	2.29	2.07	1.82	1.66	2.50	8.43
Nb	0.38	0.65	0.54	0.42	0.48	0.27	0.47	0.37	0.49	0.51	0.29	0.61	0.68	0.51	0.33	0.50	1.84
Ta	0.01	0.03	0.03	0.02	0.03	0.01	0.02	0.01	0.02	0.02	0.01	0.03	0.04	0.02	0.02	0.04	0.10
Ti	0.07	0.12	0.09	0.07	0.08	0.04	0.08	0.05	0.07	0.08	0.05	0.09	0.00	0.00	0.00	0.09	0.00
Ca	1.06	1.80	1.67	1.36	1.42	0.89	1.20	1.05	1.05	1.27	0.98	1.84	1.36	0.94	1.22	1.69	5.26
Th	0.03	0.07	0.05	0.04	0.05	0.05	0.04	0.03	0.04	0.04	0.03	0.05	0.07	0.05	0.04	0.07	0.26
U	0.01	0.02	0.01	0.01	0.01	0.01	0.01	0.01	0.02	0.03	0.01	0.03	0.03	0.02	0.01	0.03	0.10
La	0.29	0.53	0.43	0.29	0.41	0.20	0.37	0.26	0.35	0.35	0.21	0.40	0.39	0.31	0.25	0.40	1.59
Ce	0.74	1.52	1.10	0.82	1.15	0.50	0.96	0.68	0.93	1.01	0.57	1.25	0.82	0.69	0.64	0.99	4.51
Pr	0.11	0.21	0.16	0.12	0.16	0.07	0.14	0.09	0.13	0.13	0.07	0.15	0.22	0.15	0.11	0.14	0.71
Nd	0.33	1.02	0.78	0.62	0.67	0.36	0.68	0.44	0.68	0.66	0.38	0.73	0.73	0.58	0.53	0.89	2.94
Sm	0.16	0.33	0.23	0.18	0.25	0.14	0.21	0.14	0.23	0.21	0.13	0.24	0.38	0.23	0.20	0.29	1.04
Eu	0.04	0.03	0.11	0.06	0.10	0.04	0.03	0.05	0.08	0.06	0.05	0.13	0.14	0.04	0.04	0.10	0.38
Tb	0.04	0.09	0.07	0.04	0.06	0.03	0.05	0.03	0.05	0.05	0.03	0.05	0.09	0.06	0.05	0.09	0.24
Gd	0.26	0.47	0.35	0.24	0.38	0.16	0.31	0.20	0.31	0.31	0.18	0.29	0.49	0.34	0.24	0.46	1.30
Dy	0.33	0.57	0.43	0.32	0.39	0.21	0.39	0.27	0.36	0.37	0.21	0.40	0.61	0.43	0.37	0.46	1.62
Ho	0.07	0.12	0.09	0.07	0.10	0.05	0.08	0.05	0.08	0.09	0.05	0.09	0.16	0.10	0.09	0.09	0.36
Er	0.18	0.34	0.29	0.21	0.25	0.14	0.27	0.17	0.23	0.24	0.15	0.28	0.40	0.27	0.22	0.39	1.02
Tm	0.03	0.05	0.04	0.03	0.04	0.02	0.04	0.02	0.03	0.03	0.02	0.04	0.07	0.04	0.04	0.08	0.18
Yb	0.19	0.39	0.33	0.23	0.28	0.14	0.27	0.18	0.26	0.25	0.15	0.27	0.37	0.32	0.24	0.45	1.04
Lu	0.04	0.06	0.04	0.03	0.04	0.02	0.05	0.03	0.04	0.04	0.02	0.04	0.07	0.05	0.04	0.04	0.17
Sr	5.0	5.3	11.5	9.1	12.5	2.2	6.3	6.3	6.8	4.0	7.4	17.3	1.05	0.24	1.80	14.6	36.3
Ba	1.6	1.6	3.9	3.2	4.6	1.4	2.8	1.8	3.3	3.1	2.7	3.8	0.22	0.05	0.46	2.24	8.1
V	59.4	88.2	81.1	82.7	83.1	53.8	79.0	62.5	71.9	85.3	60.1	95.6	10.8	17.9	27.1	79.0	42.3
Cr	5032	5289	5264	5199	4743	3927	5343	4784	5746	6912	4834	5723	5898	6580	6076	4474	1415
Mn	0.47	0.33	0.38	0.44	0.32	0.46	0.53	0.63	0.60	0.66	0.49	0.38	0.02	0.04	0.07	0.40	87.5
Rb	4.27	6.15	2.75	4.45	7.43	5.93	1.23	4.09	17.48	4.10	9.33	4.60	4.60	0.49	1.28	10.35	0.39
Cs	0.15	0.27	0.12	0.20	0.18	0.25	b.d.	0.20	0.22	0.04	0.20	0.34	0.45	0.11	0.09	b.d.	0.05
W	0.04	b.d.	0.06	0.09	0.09	0.03	b.d.	0.05	n.a.	0.02	0.03	0.07	0.06	0.01	b.d.	n.a.	0.10

Notes. Numbers are given in ppm with exception of Ti, Ca, and Mn that are given in wt%. b.d. = below dedection limit.

Trace element analyses of objects and phases in Ordinary chondrites (LA-ICP-MS analyses)

Object	MM2	MM4c	MM4r	MM5	MM6	MM7	MM10	MM11	MM12	MM13	MM15	MM17	MM19BO	MM19gl	MM21	MM22	MM13ol
Chondrite Mezö-Madaras																	
Zr	6.11	13.80	13.42	4.05	6.01	7.23	0.96	5.61	6.90	2.69	3.65	0.70	20.11	26.25	0.43	3.87	4.49
Hf	0.16	0.37	0.36	0.14	0.17	0.21	0.02	0.15	0.19	0.09	0.08	0.02	0.52	0.59	0.02	0.13	0.10
Sc	9.78	28.45	29.59	b.d.	10.51	11.01	b.d.	10.71	10.32	5.65	b.d.	b.d.	34.76	37.82	b.d.	9.69	5.88
Y	2.54	5.43	5.54	1.66	2.49	2.65	0.34	2.28	2.86	1.11	1.49	0.28	7.79	9.91	0.11	1.48	1.37
Nb	0.55	1.18	1.21	0.24	0.53	0.68	0.31	0.49	0.60	0.24	0.35	0.23	1.71	2.09	0.14	0.39	0.40
Ta	0.02	0.07	0.06	0.02	0.03	0.03	0.01	0.02	0.03	0.01	0.03	0.00	0.09	0.12	0.00	0.02	0.01
Ti	0.07	0.20	0.19	0.06	0.08	0.09	0.02	0.09	0.10	0.04	0.06	0.03	0.40	0.47	0.02	0.06	0.09
Ca	1.41	3.23	2.54	0.70	1.54	1.25	0.24	1.57	1.80	1.54	1.30	0.42	1.49	1.86	0.17	1.59	0.98
Th	0.05	0.12	0.11	0.04	0.06	0.06	0.02	0.05	0.05	0.02	0.04	0.00	0.16	0.24	0.01	0.03	0.03
U	0.06	0.04	0.04	0.01	0.02	0.02	0.01	0.01	0.01	0.02	0.00	0.03	0.12	0.10	0.01	0.01	0.02

Appendix D (*continued*)

Object	MM2	MM4c	MM4r	MM5	MM6	MM7	MM10	MM11	MM12	MM13	MM15	MM17	MM19BO	MM19gl	MM21	MM22	MM13ol
La	0.41	1.00	0.97	0.24	0.42	0.42	0.17	0.37	0.46	0.20	0.26	0.12	1.42	1.98	0.08	0.26	0.20
Ce	1.10	2.70	2.70	0.67	1.14	1.16	1.05	0.99	1.23	0.63	0.67	0.89	3.80	5.06	0.72	0.70	0.55
Pr	0.15	0.39	0.37	0.10	0.15	0.16	0.08	0.14	0.18	0.07	0.10	0.04	0.57	0.76	0.03	0.09	0.07
Nd	0.78	1.74	2.07	0.39	0.75	0.75	0.28	0.76	0.81	0.37	0.64	0.16	2.80	4.15	0.15	0.43	0.40
Sm	0.25	0.66	0.65	0.17	0.29	0.27	0.09	0.24	0.34	0.09	0.13	0.03	0.89	1.46	b.d.	0.12	0.16
Eu	0.03	0.27	0.07	b.d.	0.08	0.09	0.01	0.05	0.07	0.10	0.01	0.02	0.12	0.08	b.d.	0.08	0.04
Tb	0.06	0.14	0.14	0.04	0.07	0.07	0.02	0.06	0.07	0.03	0.04	0.01	0.18	0.26	0.00	0.04	0.03
Gd	0.35	0.80	0.86	0.25	0.35	0.35	0.09	0.32	0.39	0.17	0.23	0.05	1.10	1.32	0.03	0.20	0.20
Dy	0.44	1.02	1.07	0.31	0.45	0.50	0.08	0.39	0.52	0.19	0.26	0.05	1.38	1.78	0.02	0.29	0.24
Ho	0.09	0.21	0.24	0.06	0.09	0.11	0.02	0.09	0.10	0.04	0.06	0.01	0.27	0.40	0.01	0.05	0.05
Er	0.28	0.61	0.62	0.21	0.25	0.32	0.04	0.26	0.34	0.14	0.23	0.03	0.82	1.13	0.02	0.16	0.13
Tm	0.04	0.10	0.09	0.03	0.04	0.04	0.01	0.04	0.05	0.02	0.04	0.01	0.13	0.16	b.d.	0.02	0.02
Yb	0.29	0.77	0.77	0.23	0.28	0.32	0.07	0.26	0.31	0.11	0.16	0.06	1.02	1.11	b.d.	0.19	0.16
Lu	0.04	0.11	0.12	0.03	0.04	0.05	0.01	0.04	0.05	0.02	0.06	0.01	0.14	0.21	b.d.	0.03	0.03
Sr	1.8	80.2	10.6	2.1	0.97	14.1	0.50	2.2	2.5	3.0	1.3	0.7	1.9	1.6	1.4	3.7	4.4
Ba	1.0	21.5	3.5	7.8	0.97	5.4	b.d.	0.96	3.4	0.44	0.74	0.29	1.1	1.1	1.1	1.3	3.5
V	77.5	71.5	72.7	75.3	82.9	92.2	49.9	84.0	84.3	79.3	76.7	83.3	133	118	90.6	79.2	56.7
Cr	6436	3278	3261	5755	5189	5686	2770	3987	5063	2700	4629	4324	3189	3163	4730	3788	3082
Mn	0.41	0.08	0.10	0.08	0.24	0.29	0.27	0.37	0.27	0.06	0.44	0.25	0.12	0.13	0.20	0.23	0.34
Rb	1.93	1.31	1.65	6.65	1.72	2.65	0.30	32.91	10.63	0.71	13.63	0.22	3.25	6.46	b.d.	2.15	1.32
Cs	1.08	0.22	0.18	0.74	0.07	0.21	b.d.	2.48	0.94	0.05	1.47	0.03	0.26	0.12	b.d.	0.37	0.07
W	b.d.	0.02	b.d.	b.d.	b.d.	0.07	0.03	0.06	0.23	0.06	0.12	0.05	0.06	0.06	0.04	0.12	0.50

Notes. Numbers are given in ppm with exception of Ti, Ca, and Mn that are given in wt%. b.d. = below dedection limit; c = core, r = rim.

Trace element analyses of objects and phases in Ordinary chondrites (LA-ICP-MS analyses)

Object	TS10	TS14c	TS14r	TS19	TS20	TS24	TS26	TS27	TS27px	TS28	TS28matrix	TS32	TS37	TS37r	TS44	TS47c
Chondrite Tieschitz																
Zr	5.27	4.78	3.74	5.90	4.61	2.75	2.55	13.42	10.61	3.45	3.92	11.65	1.37	1.16	6.07	7.66
Hf	0.16	0.12	0.08	0.15	0.14	0.04	0.07	0.36	0.28	0.12	b.d.	0.30	b.d.	b.d.	0.15	0.22
Sc	7.43	7.24	6.80	7.03	7.85	b.d.	5.86	27.54	24.02	5.32	b.d.	10.83	b.d.	b.d.	8.41	11.49
Y	1.97	2.02	1.56	2.31	1.66	0.93	1.20	5.12	3.84	1.50	1.54	3.61	0.40	0.53	2.19	2.77
Nb	0.61	0.44	0.31	0.59	0.41	0.24	0.23	0.37	0.82	0.32	0.40	0.68	0.35	0.24	0.29	0.71
Ta	0.03	0.01	0.02	0.04	0.03	b.d.	0.01	0.06	<0.07	0.01	0.02	0.05	b.d.	b.d.	0.01	0.03
Ti	0.07	0.07	0.05	0.10	0.07	0.04	0.04	0.23	0.19	0.05	0.05	0.14	0.06	0.05	0.06	0.11
Ca	1.10	1.16	1.16	1.19	1.48	1.14	0.95	2.10	1.99	0.99	0.93	1.46	0.58	0.51	1.54	1.83
Th	0.05	0.04	0.04	0.05	0.04	0.02	0.02	0.16	b.d.	0.03	b.d.	0.11	0.03	b.d.	0.06	0.06
U	b.d.	b.d.	0.02	0.03	0.01	0.02	0.02	0.02	0.03	b.d.	b.d.	0.03	0.04	b.d.	0.02	0.02
La	0.34	0.38	0.23	0.43	0.24	0.13	0.18	0.78	0.66	0.22	0.27	0.69	0.14	0.15	0.36	0.50
Ce	0.97	1.01	0.68	1.65	0.73	0.41	0.52	2.69	2.49	0.65	0.85	2.10	1.23	0.88	1.17	1.66
Pr	0.15	0.14	0.09	0.21	0.11	0.06	0.07	0.35	0.31	0.09	0.09	0.28	0.10	0.06	0.16	0.21
Nd	0.80	0.75	0.50	1.01	0.45	0.34	0.41	1.77	1.60	0.42	0.64	1.35	0.33	b.d.	0.67	1.04
Sm	0.20	0.20	0.16	0.26	0.17	b.d.	0.16	0.59	0.49	0.11	b.d.	0.39	b.d.	b.d.	0.26	0.33
Eu	0.07	0.04	0.05	0.06	0.08	0.05	0.05	0.12	0.15	0.05	0.08	0.07	0.04	0.02	0.05	0.11
Tb	0.05	0.05	0.04	0.04	0.04	0.02	0.03	0.14	0.11	0.03	0.04	0.09	0.01	b.d.	0.06	0.07
Gd	0.28	0.27	0.22	0.33	0.22	0.13	0.16	0.79	0.68	0.20	0.23	0.57	0.09	b.d.	0.37	0.40
Dy	0.28	0.34	0.27	0.40	0.27	0.16	0.24	0.79	0.66	0.30	0.35	0.71	0.08	0.11	0.46	0.52
Ho	0.08	0.08	0.05	0.09	0.07	0.03	0.05	0.18	0.14	0.05	0.06	0.14	0.02	0.00	0.09	0.10
Er	0.22	0.21	0.19	0.28	0.16	0.14	0.17	0.53	0.36	0.18	0.24	0.42	0.03	b.d.	0.25	0.28
Tm	0.04	0.03	0.02	0.03	0.03	0.02	0.02	0.09	0.07	0.03	b.d.	0.05	0.01	b.d.	0.04	0.04
Yb	0.23	0.21	0.23	0.26	0.19	0.14	0.14	0.79	0.58	0.20	0.15	0.44	b.d.	0.11	0.28	0.35
Lu	0.04	0.02	0.03	0.04	0.03	0.04	0.02	0.07	0.08	0.03	0.04	0.07	0.00	b.d.	0.04	0.05
Sr	6.4	1.8	1.5	5.4	1.2	1.7	1.5	0.70	1.7	1.2	1.7	2.8	3.5	1.1	1.1	2.3
Ba	7.1	0.47	1.6	4.7	4.7	0.30	0.45	1.4	0.54	1.6	2.4	6.4	4.0	2.0	1.5	5.2
V	68.0	62.7	68.5	81.6	78.7	55.0	55.8	138	125	71.2	59.4	100	114	112	92.8	79.6
Cr	3562	4259	4585	3910	6368	5451	5489	4602	4060	5736	4902	6518	5273	4919	8005	5184
Mn	0.18	0.35	0.36	0.21	0.42	0.45	0.46	0.09	0.07	0.33	0.29	0.29	0.03	0.10	0.51	0.22
Rb	4.79	0.20	0.44	2.54	1.24	0.99	0.94	0.41	0.90	2.15	5.31	1.66	b.d.	0.54	0.71	2.80
Cs	0.22	0.07	0.05	0.18	0.06	0.05	0.05	0.05	0.12	0.10	0.23	0.09	b.d.	b.d.	0.04	0.11
W	0.11	b.d.	0.01	0.09	b.d.	b.d.	b.d.	0.02	b.d.	0.05	0.12	0.13	0.24	0.06	0.08	0.12

Notes. Numbers are given in ppm with exception of Ti, Ca, and Mn that are given in wt%. b.d. = below dedection limit; c = core, r = rim.

References

Alexander, C.M.O'D., 2004. Chemical equilibrium and kinetic constraints for chondrule and CAI formation conditions. Geochim. Cosmochim. Acta 68, 3943–3969.

Anders, E., Grevesse, N., 1989. Abundance of the elements: Meteoritic and solar. Geochim. Cosmochim. Acta 53, 197–214.

Arrhenius, G., De, B.R., 1973. Equilibrium condensation in a solar nebula. Meteoritics 8, 297–313.

Barth, M.G., Rudnick, R.L., Horn, I., McDonough, W.F., Spicuzza, M.J., Valley, J.W., Haggerty, S.E., 2001. Geochemistry of xenolithic eclogites from West Africa, Part I. A link between low MgO eclogites and Archean Crust Formation. Geochim. Cosmochim. Acta 65, 1499–1527.

Berman, R.G., 1983. A thermodynamic model for multicomponent melts, with application to the system CaO–MgO–Al_2O_3–SiO_2. Ph.D. thesis, Univ. of British Columbia.

Berman, R.G., 1988. Internally-consistent thermodynamic data for minerals in the system Na_2O–K_2O–CaO–MgO–FeO–Fe_2O_3–Al_2O_3–SiO_2–TiO_2–H_2O–CO_2. J. Petrol. 29, 445–522.

Berman, R.G., Brown, T.H., 1985. Heat capacity of minerals in the system Na_2O–K_2O–CaO–MgO–FeO–Fe_2O_3–Al_2O_3–SiO_2–TiO_2–H_2O–CO_2. Contrib. Mineral. Petrol. 89, 168–183.

Blander, M., 1983. Condensation of chondrules. In: King, E.A. (Ed.), Chondrules and Their Origins. Lunar and Planetary Institute, Houston, pp. 1–9.

Blander, M., Abdel-Gawad, M., 1969. The origin of meteorites and the constrained equilibrium condensation theory. Geochim. Cosmochim. Acta 34, 701–716.

Blander, M., Katz, J., 1967. Condensation of primordial dust. Geochim. Cosmochim. Acta 31, 1025–1034.

Blander, M., Pelton, A.D., Jung, I.-H., Weber, R., 2005. Non-equilibrium concepts lead to a unified explanation of the formation of chondrules and chondrites. Meteorit. Planet. Sci. 39, 1897–1910.

Boynton, W.V., 1978. Rare-earth elements as indicators of supernova condensation. Lunar Planet. Sci. IX, 120–122.

Boss, A.P., 1996. A concise guide to chondrule formation models. In: Hewins, R.H., Jones, R.H., Scott, E.R.D. (Eds.), Chondrules and the Protoplanetary Disc. Cambridge Univ. Press, Cambridge, pp. 257–263.

Boss, A.P., 2006. Spatial heterogeneity of short-lived and stable isotopes in the Solar Nebula. Meteorit. Planet. Sci. Suppl. 41, A25 (abstract).

Cameron, A.G.W., 1962. The formation of the Sun and planets. Icarus 1, 13–69.

Cameron, A.G.W., 1966. The accumulation of chondritic material. Earth Planet. Sci. Lett. 1, 93–96.

Cameron, A.G.W., 1995. The first ten million years in the solar nebula. Meteoritics 30, 133–161.

Chase Jr., M.W., Davies, C.A., Downey, J.R., Frurip, D.J., McDonald, R.A., Syverud, A.N., 1985. JANAF Thermochemical Tables, third ed. J. Phys. Chem. Ref. Data 14 (Suppl. 1).

Ciesla, F.J., Hood, L.L., 2002. The nebular shock wave model for chondrule formation: Shock processing in a particle–gas suspension. Icarus 158, 281–293.

Ciesla, F.J., Hood, L.L., 2003. Evaluating planetesimal bow shocks as possible sites for chondrule formation. Lunar Planet. Sci. XXXIV. Abstract 1400.

Ciesla, F.J., Lauretta, D.S., Hood, L.L., 2004. The frequency of compound chondrules and implications for chondrule formation. Meteorit. Planet. Sci. 39, 531–544.

Davis, A.M., Tanaka, T., Grossman, L., Lee, T., Wasserburg, G.J., 1982. Chemical composition of HAL, an isotopically-unusual Allende inclusion. Geochim. Cosmochim. Acta 46, 1627–1651.

Desch, S.J., Connolly, H.C., 2002. A model of the thermal processing of particles in solar nebula shocks: Application to the cooling rates of chondrules. Meteorit. Planet. Sci. 37, 183–201.

Desch, S.J., Cuzzi, J.N., 2000. The generation of lightning in the solar nebula. Icarus 143, 87–105.

Ebel, D.S., 2005. Model evaporation of FeO-bearing liquids: Application to chondrules. Geochim. Cosmochim. Acta 69, 3183–3193.

Ebel, D.S., Alexander, C.M.O'D., 2005. Condensation from cluster-IDP enriched vapor inside the snow line: Implications for Mercury, asteroids, and enstatite chondrites. Lunar Planet. Sci. XXXVI. Abstract 1797.

Ebel, D.S., Grossman, L., 2000. Condensation in dust-enriched systems. Geochim. Cosmochim. Acta 64, 339–366.

Ebel, D.S., Engler, A., Kurat, G., 2003. Pyroxene chondrules form olivine-depleted, dust-enriched systems. Lunar Planet. Sci. XXXIV. Abstract 2059.

Engler, A., 2004. Search for solar nebula condensates in chondrites. Ph.D. thesis, Formal- und Naturwissenschaftliche Fakultät, University of Graz, Austria, 196 pp. + CD-R.

Engler, A., Kurat, G., Sylvester, P.J., 2003. Trace element abundances in micro-objects from Tieschitz (H3.6), Krymka (LL3.1), Bishunpur (LL3.1) and Mezö-Madaras (L3.7): Implications for chondrule formation. Lunar Planet. Sci. XXXIV. Abstract 1689.

Fegley Jr., B., Palme, H., 1985. Evidence for oxidizing conditions in the solar nebula from Mo and W depletions in refractory inclusions in carbonaceous chondrites. Earth Planet. Sci. Lett. 72, 311–326.

Fredriksson, K., Brenner, P.R., Fredriksson, B.J., Olsen, E., 1997. A nondestructive analytical method for stone meteorites—And a controversial discrepancy. Meteorit. Planet. Sci. 32, 55–60.

Ghiorso, M.S., Sack, R.O., 1995. Chemical mass transfer in magmatic processes. IV. A revised and internally consistent thermodynamic model for the interpolation and extrapolation of liquid–solid equilibria in magmatic systems at elevated temperatures and pressures. Contrib. Mineral. Petrol. 119, 197–212.

Gooding, J.L., Keil, K., 1981. Relative abundances of chondrule primary textural types in ordinary chondrites and their bearing on conditions of chondrule formation. Meteoritics 16, 17–43.

Gooding, J.L., Keil, K., Fukuoka, T., Schmitt, R.A., 1980. Elemental abundances in chondrules from unequilibrated chondrites: Evidence for chondrule origin by melting of pre-existing materials. Earth Planet. Sci. Lett. 50, 171–180.

Gooding, J.L., Mayeda, T.K., Clayton, R.N., Fukuoka, T., 1983. Oxygen isotopic heterogeneities, their petrological correlations and implications for melt origins of chondrules in unequilibrated ordinary chondrites. Earth Planet. Sci. Lett. 65, 209–224.

Grossman, L., 1972. Condensation in the primitive solar nebula. Geochim. Cosmochim. Acta 36, 597–619.

Grossman, J.N., 1988. Formation of chondrules. In: Kerridge, J.F., Matthews, M.S. (Eds.), Meteorites and the Early Solar System. Univ. of Arizona Press, Tucson, AZ, pp. 680–696.

Grossman, J.N., Wasson, J.T., 1982. Evidence for primitive nebular components in chondrules from the Chainpur chondrite. Geochim. Cosmochim. Acta 46, 1081–1099.

Grossman, J.N., Wasson, J.T., 1983. The composition of chondrules in unequilibrated chondrites: An evaluation of models for the formation of chondrules and their precursor materials. In: King, E.A. (Ed.), Chondrules and Their Origins. Lunar and Planetary Institute, Houston, pp. 88–121.

Grossman, J.N., Wasson, J.T., 1985. The origin and history of metal and sulfide components of chondrules. Geochim. Cosmochim. Acta 49, 925–939.

Herndon, J.M., Suess, H.E., 1977. Can the ordinary chondrites have condensed from a gas phase? Geochim. Cosmochim. Acta 41, 233–236.

Hewins, R.H., 1988. Experimental studies of chondrules. In: Kerridge, J.F., Matthews, M.S. (Eds.), Meteorites and the Early Solar System. Univ. of Arizona Press, Tucson, AZ, pp. 660–679.

Hewins, R.H., 1991. Retention of sodium during chondrule formation. Geochim. Cosmochim. Acta 55, 200–220.

Howard, E., 1802. Experiments and observations on certain stony and metallic substances which at different times are said to have fallen on the Earth; also on various kinds of native iron. Philos. Trans. R. Soc. Lond. Part I 92, 168–212.

Horn, R.W., Hinton, S.E., Jackson, Longerich, H.P., 1997. Ultra-trace element analysis of NIST SRM 616 and 614 using Laser Ablation Microprobe-Inductively Coupled Plasma-Mass Spectrometry (LAM-ICP-MS): A Comparison with Secondary Ion Mass Spectrometry (SIMS). Geostandard Newslett. 21, 191–203.

Huang, S., Lu, J., Prinz, M., Weisberg, M.K., Benoit, P.H., Sears, D.W., 1995. Chondrules: Their diversity and the role of open-system processes during their formation. Icarus 122, 316–346.

Huss, G.R., Rubin, A.E., Grossman, J.N., 2006. Thermal metamorphism in chondrites. In: Lauretta, D., McSween Jr., H.Y. (Eds.), Meteorites and the Early Solar System II. Univ. of Arizona, Tucson, pp. 567–586.

Ikeda, Y., 1983. Major element compositions and chemical types of chondrules in unequilibrated E, O, and C chondrites from Antarctica. Mem. Nat. Inst. Polar Res. Spec. Issue 30, 122–145.

Jackson, S., 2001. The application of ND: YAG Lasers in LA-ICP-MS. In: Sylvester, P. (Ed.), Laser Ablation-ICPMS in the Earth Sciences, Principles and Application. In: Short Course Series, vol. 29. Mineral. Assoc. of Canada, Ottawa, pp. 29–45.

Jackson, S., Longerich, H.P., Dunning, G.R., Fryer, B.J., 1992. The application of Laser-Ablation Microprobe-Inductively coupled plasma—Mass spectrometry (LAM-ICP-MS) to in situ trace-element determinations in minerals. Canad. Min. 30, 1049–1064.

Jenner, G.A., Foley, S.F., Jackson, S.E., Green, T.H., Fryer, B.J., Longerich, H.P., 1993. Determination of partition coefficients for trace elements in high pressure–temperature experimental run products by laser ablation microprobe-inductively coupled plasma-mass spectrometry (LAM-ICP-MS). Geochim. Cosmochim. Acta 58, 5099–5103.

Knacke, O., Kubaschewski, O., Hesselmann, K., 1991. Thermochemical Properties of Inorganic Substances. Springer-Verlag, Berlin.

Krot, A.N., Scott, E.R.D., Zolensky, M.E., 1995. Mineralogical and chemical modification of components in CV3 chondrites: Nebular or asteroidal processing? Meteorit. Planet. Sci. 30, 748–775.

Krot, A.N., Meibom, A., Russell, S.S., Alexander, C.M.O'D., Jeffries, T.E., Keil, K., 2001. A new astrophysical setting for chondrule formation. Science 291, 1776–1779.

Krot, A.N., Meibom, A., Weisberg, G.M.K., Keil, K., 2002. The CR chondrite clan: Implications for early Solar System processes. Meteorit. Planet. Sci. 37, 1451–1490.

Kurat, G., 1967. Einige Chondren aus dem Meteoriten von Mezö-Madaras. Geochim. Cosmochim. Acta 31, 1843–1857.

Kurat, G., 1969. The formation of chondrules and chondrites and some observations on chondrules from the Tieschitz meteorite. In: Millman, P.M. (Ed.), Meteorite Research. Reidel, Dordrecht, pp. 185–190.

Kurat, G., 1984. Geochemistry of chondrules: Fractionation processes in the early Solar System. Proc. 27th Internat. Geol. Congr. 11, 155–197.

Kurat, G., 1985. Geochemistry of chondrules from carbonaceous, ordinary and E chondrites. 10th Symp. Antartic Meteorites. Nat. Inst. Polar Res., Tokyo (abstract).

Kurat, G., 1988. Primitive meteorites: An attempt towards unification. Philos. Trans. R. Soc. Lond. A 325, 459–482.

Kurat, G., Pernicka, E., Herrwerth, I., 1984. Chondrules from Chainpur (LL-3): Reduced parent rocks and vapor fractionation. Earth Planet. Sci. Lett. 68, 43–56.

Kurat, G., Hoppe, P., Engrand, C., 1996. A chondrule micrometeorite from Antarctica with vapor-fractionated trace-element abundances. Meteorit. Planet. Sci. Suppl. A 31, 75–76 (abstract).

Kurat, G., Varela, M.E., Hoppe, P., Clocchiatti, R., 1997. Glass inclusions in Renazzo olivine: Condensates from the solar nebula? Meteorit. Planet. Sci. Suppl. 32. Abstract 76.

Kurat, G., Varela, M.E., Hoppe, P., Weisberg, M.K., Prinz, M., 2000. Trace element distribution within a primitive aggregate from an Allende dark inclusion. Meteorit. Planet. Sci. Suppl. 35. Abstract 94.

Kurat, G., Varela, M.E., Zinner, E., Engler, A., 2004. Condensation origin for chondrules. Meteorit. Planet. Sci. Suppl. 39. Abstract 5070.

Kurahashi, E., Kita, N.T., Nagahara, H., Morishita, Y., 2004. Contemporaneous chondrule formation between ordinary and carbonaceous chondrites. In: Workshop on Chondrites and the Protoplanetary Disk, Kauai, Hawaii, 9039K (abstr.).

Larimer, J.W., 1967. Chemical fractionation in meteorites. I. Condensation of the elements. Geochim. Cosmochim. Acta 31, 1215–1238.

Larimer, J.W., Anders, E., 1967. Chemical fractionations in meteorites. II. Abundance patterns and their interpretation. Geochim. Cosmochim. Acta 31, 1239–1270.

Lauretta, D.S., Killgore, M., Benoit, P.H., Moore, S., Sears, D.W.G., 2002. NWA505: A new LL3.0 chondrite with evidence for chondrule formation in a dust-rich environment. Meteorit. Planet. Sci. 37. Abstract 84.

Levy, E.H., Araki, S., 1989. Magnetic reconnection flares in the protoplanetary nebula and the possible origin of meteorite chondrules. Icarus 81, 74–91.

Liffman, K., Brown, M.J.I., 1996. The protostellar jet model of chondrule formation. In: Hewins, R.H., Jones, R.H., Scott, E.R.D. (Eds.), Chondrules and the Protoplanetary Disk. Cambridge Univ. Press, Cambridge, pp. 285–302.

Lodders, K., 2003. Solar System abundances and condensation temperatures of the elements. Astrophys. J. 591, 1220–1247.

Lodders, K., 2004. Revised and updated thermochemical properties of the gases mercapto (HS), disulfur monoxide (S_2O), thiazyl (NS), and thioxophosphino (PS). J. Phys. Chem. Ref. Data 33, 357–367.

Lodders, K., Fegley, B., 1998. The Planetary Scientist Companion. Oxford Univ. Press, New York, 371 pp.

Lofgren, G.E., 1989. Dynamic crystallization study of chondrule melts of porphyritic olivine composition: Textures experimental and natural. Geochim. Cosmochim. Acta 53, 461–470.

Lu, J., Sears, W.G., Keck, B., Prinz, M., Grossman, J.N., Clayton, R.N., 1990. Semarkona type I chondrules compared with similar chondrules in other classes. Proc. Lunar Sci. Conf. 13, 720–721.

McBreen, B., Hanlon, L., 1999. Gamma-ray bursts and the origin of chondrules and planets. Astron. Astrophys. 351, 759–765.

Merrill, G.P., 1929a. Composition and Structure of Meteorites. U.S. National Museum Bulletin, vol. 149. Smithsonian Institution, Washington, DC.

Merrill, G.P., 1929b. The story of meteorites. In: Merrill, G.P., Foshag, W.F. (Eds.), Minerals from Earth and Sky. Part I. In: Smithsonian Scientific Series, vol. 3. Smithsonian Institution, New York, pp. 1–163.

Norman, M.D., Griffin, W.L., Pearson, N.J., Garcia, M.O., O'Reilly, S.Y., 1998. Quantitative analysis of trace element abundances in glasses and minerals: A comparison of laser ablation ICPMS, solution ICPMS, proton microprobe, and electron microprobe data. J. Anal. Atom. Spectrosc. 13, 477–482.

Pearce, N.J.G., Perkins, W.T., Westgate, J.A., Gorton, M.P., Jackson, S.E., Neal, C.R., Chenery, S.P.A., 1997. Compilation of new and published major and trace element data for NIST SRM 610 and NIST SRM 612 glass reference materials. Geostandard Newslett. 21, 115–144.

Pedley, J.B., Marshall, E.M., 1983. Thermochemical data for gaseous monoxides. J. Phys. Chem. Ref. Data 12, 967–981.

Petaev, M.I., Wood, J.A., 1998. Mineral equilibrium in fractionated nebular systems. II. A new code embracing 18 elements. Lunar Planet. Sci. XXIX. Abstract 1474.

Petaev, M.I., Krot, A.N., 1999. Condensation of CH chondrite materials: Inferences from the CWPI model. Lunar Planet. Sci. XXX. Abstract 1775.

Petaev, M.I., Meibom, A., Krot, A.N., Wood, J.A., Keil, K., 2001. The condensation origin of zoned metal grains in Queen Alexandra Range 94411: Implications for the formation of the Bencubbin-like chondrites. Meteorit. Planet. Sci. 36, 93–106.

Phillip, W., Hartquist, T.W., Morfill, G.E., Levy, E.H., 1998. Chondrule formation by lightning in the protosolar nebula? Astron. Astrophys. 331, 121–146.

Rambaldi, E.R., Fredriksson, B.J., Fredriksson, K., 1981. Primitive ultrafine matrix in ordinary chondrites. Earth Planet. Sci. Lett. 56, 107–126.

Rasmussen, K.L., Wasson, J.T., 1982. A new lightning model for chondrule formation. In: Papers Presented to the Conference on Chondrule and Their Origins. Lunar and Planet. Inst., Houston, p. 53 (abstract).

Richard, L.R., 1995. Mineralogical and petrological, data processing system for Windows, version 2.02. Minpet Geological Software–Logiciel Géologique Minpet, Quebec.

Rubin, A.E., 1984. Coarse-grained chondrule rims in type 3 chondrites. Geochim. Cosmochim. Acta 48, 1779–1789.

Rubin, A.E., Wasson, J.T., 1987. Chondrules, matrix and coarse-grained chondrule rims in Allende meteorite: Origin, interrelationships and possible precursor components. Geochim. Cosmochim. Acta 51, 1923–1937.

Rubin, A.E., Wasson, J.T., 1988. Chondrules and matrix in the Ornans CO3 meteorite: Possible precursor components. Geochim. Cosmochim. Acta 52, 425–432.

Sears, D.W.G., Lu, J., Benoit, P.H., De Hart, J.M., Lofgren, G.E., 1992. A compositional classification scheme for meteoritic chondrules. Nature 357, 207–211.

Shu, F.H., Shang, H., Lee, T., 1996. Toward an astrophysical theory of chondrites. Science 271, 1545–1552.

Shu, F.H., Shang, H., Gounelle, M., Glassgold, A.E., Lee, T., 2001. The origin of chondrules and refractory inclusions in chondritic meteorites. Astrophys. J. 548, 1029–1050.

Skinner, W.R., 1990. Bipolar outflows and a new model of the early Solar System. Part I: Overview and implications of the model; Part II: The origins of chondrules, isotopic anomalies, and chemical fractionations. Lunar Planet. Sci. XXI, 1166–1169 (abstract).

Sonett, C.P., 1979. On the origin of chondrules. Geophys. Res. Lett. 6, 677–680.

Taylor, R.P., Jackson, S.E., Longerich, H.P., Webster, J.L., 1997. In situ trace-element analysis of individual silicate melt inclusions by laser ablation microprobe-inductively coupled plasma mass spectrometry (ICP-MS). Geochim. Cosmochim. Acta 61, 2559–2567.

Varela, M.E., Kurat, G., 2000. Glass inclusions in olivines of the Renazzo (CR) chondrite. Meteorit. Planet. Sci. Suppl. 35, A162–A163 (abstract).

Varela, M.E., Kurat, G., 2004. Glasses in meteorites: A unification model. Meteor. Planet. Sci. Suppl. 39. Abstract 109.

Varela, M.E., Kurat, G., Hoppe, P., Brandstätter, F., 2001. Chemistry of glass inclusions in olivines of the CR chondrites Renazzo, Acfer 182 and El Djouf 001. Geochim. Cosmochim. Acta 66, 1663–1679.

Varela, M.E., Kurat, G., Zinner, E., 2002a. A glass inclusion in olivine and mesostasis glass of a Kaba (CV3) aggregate are sisters. Meteorit. Planet. Sci. Suppl. 37, A143 (abstract).

Varela, M.E., Kurat, G., Hoppe, P., Weisberg, M.K., 2002b. Chemistry of glass inclusions in olivines of a dark inclusion and the host Allende CV3 chondrite. Lunar Planet. Sci. XXXIII. Abstract 1190.

Varela, M.E., Kurat, G., Zinner, E., Métrich, N., Brandstätter, F., Ntaflos, T., Sylvester, P., 2003. Glasses in the D'Orbigny angrite. Geochim. Cosmochim. Acta 67, 5027–5046.

Varela, M.E., Kurat, G., Zinner, E., 2005. A liquid-supported condensation of major minerals in the solar nebula: Evidence from glasses in the Kaba (CV3) chondrite. Icarus 178, 553–569.

Varela, M.E., Kurat, G., Zinner, E., 2006. The primary liquid condensation model and the origin of barred olivine chondrules. Icarus 184, 344–364.

Walter, L.S., Dodd, R.T., 1972. Evidence for vapor fractionation in the origin of chondrules. Meteoritics 7, 341–352.

Wasson, J.T., 1985. Meteorites: Their Record of Early Solar-System History. Freeman, New York, 267 pp.

Wasson, J.T., 1992. Constraints on chondrule origins. Meteoritics 29, 304.

Wasson, J.T., Krot, A.N., Lee, M.S., Rubin, A.E., 1995. Compound chondrules. Geochim. Cosmochim. Acta 59, 1847–1869.

Weidenschilling, S.J., Marzari, F., Hood, L.L., 1998. The origin of chondrules at jovian resonances. Science 279, 681–684.

Whipple, F.L., 1966. Chondrules: Suggestions concerning their origin. Science 153, 54–56.

Wood, J.A., 1962. Chondrules and the origin of the terrestrial planets. Nature 197, 127–130.

Wood, J.A., 1963. On the origin of chondrules and chondrites. Icarus 2, 152–180.

Wood, J.A., 1967. Olivine and pyroxene compositions in type II carbonaceous chondrites. Geochim. Cosmochim. Acta 31, 2095–2108.

Wood, J.A., 1983. Formation of chondrules and CAI's from interstellar grains accreting to the solar nebula. Mem. Nat. Inst. Polar. Res. Special Issue 30, 84–92.

Wood, J.A., 1984. On the formation of meteoritic chondrules by aerodynamic drag heating in the solar nebula. Earth Planet. Sci. Lett. 70, 11–26.

Wood, J.A., 1985. Meteoritic constraints on processes in the solar nebula: An overview. In: Black, D.C., Matthews, M.S. (Eds.), Protostars and Planets II. Univ. of Arizona Press, Tucson, AZ, pp. 682–702.

Wood, J.A., 1996. Unresolved issues in the formation of chondrules and chondrites. In: Hewins, R.H., Jones, R.H., Scott, E.R.D. (Eds.), Chondrules and the Protoplanetary Disk. Cambridge Univ. Press, Cambridge, pp. 55–69.

Wood, J.A., Hashimoto, A., 1993. Mineral equilibrium in fractionated nebular systems. Geochim. Cosmochim. Acta 57, 2377–2388.

Wood, J.A., McSween Jr., H.Y., 1977. Chondrules as condensation products. In: Comets, Asteroids, Meteorites: Interrelations, Evolution and Origins. Proc. 39th International Colloquium, Lyons, France, 1976. University of Toledo, Toledo, OH, pp. 365–373.

Wood, J.A., Morfill, G.E., 1988. A review of solar nebula theory. In: Kerridge, J.F., Matthews, M.S. (Eds.), Meteorites and the Early Solar System. Univ. of Arizona Press, Tucson, AZ, pp. 329–347.

Yoneda, S., Grossman, L., 1995. Condensation of CaO–MgO–Al_2O_3–SiO_2 liquids from cosmic gases. Geochim. Cosmochim. Acta 59, 3413–3444.